UNIVERSITÉ DE STRASBOURG

Thèse présentée pour obtenir le titre de
Docteur de l'Université de Strasbourg
Discipline : Physique

Some thermodynamic, conformational and rheological properties of linear and hyperbranched polymer melts revisited

Patrycja Polińska

Thèse soutenue publiquement le 24 février 2014

Membres du Jury :

Directeur de thèse : **M. J. P. Wittmer**
Directeur de recherche, Institut Charles Sadron, Strasbourg, France

Rapporteur externe : **M. O. Borisov**
Professeur, Université de Pau, Pau, France

Rapporteur externe : **M. F. Leermakers**
Professeur, WU Agrotechnology & Food Sciences, Wageningen, Netherlands

Examinateur interne : **M. Th. Charitat**
Professeur, Institut Charles Sadron, Strasbourg, France

Examinateur externe : **M. A. Blumen**
Professeur, Albert-Ludwigs-Universität, Freiburg, Germany

Examinateur externe: **Mme. H. Xu**
Professeur, Université de Lorraine, Lorraine, France

Contents

List of Figures

List of Tables

List of symbols

d_C	-	shortest distance between two bead centers
d_f	-	fractal dimension
$D_{S,G}$	-	dendrimer with G-generation and branch length S
G	-	generation number; shear modulus
$g(r)$	-	radial pair distribution function
$J(t)$	-	heat flux
K	-	bulk modulus
N_c	-	contact number
N	-	number of beads in a molecule
R_e	-	core-to-end distance
R_g	-	radius of gyration
S	-	spacer length (branch length)
δ	-	shell thickness
η	-	viscosity
κ	-	compressibility
ρ	-	number density
$\rho(r)$	-	number density as a function of a radial distance r
σ	-	bead radius

Acknowledgements

This thesis was realized under the supervision of Dr. Joachim P. Wittmer from Institute Charles Sadron (UPR CNRS, Strasbourg) in the Group of the Theory and Simulations of Polymers. I was collaborating with Prof. Hong Xu (Universtié de Lorraine, Metz), Prof. Christian Friedrich (Polymer Processing Group, Freiburg) and Prof. Alexander Blumen (Theoretical Polymer Physics Group). This interdisciplinary work involved many people with whom I was interacting during the course of my thesis and from whom I have learn a lot.

First of all I would like to thank my supervisor, Joachim Wittmer, for pulling me into many interesting projects and for the freedom I got with my own one but as well for keeping an ear to the ground. I got an unique opportunity to explore the beauty of the science.

I would also like to thank Prof. Jörg Baschnagel for his support and amazing possibilities he gave us together with Prof. Günther through the IRTG project.
At this point I would like to thank to the coordinators of the IRTG, Christelle Vergnat, Amandine Henckel and Brigitta Zovko, who were helping students to go through the administrative difficulties and were doing it heartily.

I would as well to thank the Dr. Oleg Borisov and Prof. Frans Leermakers not only for accepting being the reviewers of the thesis but as well for the discussions that pushed my work further. As well I would like to thank to all the jury members for their consideration, accepting my invitation and for the constructive questions during the defense.

During my PhD I was hosted by two groups under the supervision of Prof. Alexander Blumen and Prof. Christian Friedrich, I really appreciate their hospitality. I would like to thank as well all the members of both groups in Freiburg that made my stay there so pleasant, especially Carina Gillig who not only showed me how interesting the chemistry world is but was a great colleague.

I want to thank to Prof. Hong Xu for her attention to the detailed of the project and providing me a necessary scientific knowledge and pulling me into interesting projects,

Thanks to the broad scientific and technical knowledge of Dr. Olivier Benzerara and Dr. Hendrik Mayer my work got a truly scientific shape. Thank you for your help.

I want to thank to all the members of our group, Dr. Fabian Weyßer, Dr. Alex Shvetz, Dr. Falko Ziebert, Dr. Gi-Moon Nam, Dr. Julia Zabel, Dr. Stephan Frey, Dr. Jean Farago, Dr. Nava Schulman, Dr. Igor Kulic, Dr. André Galushko, Julien Fierling and Céline Rucher for their company through last years.

Ania, Franck and Mirela and Hatice, thank you for being great friends.
All the people in the ICS who make the atmosphere in the institute so agreable.

Paweł and Paulina, thank you for your understanding and support.
I want as well thank to my parents, who showed me that it is the discovery of new things that brings the most joy in life.

Résumé de la thèse

Observations générales

Ma thèse a été réalisée à l'Institut Charles Sadron (ICS) de Strasbourg sous la direction du Docteur Joachim Wittmer dans le cadre de l'IRTG Soft Matter Science en collaboration avec le Professeur Hong Xu (Metz), le Professeur Christian Friedrich (Freiburg) et le Professeur Alexander Blumen (Freiburg). Une bonne étude pluridisciplinaire fourni une large gamme de possibilités pour résoudre plusieurs problèmes difficilement solvables. L'IRTG Soft Matter Science dont je dépends, est conçu pour fournir des solutions dans la compréhension des problèmes complexes entre plusieurs disciplines scientifiques. C'est dans ce but que l'IRTG, une collaboration entre mon groupe de recherche et d'autres groupes, est née. Mon travail avec le professeur Xu était centré sur les propriétés thermodynamiques et mécaniques des polymères denses et sur leurs liens avec les systèmes de la matière molle que j'expliquerai brièvement dans le paragraphe suivant. Ma collaboration avec le Professeur Friedrich m'a permis d'étudier les propriétés de conformation et les propriétés rhéologiques des polymères hyperbranchés qui sont les actuelles priorités de mes recherches. La participation théorique de mon travail, principalement des travaux de modélisation numérique, a été effectuée en collaboration avec le Professeur Blumen. Cette partie du projet était particulièrement intéressante pour moi.

Contributions à la description des propriétés thermodynamique et mécanique des polymères à l'état fondu et des systèmes de matière molle.

Tant qu'il sera difficile voire impossible d'examiner certains cas particuliers avec des instruments communs, la simulation numerique propose une méthode compréhensible capable d'etudier ces cas particuliers. Aussi loin que notre imagination le permet, nous pouvons établir des correspondances grâce aux données obtenues pour examiner précisément le matériau choisi. Lors de ma thèse, j'ai pu me heurter à plusieurs problèmes intrigants. Mon approche face à ceux-ci est partiellement décrite dans le manuscrit. Lors de mon stage

de trois mois (2009) à l'ICS, j'ai déjà participé à l'etude numérique de la corrélation temporell des déplacements dans des liquides de Lennard-Jones, denses, fortement suramortis et qui dépendent d'un thermostat de Langevin imposé. Un problème fortement lié concerne la déviation de la dynamique du centre de masse des polymères par rapport au modèle de Rouse pour des polymères denses mais non-enchevêtrés. Ceci a été étudié dans mes trois premières publications que je reprendrai dans mon manuscript [1, 2, 3]. La réponse linéaire élastique d'un système sous l'action de champs variables externes est l'une des méthodes d'investigation les plus communes pour décrire un matériau. Certaines fluctuations du système dépendent fortement des contraintes imposées au système [4, 5, 6]. De nombreux efforts ont été consacrés à valider la fiabilité du modèle et à l'améliorer. C'est pour cette raison que nous avons décidé de clarifier la notion de distance critique d'un potentiel et de son décalage sur des quantités impliquant les dérivées secondes (et de plus haut degrés) de ce potentiel [7].

Etude principale: Polymères hyperbranchés

Le champ de recherche des polymères étoiles, développés à la fin des années 1970, a explosé durant la dernière décennie. Au tout début, ces molécules étaient étudiés uniquement en sciences des matériaux et des polymères mais ces nouveaux types de macromolécules ont rapidement trouvé leur place dans un champ pluridisciplinaire entre la chimie organique, la médecine, la biologie et les biotechnologies. Dans le dernier projet sur lequel nous nous concentrons ici, nous étudirons les corrélations entre la topologie des polymères étoiles, car leur comportement n'est pas bien compris. L'étude de polymères hyperbranchés montre qu'ils sont substantiellement différents de leurs analogues linéaires. En utilisant des méthodes de simulation, nous pouvons obtenir des informations inaccessibles par des méthodes expérimentales et heureusement obtenir de précieuses informations du point de vue industriel et scientifique. Notre point de départ était l'étude de l'influence de la longueur d'une branche et du nombre de générations sur la conformation de la molécule. Ces deux paramètres influent visiblement sur la forme de la molécule. Ces changements, visibles pour différentes propriétés comme le nombre de contact, le facteur de forme ou le déplacement carré moyen, seront explicités dans la thèse. Actuellement, il existe une controverse dans la littérature, à savoir si les molécules en étoile, peuvent supporter une structure à centre de faible densité et si elles peuvent devenir colloïdales pour un grand nombre de générations. Cette étude traite le problème par des simulations et comme expliqué dans le manuscrit, dans notre simulation, nous avons observé un centre de faible densité pour un grand nombre de générations et une enveloppe extérieure plutôt compacte. Cette tendance se retrouve également pour les propriétés dynamiques. Le manque d'enchevétrement dans les polymères hyperbranchés fait d'eux des matériaux moins résistant que ceux composés de chaînes linéraires. Un autre point est la diminution

de la mobilité causée par un grand nombre de points de ramification. La viscosité perd sa simple dépendance à la masse dans le cas d'une chaîne linéaire.

Au cours de ma thèse j'ai organisé une conférence "Experimental and theoretical methods for investigating polymer dynamics" in Schauinsland, Allemagne (5-6 Mars 2012).

Chapter 1

Introduction

1.1 Context of my research

Generalities. Soft matter [8] is a subfield of condensed matter [9] comprising a variety of physical states that are easily deformed by thermal stresses or thermal fluctuations. They include liquids [10, 11], colloids, polymers [12, 13, 14, 15], foams, gels and various glass forming materials [16]. They share an important common feature in that predominant physical processes occur at an energy scale comparable with room temperature thermal energy. (At these temperatures, quantum aspects are generally unimportant [8].) Soft matter physics is an interdisciplinary field encompassing statistical physics [17, 18], materials science [19], and (more recently) biophysics. The experimental and computational study of soft matter systems is generally difficult due to the extremely *wide range of length and time scales* which govern their static and dynamical behavior [12]. This challenge can often only be met by studying by means of computer simulations [20, 21, 22] extremely simplified *coarse-grained* models characterized by a small number of effective parameters.

Polymeric systems. Such a simplified approach is indicated for the numerical study of solutions and melts of (linear or branched, unattached or grafted, neutral or charged, quenched or annealed, ...) macromolecular polymer chains [14] which is a central focus of my current research group at the Institut Charles Sadron (ICS) in Strasbourg [23, 1, 24, 25]. Often required parameters are, e.g., the number of effective monomers N per chain, the Wiener index W_1 characterizing the first moment of the distribution of the curvilinear distances of topologically connected monomer pairs [26] (cf. Sec. 3.3), and the number density ρ of the particles [13, 14]. From the thermodynamic point of view it is the temperature T (often set to unity in the current work), the pressure P, the compression modulus K and (e.g., for solid-like glasses at low temperatures [25]) the shear modulus G which characterize in addition the isotropic equilibrium phases we shall focus

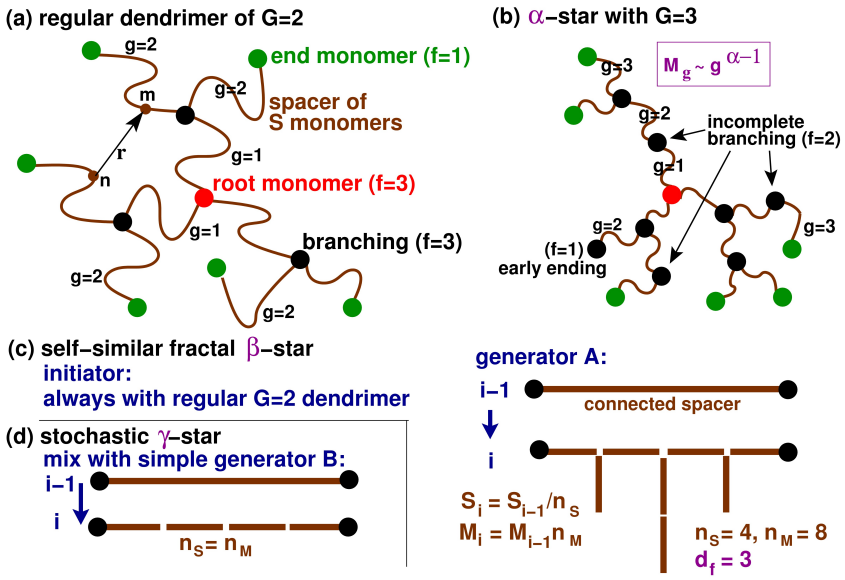

Figure 1.1: Sketch of different topologies of branched polymer stars considered: **(a)** Regular dendrimer of generation number $G = 2$ with $M = 9$ arms. **(b)** Hyperbranched so-called "α-stars" with imposed spacer chain number $M_g \sim g^{\alpha-1}$ for $g \leq G$ constructed iteratively ($g \to g+1$) by restricting randomly the branching of the arms. Some branches may thus end at $g < G$. **(c)** Self-similar "β-stars" of fractal dimension d_f are generated starting with regular $G = 2$ dendrimers and replacing iteratively the M_{i-1} spacers of length S_{i-1} by $M_i = M_{i-1}n_M$ spacers of length $S_i = S_{i-1}/n_S$. The generator shown corresponds to self-similar stars of constant density ($d_\mathrm{f} = 3$). **(d)** Multifractal "γ-stars" are obtained by applying randomly more than one generator. Mixing with equal weight the generator B ($n_S = n_M = 4$) with the compact star generator A ($n_S = 4$, $n_M = 8$) leads to a star with $d_\mathrm{f} = 2.5$.

on [1].[1] Experimental relevant observables of such polymeric systems are, e.g., the radius of gyration $R_\mathrm{g}(N)$ or the intramolecular coherent form (structure) factor $F(q)$ with q being the wavevector of the light, X-ray (SAXS) or small-angle neutron (SANS) scattering method used [12, 14, 15]. It is generally the aim of a theoretical or computational study to understand and, possibly, to predict the scaling of such experimental observables with respect to, say, the monomer number N, the chain topology or architecture imposed by the chemical reaction.

Hyperbranched polymers and dendrimers. The use of simple coarse-grained models is especially relevant for the simulation and characterization of dilute and dense solutions of (asymptotically) large *hyperbranched polymer stars* [14, 27]. I remind that regular *dendrimers* are a subset of hyperbranched polymers without topological imperfections on

[1] Obviously, the static shear modulus G vanishes in the liquid state [8] as emphasized in Chapter 2. The notation $G(t) \equiv \tau(t)/\gamma$ used in Sec.4.4 refers to the time-dependent shear stress relaxation modulus with $\tau(t)$ being the shear stress remaining at time t after a shear strain γ was applied at $t = 0$ to an unstressed reference system [14]. For historical reasons, the notation G is unfortunately also used to specify the number of generations in hyperbranched polymer stars in Chapter 3 and 4.

which much of the recent experimental [28], theoretical [29, 30, 31, 32, 33] and computational research [31, 34, 35, 36, 37, 38, 39, 40] has concentrated on. A sketch of such regular dendrimers can be seen in panel (a) of Fig. 1.1 which is further discussed in more detail in Chapter 3 and 4. Such "starburst" molecules are made either by divergent synthesis, starting from the root monomer and sequentially filling out generations [28], or by convergent synthesis, growing branched arms first and then attaching them to the core [41]. There is a considerable research on dendrimer chemical synthesis, and there are many reviews in the literature [42, 43, 44, 45]. Dendritic polymers have shown promise in a host of applications including the photochemistry [46], biology- and biochemistry-oriented contribution to gene transfection [47], acting as antibody dendrimers [48]. The pharmaceutical industry could attach side-specific receptors and use them as delivery vehicles for bioreactive molecules [49]. In order to better engineer the desired properties into a starburst dendrimer, one must know how its internal (intra chain) density profile $\rho(r)$ is affected by the specific chemical characteristics such as the functionality f of the branching monomers (filled spheres in Fig. 1.1), the length S of the spacer chains between the branching points, and their relative flexibility or rigidity.

One central query. For a number of technologically important applications, it is crucial to predict the range of parameters for which a dendrimer has a dense outer shell with a solvent-filled, hollow (or at least monomer depleted) inner core.[2] Interestingly, there is a controversy in the literature as to whether the simplest case of an uncharged dendrimer with flexible spacers and purely repulsive monomers has a dense or a hollow inner core. In an early analytical self-consistent mean-field calculation (assuming implicitly strongly stretched dendrimer arms), de Gennes et Hervet [29] found the density to be minimal at the core *increasing monotonically* to the outer edge. At variance, a numerical kinetic growth algorithm of regular dendrimers without equilibration of the monomer positions by Lescanec and Muthukumar [34] showed a maximum density at the core *decreasing monotonously* to the edge. This general "dense core picture" has essentially been confirmed by the (thermodynamically more rigorous) Monte Carlo simulations by Mansfield and Klushin [50], the molecular dynamics simulations by Murat and Grest [36] and other more recent numerical studies [38, 39, 51]. Interestingly, a *slight local minimum* at small radial distances r for larger generation numbers G can be observed in some these numerical studies [36]. Such a local minimum, if confirmed, would not be consistent with the (present version of the) self-consistent mean-field model suggested by Boris and Rubinstein [52]. Note that most of the mentioned numerical studies focus on *dilute* dendrimers [34, 36, 38, 39, 50, 51]. Using a variant of the bead-spring model studied by Murat and Grest [36], much of my PhD work was dedicated to the equilibration and characterization of *dense melts* of such regular dendrimers.

[2] In the extreme case such a hollow structure may mimic a cell membrane.

1.2 Stepping stones of my PhD work

Contributing to various numerical issues of concern to my research group and my collaborators in Metz (Prof. H. Xu) and Freiburg (Prof. A. Blumen, Prof. C. Friedrich, C. Gillig), I had the opportunity to contribute to several publications [1, 2, 3, 4, 5, 6, 7, 53, 54]. Using various molecular dynamics and Monte Carlo schemes [20, 21, 22, 55], I have thus worked on a broad range of topics covering dense colloidal solutions and glasses [4, 5, 6, 7, 56], linear polymer melts [1, 2, 3] and hyperbranched polymer stars [54, 57]. Following my (yet unpublished) internship study on displacement correlations [56] at the ICS (2010), I have briefly touched dynamical properties [1, 2, 3] related to the recently discovered viscoelastic hydrodynamic interactions in polymer melts [24]. Most of my work in the last three years has focused, however, on static issues:

(i) the numerical determination of elastic moduli and related static correlation functions in different (generalized Gaussian) ensembles [4, 5, 6, 7, 53] and

(ii) conformational properties of hyperbranched polymer stars [54, 57].

Especially, my molecular simulations of dendrimer melts [57] have turned out to be computationally very demanding requiring about two years of sampling time on our local workstation cluster. For this reason we have still not managed to conclude this most central issue of my PhD work. I note that this research issue has been triggered by my collaboration with the groups of Prof. Friedrich and Prof. Blumen in Freiburg in the frame of the IRTG (International Research and Training Group) "Soft Matter" where my PhD grant was funded. Originally, the idea has been to investigate

(iii) the elastic and rheological properties of *transient networks* formed by systems of, e.g., *telechelic polymers* in water-old emulsions [58, 59], living polymer micellar systems [60] or hyperbranched chains with sticky end groups, as have been synthesized in the Friedrich group [61].

The simulation of solutions and melts of regular dendrimers with purely repulsive monomer interactions (see Sec.4.2 for details) was thus initially thought to be just a first step for the study of transient hyperbranched polymer networks. Unfortunately, mainly due to the already mentioned huge sampling times needed, the switching on of attractive interactions between the end groups of the hyperbranched chains has not been possible yet. One reason for the study of the elastic and rheological properties in colloidal systems was that we wanted to prepare the methods needed for the investigation of the transient network systems[3]. Unfortunately, it has not been possible within this PhD to bring together *(i)* and *(ii)* to study numerically *(iii)* which must be postponed to the future.

[3]For this reason we also got interested in the "reversed non-equilibrium molecular dynamics" (RNEMD) method by Müller-Plathe for computing the shear viscosity [62] described in Sec.4.4.

1.3 Scope and outline of my PhD thesis

The presented PhD manuscript mirrors the two main fields *(i)* and *(ii)* of my research. *(i)* Chapter 2 presents the paper [7] on elastic-mechanical properties on which I have contributed most. The truncation of a pair potential at a distance r_c is well-known to imply in general an impulsive correction to the pressure and other moments of the first derivatives of the potential [21]. That, depending on r_c, the truncation may also be of relevance to *higher derivatives* of the potential is shown theoretically for the Born contributions to the elastic moduli obtained using the stress-fluctuation formalism [4, 21] in d dimensions. Focusing on isotropic liquids for which the shear modulus G must vanish by construction, the predicted corrections are tested numerically for binary mixtures [63] and polydisperse Lennard-Jones beads [64, 65] in, respectively, $d = 3$ and $d = 2$ dimensions. If the impulsive correction is properly taken into account, $G(T)$ is seen to vanish for all temperatures T above the glass transition temperature T_g and to increase strongly as $G \approx (1 - T/T_g)^{1/2}$ on cooling below T_g, i.e. a thermodynamically well-defined four-point correlation function is shown to become finite at the transition. More details on the calculation of the shear modulus at and around the glass transition can be found in Ref. [6] which is not reproduced here since I have only played a minor part in this project.

(ii) Conformational properties of regular dendrimers and hyperbranched polymer stars with *Gaussian statistics* [12, 13] for the spacer chains between branching points are revisited in Chapter 3 which is based on a recently submitted manuscript [54]. We investigate the scaling for asymptotically long chains especially for fractal dimensions $d_f = 3$ (marginally compact [15, 66]) and $d_f = 2.5$ (diffusion limited aggregation [67, 68, 69, 70]). Power-law stars obtained by imposing the number of additional arms per generation are compared to truly self-similar stars. We discuss effects of weak excluded volume interactions (Sec. 3.6) and sketch the regime where the Gaussian approximation should hold in dense solutions and melts for sufficiently large spacer chains (Sec. 3.7). Chapter 3 is needed to introduce some notations and well-known concepts [12, 14] and to discuss the Gaussian reference (all excluded volume interactions being switched off) which should be relevant — assuming sufficiently large spacer chains as seen in Sec. 3.7 — for describing the regular dendrimer *melts* discussed in the following Chapter.

We present in Chapter 4 our still on-going molecular dynamics simulation of dendrimers of a broad range of the spacer chain length S at the standard "melt density" $\rho = 0.85$ of the Kremer-Grest bead-spring model [36, 71]. Sec.4.2 presents our numerical model and some technical issues related to the equilibration and characterization of the samples. The static properties of the dendrimers are described in Sec.4.3. This section contains the most surprising finding of this PhD work: The total density profile of the dendrimers is found to have a strikingly *strong depletion* close to the root monomer of the

star, i.e. at variance to various statements made in the literature [34, 36, 39, 51, 72, 73] the density is strongly non-monotonous. Sec. 4.4 attempts to characterize the equilibrium dynamics of our dendrimer melts. While for large generation numbers and short spacer chains (where the dendrimers essentially become compact spheres) the diffusion constant D is seen to decrease inversely with mass N (as expected for uncorrelated random forces acting on all N particles [12, 13]), additional slowing-down of the diffusion is observed with increasing spacer length. The latter effect may be traced back to the stronger interpenetration of the stars and the increasing influence of topological interactions (implying possibly reptation-like dynamics of the star arms) [12]. Surprisingly and perhaps in contradiction to the single chain (self) dynamics, we observe that for large generation numbers the zero-shear viscosity η, obtained using Müller-Plathe's out-of-equilibrium method [62], gets essentially G-independent, i.e. the *collective* dynamical response of the melt becomes N-independent.

The work of my PhD is summarized in Chapter 5.

1.4 List of own publications

Published papers:

1. *Scale-free center-of-mass displacement correlations in polymer melts without topological constraints and momentum conservation: A bond-fluctuation model study*
   J.P. Wittmer, P. Polińska, H. Meyer, J. Farago, A. Johner, J. Baschnagel, and A. Cavallo
   The Journal of Chemical Physics **134**, 23 (2011)

2. *Scale-Free Static and Dynamical Correlations in Melts of Monodisperse and Flory-Distributed Homopolymers*
   J.P. Wittmer, A. Cavallo, H. Xu, J.E. Zabel, P. Polińska, N. Schulmann, H. Meyer, J. Farago, A. Johner, S.P. Obukhov, and J. Baschnagel
   Journal of Statistical Physics **145**, 4 (2011)

3. *Note: Scale-free center-of-mass displacement correlations in polymer films without topological constraints and momentum conservation*
   J.P. Wittmer, N. Schulmann, P. Polińska, and J. Baschnagel
   The Journal of Chemical Physics **135**, 18 (2011)

4. *Strictly two-dimensional self-avoiding walks: Thermodynamic properties revisited*
   N. Schulmann, H. Xu, H. Meyer, P. Polińska, J. Baschnagel, and J.P. Wittmer
   The European Physical Journal E **35**, 9 (2012)

5. *Impulsive correction to the elastic moduli obtained using the stress-fluctuation formalism in systems with truncated pair potential*
   H. Xu, J.P. Wittmer, P. Polińska, and J. Baschnagel
   Physical Review E **84**, 4 (2012)

6. *Shear modulus of simulated glass-forming model systems: Effects of boundary condition, temperature, and sampling time*
   J.P. Wittmer, H. Xu, P. Polińska, F. Weysser, and J. Baschnagel
   The Journal of Chemical Physics **138**, 12 (2013)

7. *Communication: Pressure fluctuations in isotropic solids and fluids*
   J.P. Wittmer, H. Xu, P. Polińska, F. Weysser, and J. Baschnagel
   The Journal of Chemical Physics **138**, 19, (2013)

8. *Compressibility and pressure correlations in isotropic solids and fluids*
   J.P. Wittmer, H. Xu, P. Polińska, C. Gillig, J. Helfferich, F. Weysser, and J. Baschnagel
   The European Physical Journal E **36**, 11 (2013)

9. *Hyperbranched polymer stars with Gaussian chain statistics revisited*
   P. Polińska, C. Gillig, J.P. Wittmer and J. Baschnagel
   The European Physical Journal E **37**, 12 (2014)

Papers in preparation:

10. *Non-monotonous density profile of starburs dendrimer melts*
    P. Polińska, H. Meyer, J.P. Wittmer

11. *Long-range spatio-temporal correlations of the displacement field of both incomressible and overdamped liquids: Phenomenological linear response theory and Monte Carlo simulation results*
    P. Polińska, J. Farago, J.P. Wittmer, A. Johner, J. Baschnagel

Reference [2] is a review paper of my research group at the ICS. The presented PhD manuscript focuses on the publications [5] and [9]. Currently, we are preparing a publication on our molecular dynamic simulation of starburst dendrimer melts [10] on which Chapter 4 is based. Publication [11] refers to an yet unwritten paper summarizing some of my results obtained in my internship at the ICS (2011).

Chapter 2

Impulsive correction to the elastic moduli obtained using the stress-fluctuation formalism

2.1 Introduction

Background. It is common practice in computational condensed matter physics [20, 21, 22] to truncate a pair interaction potential $U(r)$, with r being the distance between two particles i and j, at a conveniently chosen cutoff r_c. This allows to reduce the number of interactions to be computed and energy or force calculations become $\mathcal{O}(n)$-processes where n denotes the particle number. However, the truncation also introduces technical difficulties, e.g., instabilities in the numerical solution of differential equations as well-studied especially for the molecular dynamics (MD) method [20]. Let us label the interaction between two particles $i < j$ by an index l. For simplicity of the presentation and without restricting much in practice the generality of our results, we assume that

- the potential $U(r)$ is short-ranged, i.e. that it decays within a few particle diameters,
- it scales as $U(r) \equiv u(s)$ with the reduced dimensionless distance $s = r/\sigma_l$ where σ_l characterizes the length scale of the interaction l and
- the same reduced cutoff $s_\mathrm{c} = r_\mathrm{c}/\sigma_l$ is set for all interactions l.

For instance, for monodisperse particles with constant diameter σ, as for the standard Lennard-Jones (LJ) potential [20],

$$u_\mathrm{LJ}(s) = 4\epsilon \left(\frac{1}{s^{12}} - \frac{1}{s^6} \right), \tag{2.1.1}$$

the scaling variable becomes $s = r/\sigma$ and the reduced cutoff $s_c = r_c/\sigma$. The effect of introducing s_c is to replace $u(s)$ by the truncated potential

$$u_t(s) = u(s)H(s_c - s) \tag{2.1.2}$$

with $H(s)$ being the Heaviside function [74]. Even if Eq. (2.1.2) is taken *by definition* as the new system Hamiltonian, it is well known that impulsive corrections at the cutoff have to be taken into account in general for the pressure P and other moments of the first derivatives of the potential [21]. These corrections can be avoided by considering a properly shifted potential [21]

$$u_s(s) = (u(s) - u(s_c))\, H(s_c - s) \tag{2.1.3}$$

as emphasized also below in Sec. 2.2.1.

Key points made. Reproducing essentially Ref. [7], I discuss in this Chapter the consequences of Eq. (2.1.3) on quantities involving second (and higher) derivatives of the potential. For these quantities the standard shifting of a truncated potential is shown to be insufficient in general to avoid impulsive corrections. I shall demonstrate that this is particulary the case for the Born contribution $C_B^{\alpha\beta\gamma\delta}$ (defined below) to the elastic moduli computed using the stress-fluctuation formalism described in detail in the literature [10, 25, 53, 65, 75, 76, 77, 78, 79, 80, 81, 82, 83, 84]. This should be of importance for the *precise* localization of the transition between different thermodynamic phases by means of the elastic moduli, especially for liquid/sol ($G = 0$) to solid ($G > 0$) transitions in network forming systems where the shear modulus G plays the role of an order parameter [85]. Examples of current experimental and computational interest include the glass transition of colloidal or polymer liquids [16, 86, 87, 88, 89, 25], colloidal gels [90], hyperbranched polymer chains with sticky end-groups [61] or bridged networks of telechelic polymers in water-oil emulsions [58, 59].

Outline. After recapitulating in Sec. 2.2.1 the known corrections for the pressure and similar first derivatives of the potential, the impulsive correction for the general Born contribution $C_B^{\alpha\beta\gamma\delta}$ is given in Sec. 2.2.2. I describe then in Sec. 2.2.3 the corrections on the compression modulus K and the shear modulus G in isotropic systems. I comment on polydispersity effects and mixed potentials in Sec. 2.2.4. The results are reexpressed in terms of the radial pair distribution function $g(s)$ in Sec. 2.2.5 which allows to predict the asymptotic behavior for large s_c. Further algorithmic section gives some technical details on the two numerical model systems [63, 64, 65] in $d = 3$ and $d = 2$ dimensions used to test the predictions made. This test is described in Sec. 2.3. We focus there on the high-temperature liquid regime of both models where the shear modulus G must vanish [10, 11],

since this provides a clear reference point for verifying the predicted corrections. The main results are summarized in Sec. 2.4.1 and an outlook on related issues is given in Sec. 2.4.2. Since both numerical models considered are well-known glass-formers, I comment briefly in Sec. 2.4.3 on the related Ref. [4] investigating the shear modulus $G(T)$ as a function of temperature T around the glass transition temperature $T_{\rm g}$. Such a characterization is of considerable current interest due to the qualitative different theoretical suggestions put forward by mode-coupling theory (MCT) predicting a discontinuous jump [16, 88] and by replica theory [86] implying a continuous transition [87, 89].

2.2 Theoretical predictions

2.2.1 Reminder

Truncated potential. As usual for pairwise additive interactions the mean pressure $P = P_{\rm id} + P_{\rm ex}$ may be obtained as the sum of the ideal kinetic contribution $P_{\rm id} = k_{\rm B}T\rho$ and the excess pressure contribution [20, 21]

$$P_{\rm ex} = \left\langle \hat{P}_{\rm ex} \right\rangle = -\frac{1}{dV} \sum_l \langle s_l u_{\rm t}'(s_l) \rangle \tag{2.2.1}$$

with $\rho = n/V$ being the number density, n the particle number, V the d-dimensional volume, $\hat{P}_{\rm ex}$ the instantaneous pressure and $\langle \ldots \rangle$ indicating the thermal average over the configuration ensemble. (A prime denotes a derivative of a function with respect to its argument.) By taking the derivative of the truncated potential

$$u_{\rm t}'(s) = u'(s)H(s_{\rm c} - s) - u(s)\delta(s - s_{\rm c}) \tag{2.2.2}$$

the excess pressure may be written as the sum $P_{\rm ex} = \tilde{P}_{\rm ex} + \Delta P_{\rm ex}$ of an uncorrected (bare) contribution $\tilde{P}_{\rm ex}$ and an impulsive correction $\Delta P_{\rm ex}$. The latter correction is obtained numerically from [21]

$$\begin{aligned} \Delta P_{\rm ex} &= \lim_{s \to s_{\rm c}^-} h_1(s) \text{ with} \\ h_1(s) &\equiv \frac{1}{dV} \sum_l \langle s_l u(s_l)\ \delta(s_l - s) \rangle \end{aligned} \tag{2.2.3}$$

being a weighted histogram. In practice, the proper limit $s \to s_{\rm c}^-$ may be replaced by setting $s = s_{\rm c}$ in $h_1(s)$.

Shifted potential. The impulsive correction related to first derivatives of the truncated potential can be avoided by considering the shifted potential $u_{\rm s}(s)$, Eq. (2.1.3), since $u_{\rm s}'(s) = u'(s)H(s_{\rm c} - s)$. With this choice *no* impulsive correction arises either for similar

observables such as, e.g., moments of the instantaneous excess pressure tensor

$$\begin{aligned} \hat{P}_{\rm ex}^{\alpha\beta} &= -\frac{1}{V}\sum_l s_l^\alpha \frac{\partial u_{\rm s}(s_l)}{\partial s_l^\beta} \\ &= -\frac{1}{V}\sum_l s_l u_{\rm s}'(s_l)\ n_l^\alpha n_l^\beta \end{aligned} \tag{2.2.4}$$

where s_l^α stands for the spatial component α of the reduced distance between the particles and $n_l^\alpha = s_l^\alpha/s_l$ for the corresponding component of the normalized distance vector. Greek letters are used for the spatial coordinates $\alpha, \beta, \gamma, \delta = 1, \ldots, d$. (Note that $\hat{P}_{\rm ex} = {\rm Trace}[\hat{P}_{\rm ex}^{\alpha\beta}]/d$.) Specifically, if the potential is shifted, all impulsive corrections are avoided for the excess pressure fluctuations

$$C_{\rm F}^{\alpha\beta\gamma\delta} \equiv -\beta V \left(\left\langle \hat{P}_{\rm ex}^{\alpha\beta} \hat{P}_{\rm ex}^{\gamma\delta} \right\rangle - \left\langle \hat{P}_{\rm ex}^{\alpha\beta} \right\rangle \left\langle \hat{P}_{\rm ex}^{\gamma\delta} \right\rangle \right) \tag{2.2.5}$$

($\beta \equiv 1/k_{\rm B}T$ being the inverse temperature) which give important contributions — especially for polymer-type liquids [25] and amorphous solids [81] — to the elastic moduli computed using the stress-fluctuation formalism [21, 80]. Please note that since the stress is a two-point correlation function between the particles of the system, $C_{\rm F}^{\alpha\beta\gamma\delta}$ contains also in general three-point and four-point correlations.

2.2.2 Key point made

Correction to the Born term. Another important contribution to the elastic moduli is given by the Born term $C_{\rm B}^{\alpha\beta\gamma\delta}$, already mentioned in the Introduction.[1] Being a moment of the first and the second derivatives of the potential it is defined as [75, 21, 80, 25, 64]

$$C_{\rm B}^{\alpha\beta\gamma\delta} = \frac{1}{V}\sum_l \left\langle \left(s_l^2 u_{\rm s}''(s_l) - s_l u_{\rm s}'(s_l) \right) n_l^\alpha n_l^\beta n_l^\gamma n_l^\delta \right\rangle \tag{2.2.6}$$

using the notations given above. For solids with well-defined reference positions and displacement fields the Born contribution is known to describe the energy change due to an *affine* response to an imposed homogeneous strain [80, 81, 64]. Assuming now a truncated and shifted potential the impulsive correction $\Delta C_{\rm B}^{\alpha\beta\gamma\delta}$ to $C_{\rm B}^{\alpha\beta\gamma\delta} = \tilde{C}_{\rm B}^{\alpha\beta\gamma\delta} + \Delta C_{\rm B}^{\alpha\beta\gamma\delta}$ is simply obtained using

$$u_{\rm s}''(s) = u''(s) H(s_{\rm c} - s) - u'(s)\delta(s - s_{\rm c}) \tag{2.2.7}$$

[1] Apart from the Born term $C_{\rm B}^{\alpha\beta\gamma\delta}$ and the stress-fluctuation term $C_{\rm F}^{\alpha\beta\gamma\delta}$ there is a kinetic contribution $C_{\rm K}^{\alpha\beta\gamma\delta}$ and in pre-stressed systems (as in the systems considered numerically by us) an explicit contribution from the applied stress to the experimentally relevant elastic moduli resulting from an infinitesimal strain applied to the reference state [21, 75, 25].

which yields

$$\begin{aligned} \Delta C_{\mathrm{B}}^{\alpha\beta\gamma\delta} &= -\lim_{s\to s_{\mathrm{c}}^-} h_2^{\alpha\beta\gamma\delta}(s) \text{ with} \\ h_2^{\alpha\beta\gamma\delta}(s) &\equiv \frac{1}{V}\sum_l \left\langle s_l^2 u'(s_l) n_l^\alpha n_l^\beta n_l^\gamma n_l^\delta \; \delta(s_l - s)\right\rangle . \end{aligned} \tag{2.2.8}$$

General impulsive corrections. More generally, one might consider a property

$$A = \frac{1}{V}\sum_l \left\langle f(s_l) u_{\mathrm{s}}^{(n)}(s_l)\right\rangle \tag{2.2.9}$$

with $f(s)$ being a specified function and (n) denoting the n-th derivative of the shifted potential $u_{\mathrm{s}}(s)$. Let us further suppose that all potential derivatives up to the $(n-2)$-th one do vanish at the cutoff s_{c}. It thus follows that $A = \tilde{A} + \Delta A$ takes an impulsive correction

$$\begin{aligned} \Delta A &= -\lim_{s\to s_{\mathrm{c}}^-} h_n(s) \text{ with} \\ h_n(s) &\equiv \frac{1}{V}\sum_l \left\langle f(s_l) u^{(n-1)}(s_l) \; \delta(s_l - s)\right\rangle \end{aligned} \tag{2.2.10}$$

being the relevant histogram.

Generalized shifting. Obviously, the original potential can not only be shifted by a constant $u(s_{\mathrm{c}})$ but by a polynomial of s to make the first and arbitrarily high derivatives of the potential vanish at $s = s_{\mathrm{c}}$. In this way, all impulsive corrections could be avoided in principle. Since discontinuous forces at the cutoff may cause problems in MD simulations, a number of studies use, e.g., a "shifted-force potential" where a linear term is added to the potential [20, 91]. The difference between the original potential and the generalized shifted potential removing the cutoff discontinuities means, of course, that the computed properties deviate to some extent from the original model. Only if the generalized shifting is weak, one may recover the correct thermodynamic properties using a first-order perturbation scheme [20]. Since the (simply) shifted potential $u_{\mathrm{s}}(s)$, Eq. (2.1.3), is anyway the most common choice in simulations [25, 63, 64, 65, 76, 77, 81, 82, 83], let us restrict the presentation on this case and demonstrate how the impulsive correction associated to the non-vanishing $u_{\mathrm{s}}'(s_{\mathrm{c}}^-)$ can be computed.

2.2.3 Isotropic systems

Lamé coefficients. In order to show that the above mentioned impulsive corrections may be of relevance computationally I focus now on homogeneous and isotropic systems. It is assumed that not only the material properties but also the external load is isotropic,

i.e. the mean imposed pressure tensor is given by

$$\left\langle \hat{P}_{\rm ex}^{\alpha\beta} \right\rangle = P\ \delta_{\alpha\beta}. \tag{2.2.11}$$

The two elastic Lamé coefficients λ and μ [75] characterizing their elastic properties may then be computed numerically using [25]

$$\begin{aligned} \lambda &= \lambda_{\rm F} + \lambda_{\rm B}, \\ \mu - P_{\rm id} &= \mu_{\rm F} + \mu_{\rm B} \end{aligned} \tag{2.2.12}$$

where the only contribution due to the kinetic energy of the particles is contained by the ideal gas pressure $P_{\rm id}$ indicated for μ. Note that the trivial kinetic energy contributions to the elastic moduli are removed as far as possible from the presentation since MC results are also considered here. The first contributions indicated on the right hand-side of Eq. (2.2.12) are the excess pressure fluctuation contributions $\lambda_{\rm F}$ and $\mu_{\rm F}$ which may be obtained from the general $C_{\rm F}^{\alpha\beta\gamma\delta}$ by setting, e.g., $\alpha = \beta = 1$ and $\gamma = \delta = 2$ for $\lambda_{\rm F}$ and $\alpha = \gamma = 1$ and $\beta = \delta = 2$ for $\mu_{\rm F}$ characterizing the shear stress fluctuations. The "Born-Lamé coefficients" [25]

$$\lambda_{\rm B} \equiv \mu_{\rm B} \equiv \frac{1}{d(d+2)V} \sum_l \left\langle s_l^2 u''(s_l) - s_l u'(s_l) \right\rangle \tag{2.2.13}$$

may be obtained from the general Born terms $C_{\rm B}^{\alpha\beta\gamma\delta}$ by setting, e.g., $\alpha = \gamma = 1$ and $\beta = \delta = 2$. The d-dependent prefactor stems from the assumed isotropy of the system and the mathematical formula [74]

$$\left\langle \left(n_l^\alpha n_l^\beta \right)^2 \right\rangle = \frac{1}{d(d+2)} \left(1 + 2\delta_{\alpha\beta} \right) \tag{2.2.14}$$

($\delta_{\alpha\beta}$ being the Kronecker symbol [74]) for the components of a unit vector in d dimensions pointing into arbitrary directions. Equation (2.2.8) implies then an impulsive correction

$$\begin{aligned} \Delta\lambda_{\rm B} &= \Delta\mu_{\rm B} = -\lim_{s \to s_{\rm c}^-} h_2(s) \text{ with} \\ h_2(s) &\equiv \frac{1}{d(d+2)V} \sum_l \left\langle s_l^2 u'(s_l)\ \delta(s_l - s) \right\rangle . \end{aligned} \tag{2.2.15}$$

The histogram $h_2(s)$ is called below "weighted (radial) pair distribution function" since it is related to the standard radial pair distribution function $g(r)$ [11] as further discussed in Sec. 2.2.5.

Compression and shear modulus. Instead of using the Lamé coefficients it is from the experimental point of view more natural to characterize isotropic bodies using the compression modulus K and the shear modulus G. The latter moduli may be expressed as [75]

$$K = (\lambda + P) + \frac{2}{d}G, \tag{2.2.16}$$
$$G = \mu - P = \mu_{\rm B} + \mu_{\rm F} - P_{\rm ex} \tag{2.2.17}$$

with $P = P_{\rm id} + P_{\rm ex}$ being the total imposed mean pressure. I follow here the notation of Ref. [25] to emphasize the explicit pressure dependence which is often (incorrectly) omitted as clearly pointed out by Birch [92] and Wallace [75]. Using symmetry considerations Eq. (2.2.16) can be refomulated to a numerically more straightforward expression first stated by Rowlinson [10, 20]

$$K = P + \eta_{\rm B} - \eta_{\rm F}. \tag{2.2.18}$$

Here, the second term $\eta_{\rm B}$ stands for the so-called "hypervirial" [20]

$$\eta_{\rm B} \equiv \lambda_{\rm B} + \frac{2}{d}\left(\mu_{\rm B} - P_{\rm ex}\right) \tag{2.2.19}$$
$$= \frac{1}{d^2 V}\sum_l \left\langle s_l^2 u_{\rm s}''(s_l) + s_l u_{\rm s}'(s_l)\right\rangle \tag{2.2.20}$$

in agreement with Eq. (2.2.1) and Eq. (2.2.13). The last term

$$\eta_{\rm F} \equiv (-\lambda_{\rm F}) + \frac{2}{d}(-\mu_{\rm F}) \tag{2.2.21}$$
$$= \beta V\left(\left\langle \hat{P}_{\rm ex}^2\right\rangle - \left\langle \hat{P}_{\rm ex}\right\rangle^2\right) \tag{2.2.22}$$

characterizes the fluctuation of the excess pressure $\hat{P}_{\rm ex}$. As one expects, kinetic elastic contributions terms do not enter explicitly for the shear modulus G in Eq. (2.2.17). (An ideal gas does not have a finite shear modulus.) Since only the Born contributions $\lambda_{\rm B} = \mu_{\rm B}$ or $\eta_{\rm B}$ require a cutoff correction, this implies $K = \tilde{K} + \Delta K$ and $G = \tilde{G} + \Delta G$ with $\tilde{K}$ and $\tilde{G}$ being the uncorrected (bare) moduli and

$$\Delta K = \Delta\lambda_{\rm B} + \frac{2}{d}\Delta\mu_{\rm B} = \frac{2+d}{d}\Delta\mu_{\rm B}, \tag{2.2.23}$$
$$\Delta G = \Delta\mu_{\rm B} \tag{2.2.24}$$

being the impulsive corrections. We shall test these predictions numerically in Sec. 2.3.

2.2.4 Polydispersity and mixed potentials

As stated in the Introduction, we assume throughout this Chapter the scaling $U(r) \equiv u(s)$ of the pair potential in terms of the reduced distance $s = r/\sigma_l$. This is done not only for dimensional reasons but, more importantly, to describe a broad range of model systems for mixtures and polydisperse systems where σ_l may differ for each interaction l. Moreover, the type and/or the parameter set of the pair potential may vary for different interactions. For such mixed potentials $u(s)$, $u_{\mathrm{t}}(s)$ and $u_{\mathrm{s}}(s)$ and their derivatives take in principal an explicit index l, i.e. one should write $u_l(s)$, $u_{\mathrm{t},l}(s)$, $u_{\mathrm{s},l}(s)$ and so on. This is not done here to keep a concise notation. For example one might wish to consider

- a generic polymer bead-spring model where some interactions l describe the bonding between monomers along the chain (which are normally not truncated and need not to be corrected) and the truncated excluded volume interactions between the monomers [53];

- the generalization of the monodisperse LJ potential, Eq. (2.1.1), to a mixture or polydisperse system with

$$u_l(s) = 4\epsilon_l \left(s^{-12} - s^{-6}\right) \text{ with } s = r/\sigma_l \tag{2.2.25}$$

  where ϵ_l and σ_l are fixed for each interaction l. In practice, each particle i may be characterized by an energy scale E_i and a "diameter" D_i. The interaction parameters $\epsilon_l(E_i, E_j)$ and $\sigma_l(D_i, D_j)$ are then given in terms of specified functions of these properties [64];

- the extensively studied Kob-Andersen (KA) model for binary mixtures of beads of type A and B [63], a particular case of Eq. (2.2.25) with fixed interaction ranges σ_{AA}, σ_{BB} and σ_{AB} and energy parameters ϵ_{AA}, ϵ_{BB} and ϵ_{AB} characterizing, respectively, AA-, BB- and AB-contacts;

- a network forming emulsion of oil droplets in water bridged by telechelic polymers where the oil droplets are modeled as big LJ spheres, the telechelic polymers by a bead-spring model with a soluble "spacer" in the middle of the chain and insoluble end-groups ("stickers") strongly attracted by the oil droplets [58, 59]. Assuming sufficiently strong (in strength, number and life-time) sticker-oil interactions, such a system behaves as a soft solid with a finite shear modulus G (at least for a fixed finite sampling time) which may be probed, at least in principle, using Eq. (2.2.17).

The impulsive corrections given in Eq. (2.2.3) for the pressure P, in Eq. (2.2.8) for the general Born term $C_{\mathrm{B}}^{\alpha\beta\gamma\delta}$ and in Eq. (2.2.15) for the Born Lamé coefficients $\lambda_{\mathrm{B}} = \mu_{\mathrm{B}}$ have been stated in terms of, respectively, the weighted histograms $h_1(s)$, $h_2^{\alpha\beta\gamma\delta}(s)$ and

$h_2(s)$. These expressions remain valid for explicitly l-dependent potentials and, from the numerical point of view, this is all what is needed. The direct computation of these histograms remains in all cases straightforward as illustrated in Sec. 2.3.1.

2.2.5 Radial pair distribution function $g(r)$

Notations. For isotropic systems it is common practice to reexpress correlations and histograms in terms of the radial pair distribution function $g(r)$ [10, 11]. This is also of interest here since for large cutoff distances the pair distribution function must drop out, $g(r_c) \to 1$, allowing thus to predict the corrections in this limit. Let us remind first that, that using the Gamma function $\Gamma(x)$ [74], the $(d-1)$-dimensional surface of a d-sphere of radius r is given by

$$A(r) = \frac{2\pi^{d/2}}{\Gamma(d/2)}\, r^{d-1} \text{ for } d = 2, 3, \ldots \tag{2.2.26}$$

and similarly for the (dimensionless) surface $A(s)$ using the reduced distance s.

Monodisperse interactions. For strictly monodisperse particles and similar interactions of constant interaction range σ it is seen that Eq. (2.2.3) for the pressure correction becomes

$$\Delta P_{\text{ex}} = \frac{1}{2}\,\frac{1}{d}\rho^2\sigma^d A(s_c) s_c u(s_c) \times g(s_c) \tag{2.2.27}$$

where the factor $1/2$ assures that every interaction is only counted once. For the LJ potential, Eq. (2.1.1), this leads to

$$\Delta P_{\text{ex}} = -\frac{4\pi^{d/2}}{\Gamma(d/2)d}\left(\rho\sigma^d\right)^2 \frac{\epsilon}{\sigma^d} s_c^{d-6}(1 - s_c^{-6}) \times g(s_c). \tag{2.2.28}$$

Please note that Eq. (3.2.7) given in Ref. [21] is recovered by setting $d = 3$ and assuming $g(s_c) \approx 1$. Similarly, one obtains from Eq. (2.2.15) the correction

$$\Delta\mu_{\text{B}} = -\frac{1}{2}\,\frac{1}{d(d+2)}\rho^2\sigma^d A(s_c) s_c^2 u'(s_c) \times g(s_c) \tag{2.2.29}$$

for the Born-Lamé coefficient. For a LJ potential this becomes

$$\Delta\mu_{\text{B}} = -\frac{24\pi^{d/2}}{d(d+2)\Gamma(d/2)}\left(\rho\sigma^d\right)^2 \frac{\epsilon}{\sigma^d} f_{\text{LJ}}(s_c) \times g(s_c) \tag{2.2.30}$$

where I have defined

$$f_{\text{LJ}}(s) \equiv (1 - (s_0/s)^6)/s^{6-d} \tag{2.2.31}$$

with $s_0 = 2^{1/6}$ being the minimum of the potential. Note that $\Delta\mu_{\rm B}$ vanishes for $s \to s_0$. For sufficiently large cutoff distances where $g(s_{\rm c}) \approx 1$ the correction decays as

$$\Delta\mu_{\rm B} \sim -A(s_{\rm c}) s_{\rm c}^2 u'(s_{\rm c}), \tag{2.2.32}$$

e.g. $\Delta\mu_{\rm B} \sim -1/s_{\rm c}^{6-d}$ for a LJ potential. (Only for $d < 6$ the cutoff correction vanishes in the large-s limit.) This asymptotic behavior also holds for the more complicated cases discussed below.

Mixtures. Many experimentally relevant systems have mixed potentials, such as the KA model for binary mixtures sketched above. In general, the interaction potential $U_{ab}(r) = u_{ab}(s)$ between beads of two species a and b takes different energy parameters which causes different weights at the cutoff depending on which particles interact. The impulsive corrections of such mixtures are readily obtained by linear superposition of Eq. (2.2.29) for different contributions (a, b). Let $c_a = \rho_a/\rho$ denote the mole fraction of species a, σ_{ab} the interaction range between a bead of type a and a bead of type b and $g_{ab}(s)$ the respective radial pair distribution function. The impulsive correction to the Born-Lamé coefficient thus becomes

$$\begin{aligned} \Delta\mu_{\rm B} &= -\frac{1}{2}\frac{1}{d(d+2)}\rho^2 A(s_{\rm c}) s_{\rm c}^2 \\ &\times \sum_a \sum_b c_a c_b \sigma_{ab}^d u'_{ab}(s_{\rm c})\; g_{ab}(s_{\rm c}) \end{aligned} \tag{2.2.33}$$

where I have used that for all types of interaction we have the *same* reduced cutoff $s_{\rm c}$.

Let us now assume a mixture described by the generalized LJ potential $u_{ab}(s) = 4\epsilon_{ab}(1/s^{12} - 1/s^6)$ with $s = r/\sigma_{ab}$. A reference energy $\epsilon_{\rm ref}$ and a reference interaction range $\sigma_{\rm ref}$ may arbitrarily be defined using, say, the interaction of two beads of type $a = b = 1$, i.e. $\epsilon_{\rm ref} \equiv \epsilon_{11}$ and $\sigma_{\rm ref} \equiv \sigma_{11}$. Defining the dimensionless ratios $w_{ab} \equiv \epsilon_{ab}/\epsilon_{\rm ref}$ and $v_{ab} = (\sigma_{ab}/\sigma_{\rm ref})^d$ one may thus rewrite the general Eq. (2.2.33) as

$$\begin{aligned} \Delta\mu_{\rm B} &= -\frac{24\pi^{d/2}}{d(d+2)\Gamma(d/2)} \left(\rho\sigma_{\rm ref}^d\right)^2 \frac{\epsilon_{\rm ref}}{\sigma_{\rm ref}^d}\; f_{\rm LJ}(s_{\rm c}) \\ &\times \sum_a \sum_b c_a c_b v_{ab} w_{ab}\; g_{ab}(s_{\rm c}). \end{aligned} \tag{2.2.34}$$

Since $g_{ab}(s_{\rm c}) \to 1$ for large $s_{\rm c}$, the function $f_{\rm LJ}(s_{\rm c})$ determines the scaling as already stated above, Eq. (2.2.32).

Continuous polydispersity. I turn now to systems with a continuous polydispersity as in the second model investigated numerically below. Let us assume that each bead is characterized by a bead diameter D which is distributed according to a well-defined

s_c/s_0	$e\beta$	$P\beta/\rho$	$\tilde{K}\beta/\rho$	$K\beta/\rho$	$\tilde{G}\beta/\rho$	$\Delta\mu_B\beta/\rho$	$K\beta/\rho$
0.9	0.255	5.08	-20.4	17.7	-18.95	19.05	17.4
1.0	0.523	6.01	22.5	22.5	0.03	0.03	22.4
1.1	0.176	5.46	24.2	20.4	1.97	-1.92	20.6
1.5	-1.79	3.61	17.6	16.7	0.36	-0.43	16.8
2.0	-2.43	3.17	16.7	16.1	0.31	-0.32	16.0
2.5	-2.64	3.01	15.8	15.6	0.08	-0.10	15.7
3.0	-2.72	2.95	15.6	15.5	0.08	-0.06	15.5
3.5	-2.75	2.93	15.6	15.5	0.02	-0.03	15.3
4.0	-2.77	2.92	15.7	15.7	0.03	-0.02	15.5

Table 2.1: Some properties of pLJ beads at temperature $T = 1$ and density $\rho \approx 0.72$ for several computed values of the reduced cutoff distance s_c/s_0 with $s_0 = 2^{1/6}$ being the minimum of the potential: energy per bead e, total pressure $P = P_{id} + P_{ex}$, uncorrected compression modulus $\tilde{K}$, corrected compression modulus $K = \tilde{K} + 2\Delta\mu_B$, bare shear modulus $\tilde{G}$ and impulsive correction $\Delta\mu_B$ obtained from the histogram $h_2(s)$ at $s = s_c$. The corrected shear modulus $G = \tilde{G} + \Delta G$ vanishes as it should. The last column refers to the compression modulus K obtained using Eq. (2.3.1) for isobaric ensembles kept at the same pressure P (third column).

normalized distribution c_t with $t = D/\sigma_{ref}$ being a reduced bead diameter with respect to some reference length σ_{ref}. To be specific let us assume a generalized LJ potential, Eq. (2.2.25), where the interaction range $\sigma_{tt'}$ and the energy scale $\epsilon_{tt'}$ between two beads are uniquely specified by the two reduced diameters t and t'. Defining $w_{tt'} = \epsilon_{tt'}/\epsilon_{ref}$, $v_{tt'} = (\sigma_{tt'}/\sigma_{ref})^d$ and using the radial pair distribution function $g_{tt'}(s)$ for two beads of reduced diameter t and t', the double-sum in Eq. (2.2.34) can be rewritten as the double-integral

$$\begin{aligned} \Delta\mu_B &= -\frac{24\pi^{d/2}}{d(d+2)\Gamma(d/2)} \left(\rho\sigma_{ref}^d\right)^2 \frac{\epsilon_{ref}}{\sigma_{ref}^d}\, f_{LJ}(s_c) \\ &\times \int dt \int dt'\; c_t c_{t'} v_{tt'} w_{tt'}\; g_{tt'}(s_c). \end{aligned} \tag{2.2.35}$$

In order to determine $\Delta\mu_B$ from Eq. (2.2.35) one needs to prescribe the laws for c_t, $\sigma_{tt'}$ and $\epsilon_{tt'}$. In the large-s_c limit the double-integral becomes in any case constant, i.e. we have again $\Delta\mu_B \sim -f_{LJ}(s_c) \sim -1/s_c^{6-d}$.

2.3 Computational results

2.3.1 Weighted pair distribution function $h_2(s)$

The weighted radial pair distribution function $h_2(s)$, Eq. (2.2.15), is presented in Fig. 2.1. Several cutoff distances s_c are given for the pLJ model, but for clarity only for distances $s \le s_c$. For the KA model only one cutoff is given, but this also for $s > s_c$. Note that

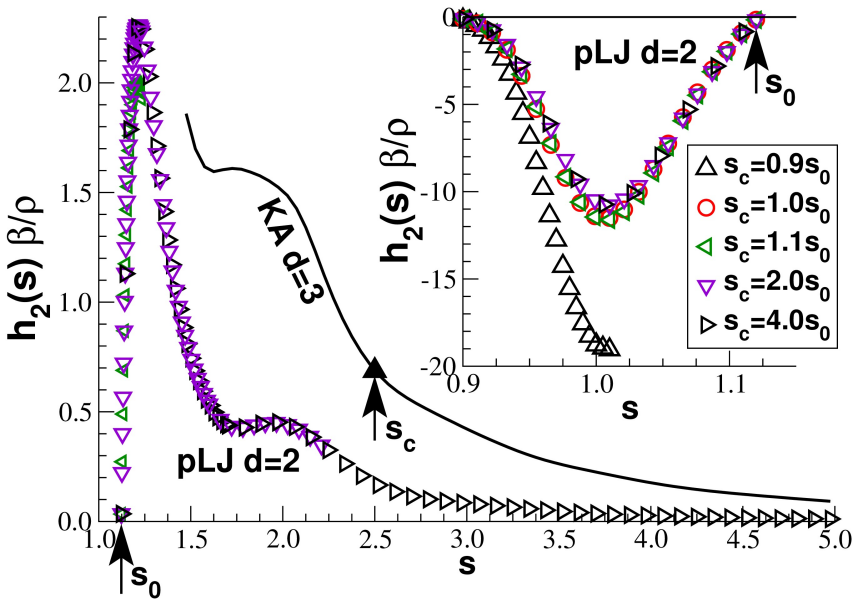

Figure 2.1: Weighted radial pair distribution function $h_2(s)\beta/\rho$ with $s = r/\sigma_l$ being the reduced distance between two beads i and j. Main panel: KA mixtures in $d = 3$ (bold line) and pLJ beads in $d = 2$ (open symbols) for large reduced distances $s > s_0$ where the potential is attractive. The filled triangle corresponds to the shear modulus $\tilde{G}$ computed using Eq. (2.2.17) for the KA system not taken into account the impulsive correction. Inset: pLJ model for $s \leq s_0$ where $h_2(s)$ becomes strongly negative.

albeit different s_c for each model correspond strictly speaking to different state points — as better seen from the energies per particle e or total pressures P indicated in Table 2.1 — the histograms vary only weakly with s_c. Strong differences become only apparent for very small s_c as shown for $s_c = 0.9s_0$ in the inset. One can thus use the histogram obtained for one s_c to anticipate the impulsive correction for a different cutoff. Note that for large distances corresponding to an attractive interaction we have $h_2(s) > 0$ (main panel). Obviously, $h_2(s)$ vanishes at the minimum of the potential $s = s_0$ and for very large distances s. Since $g(s) \approx 1$ in the latter limit, the histogram $h_2(s)$ is given (up to a known prefactor) by $s^{d+1}u_s'(s)$. As one expects the decay is faster for the $d = 2$ data than for the KA mixtures in $d = 3$, since the phase volume at the cutoff is larger for the latter systems. Since all histograms are rather smooth, one may simply set $s = s_c$ for obtaining $\Delta\mu_B$ from $h_2(s)$ instead of properly taking the limit $s \to s_c^-$.

2.3.2 Compression modulus K

The compression modulus K may be obtained from Eq. (2.2.16) or, equivalently, using the Rowlinson formula Eq. (2.2.18). Note that if plotted as a function of the number of configuration sampled, the compression modulus for both models is seen to decrease first with sampling time t before leveling off at a finite value. Similar behavior has been observed for polymeric systems [25, 53]. All our systems are highly incompressible, i.e.

the compression modulus K is large as usual in condensed matter systems, and it is thus difficult to demonstrate the small correction predicted by Eq. (2.2.23). For the KA model we obtain, e.g. $\Delta K\beta/\rho \approx -(5/4) \times 0.69 \approx -1.2$ which compared to the uncorrected estimate $\tilde{K}\beta/\rho \approx 21.9$ is small.

More importantly, it is not easy to obtain an independent and precise K-value for canonical ensembles of mixtures and polydisperse systems using, e.g., the total particle structure factor [11, 53]. For the pLJ model we have thus computed K directly from the volume fluctuations δV in the isobaric ensemble [20]

$$K = k_{\rm B}T\frac{\langle V\rangle}{\langle \delta^2 V\rangle} \tag{2.3.1}$$

where the same (mean) pressure P is imposed as for the corresponding canonical ensemble. As described in Ref. [20] proposed volume fluctuations of the simulation box are accepted or rejected according to a Metropolis MC scheme. As may be seen from the last column indicated in Table 2.1, this yields within statistical accuracy the same values as the stress-fluctuation formula, Eq. (2.2.16), if the impulsion correction is taken into account. Unfortunately, for larger cutoffs our error bars (not shown) become too large to confirm the correction. The most striking example, where Eq. (2.2.23) can be shown to work, is the case of the small cutoff $s_{\rm c} = 0.9s_0$: Using Eq. (2.2.16) an impossible *negative* value $\tilde{K}\beta/\rho \approx -20.4$ is obtained. As may be seen from the inset in Fig. 2.1, one gets $\Delta\mu_{\rm B}\beta/\rho \approx 19.1$ from the weighted histogram $h_2(s)$. Taking the correction Eq. (2.2.23) into account this yields $K\beta/\rho \approx 17.7$ which is consistent with the value 17.4 obtained using the strain fluctuation formula Eq. (2.3.1).

2.3.3 Shear modulus G

Asymptotic limit for large sampling times. Since all our systems are liquids, the shear modulus G should of course vanish — at least in the thermodynamic limit for a sufficiently long sampling time. We have thus a clear reference and for this reason G is highly suitable to test the predictions. As can be seen from the solid triangle indicated in Fig. 2.1 for the KA mixtures with $s_{\rm c} = 2.5$ we obtain $\tilde{G}\beta/\rho \approx 0.65$ if the impulsive correction for the Born term is *not* taken into account. As also shown by the figure (thin line), this deviation equals $h_2(s_{\rm c} = 2.5)\beta/\rho \approx 0.69$ as predicted.

The same behavior is seen from Fig. 2.2 for pLJ beads for a broad range of cutoff distances $s_{\rm c}$ where the open squares refer to the uncorrected $\tilde{G}$ and the filled squares to G obtained using Eq. (2.2.24). The solid lines indicated show Eq. (2.2.35). Focusing on the scaling for large $s_{\rm c}$ we have set $g_{tt'}(s_{\rm c}) = 1$ in the double-integral which (under this assumption) is close to unity. Note that the correction $-\Delta\mu_{\rm B}$ (open spheres) is obtained with much higher numerical precision than it was possible for $\tilde{G}$. The error bars (not

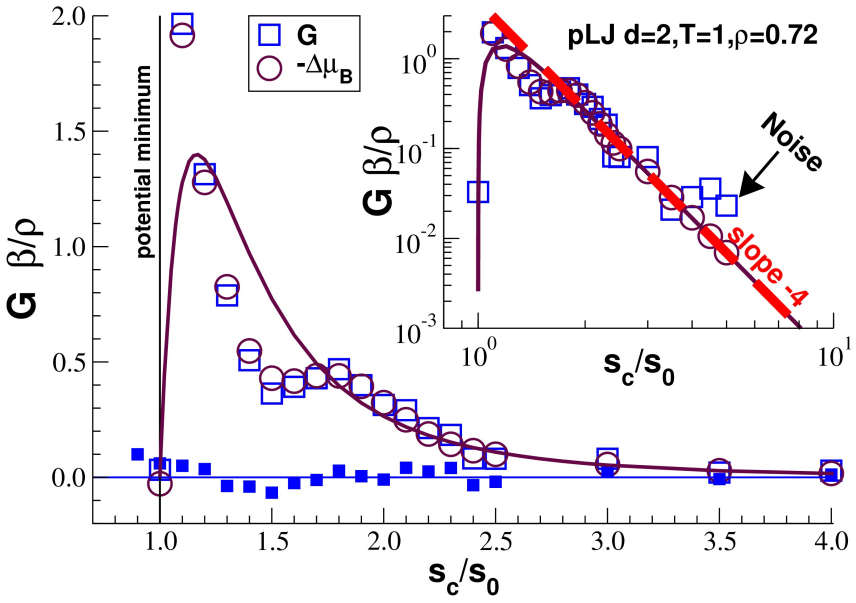

Figure 2.2: Shear modulus G and impulsive correction $-\Delta\mu_{\rm B}$ for the pLJ model *vs.* the reduced cutoff distance $s_{\rm c}/s_0$. The uncorrected shear modulus $\tilde{G}$ (open squares) has been obtained using the stress-fluctuation formula, Eq. (2.2.17), the correction term (spheres) from the histogram $h_2(s)$, Eq. (2.2.15). The solid lines indicate Eq. (2.2.35) where we have set $g_{tt'}(s_{\rm c}) = 1$. Main panel: Linear representation showing that $G = \tilde{G} + \Delta\mu_{\rm B}$ (filled squares) vanishes as predicted, Eq. (2.2.24). Inset: Double-logarithmic representation emphasizing the asymptotic power-law decay for large $s_{\rm c}$, Eq. (2.2.32), as indicated by the bold dashed line.

indicated) become larger than the signal below $\tilde{G}\beta/\rho \approx 0.05$.

Sampling time dependence. Figure 2.3 gives additional information on the shear modulus $G(t)$ plotted as a function of the number t of MC steps (MCS) for pLJ beads. Using time series where instantaneous properties relevant for the moments are written down every 10 MCS for total trajectories of length 10^7 MCS, all reported properties have been averaged using standard gliding averages [20], i.e. we compute mean values and fluctuations for a given time interval $[t_0, t_1 = t_0 + t]$ and average over all possible intervals of length t. For $s_{\rm c} = 0.9s_0$, where $\Delta\mu_{\rm B}\beta/\rho \approx 17.1$, the uncorrected data is negative and cannot be represented. Note that $G = \tilde{G}$ for $s_{\rm c} = 1.0s_0$ since $\Delta\mu_{\rm B} = 0$ for $s_{\rm c} = 1.0s_0$, Eq. (2.2.15). Since $\Delta\mu_{\rm B}$ is very small for $s_{\rm c} = 4.0s_0$, only the corrected values are represented. The filled symbols refer to the uncorrected shear modulus $\tilde{G}(t)$ for $s_{\rm c} = 1.1s_0$, $s_{\rm c} = 1.5s_0$ and $s_{\rm c} = 2.5s_0$ which are seen to approach for large times the predicted correction $-\Delta\mu_{\rm B}$ taken from the Table 2.1 (horizontal lines). If corrected, all data sets vanish properly with time. (The noise becomes again too large below $G(t)\beta/\rho \approx 0.05$.)

Interestingly, neither $\mu_{\rm B}$ nor $P_{\rm ex}$ do (essentially) depend on the sampling time t while the fluctuation contribution $-\mu_{\rm F}(t)$ approaches (the corrected) $\mu_{\rm B} - P_{\rm ex}$ from below (not shown). The corrected shear modulus $G(t)$ thus decreases monotonously with time. As

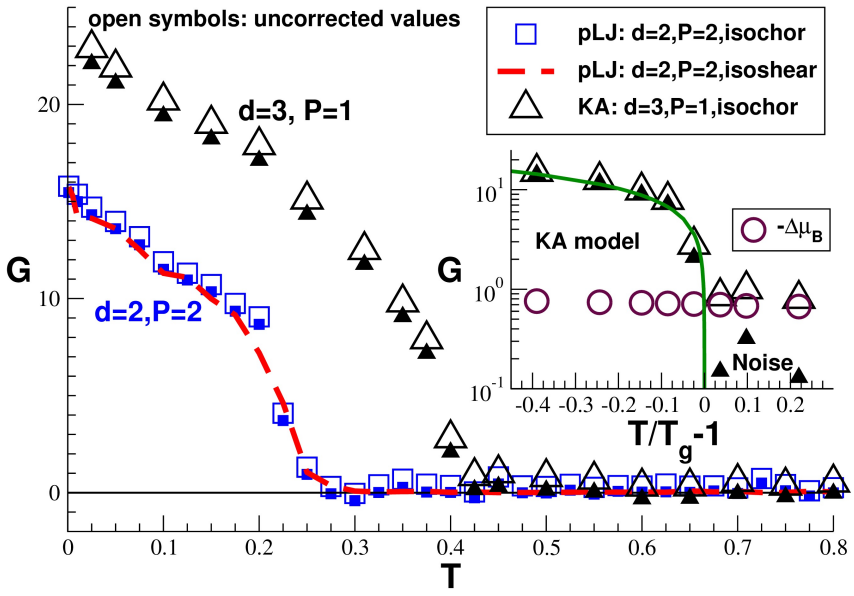

Figure 2.3: Shear modulus G for pLJ beads in $d = 2$ for different s_c as a function of the sampling time t given in units of MC Steps (MCS) of the local MC jumps used. The vertical axis is made dimensionless by means of a factor β/ρ. Filled symbols refer to the uncorrected $\tilde{G}(t)$. The horizontal lines indicate $-\Delta\mu_B$ obtained from the histograms $h_2(s)$ for three cutoffs as indicated in the Table 2.1. The dashed slope characterizes the decay of (the corrected) $G(t)$ with time.

can be seen from Fig. 2.3, $G(t)$ decays roughly as the power-law slope -1 indicated by the dashed line. Exactly the same behavior has been observed for the KA model in $d = 3$ (not shown). Apparently, $G(t)$ decays quite generally inversely as the mean-square displacement $h(t)$ of the beads in the free-diffusion limit, $h(t) \sim t$. I remind that the same scaling $G(t) \sim 1/h(t)$ has also been reported for a bead-spring polymer model without impulsive corrections ($s_c = s_0$) [53].

2.4 Discussion

2.4.1 Summary

Impulsive correction. It has been demonstrated in this Chapter that an impulsive correction to the Born contribution $C_B^{\alpha\beta\gamma\delta}$ of the elastic moduli must arise if the interaction potential is truncated and shifted, Eq. (2.1.3), with a non-vanishing first derivative at the cutoff. To test our theoretical predictions the elastic moduli of isotropic liquids in $d = 3$ and $d = 2$ dimensions has been computed. Since for these systems the shear modulus G must vanish by construction, this allows a precise numerical verification for different reduced cutoff distances s_c (Fig. 2.2). It has been shown how the impulsive correction for mixtures and polydisperse systems may be obtained from the weighted histogram $h_2(s)$ which scales as $h_2(s) \sim s^{d+1}u'(s)$ for large s. As one expects, the cutoff effect vanishes if s_c

is large, Eq. (2.2.32), or set to the minimum of the potential. It becomes more important with increasing spatial dimension.

General validity of the stress-fluctuation formalism. It should be reminded that the stress-fluctuation formula $G = \mu - P = \mu_{\mathrm{B}} + \mu_{\mathrm{F}} - P_{\mathrm{ex}}$ and several other relations used in this work for *liquid* systems were originally formulated for *solids* assuming well-defined reference positions and displacement fields [76, 84]. By revisiting the derivation [10] for the compression modulus K for simple liquids, Eq. (2.2.18), for general elastic moduli (as in fact already done by Lutsko [80]), it can be seen that these assumptions can be relaxed and especially Eq. (2.2.17) must hold quite generally for isotropic systems [4]. One additional goal of the presented paper [7] was to show numerically that the stress-fluctuation formalism yields the right value ($G = 0$), *once* the impulsive correction has been taken into account.

2.4.2 Further generalizations and related issues

The generalization of our results to

- other elastic moduli in anisotropic systems using the more general impulsive correction, Eq. (2.2.8);
- observables related to even higher derivatives of the potential, Eq. (2.2.10);
- local and inhomogeneous elastic moduli which have been argued to be of relevance for the plastic failure under external load [82, 84, 65];
- more complicated interaction potentials, not necessarily scaling simply with $s = r/\sigma_l$;
- general non-pair interactions using the generalization of the Born term derived by Ray [78] and studied, e.g., numerically by Yoshimoto *et al.* [83]

is straightforward and should be considered in future work.[2]

2.4.3 Shear modulus near the glass transition

The presented approach has been used in Ref. [4] to characterize as a function of temperature, imposed pressure and sampling time the elastic properties of the two models discussed here. Some results of this work are given in Fig. 2.4. Following the procedure described in Ref. [25], the data have been obtained for systems which are cooled through

[2] A similar, albeit very small, impulsive correction arises for the "configurational temperature" being the ratio of the mean-squared forces acting on the particles and the mean divergence of these forces. See Eq. (7.2.11) of Ref. [11].

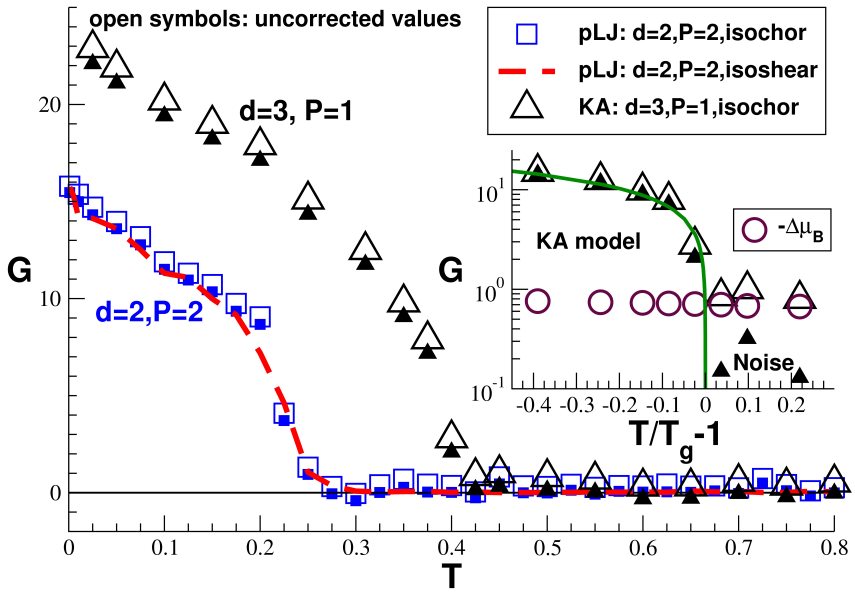

Figure 2.4: Shear modulus G as a function of temperature T for the KA model ($P \approx 1$, $s_c = 2.5$, $T_g \approx 0.41$) and the pLJ model ($P \approx 2$, $s_c = 2.0s_0$, $T_g \approx 0.27$). The uncorrected values are represented by open symbols, the corrected values by small filled symbols. Main panel: The dashed line represents the shear modulus obtained from the shear strain fluctuations in simulation boxes with shape deformations, Eq. (2.4.1). Inset: Half-logarithmic representation for $G(T)$ for the KA model focusing on the behavior around T_g. The transition becomes rather sharp if the impulsive correction is taken into account as emphasized by the solid line indicating Eq. (2.4.2). Note that $-\Delta\mu_B$ (spheres) increases only weakly with decreasing T.

the glass transition at constant pressure P, i.e. allowing first the volume to fluctuate as in Sec. 2.3.2.[3] The glass transition temperature T_g of both systems is either known [63] or may be determined, e.g., from the density $\rho(T)$ [25]. Imposing then a constant (mean) temperature and a simulation box of fixed volume and shape, the shear modulus is computed using the stress-fluctuation formula Eq. (2.2.17) for the canonical ensemble. The bare moduli $\tilde{G}$ (open squares and triangles) are clearly seen to be finite for all T, while the corrected moduli $G = \tilde{G} + \Delta\mu_B$ vanish for all $T > T_g$. That this is indeed the case is better seen from the half-logarithmic representation shown in the inset for the KA model. Decreasing the temperature further below T_g the shear moduli are seen to increase rapidly for both models.[4] As above for the compressibility K in Sec. 2.3.2, we have crosschecked the values obtained from the stress-fluctuations in the canonical ensemble by directly measuring G from the shear strain γ (in the xy-plane) in deformable

[3]For systems with finite mean shear stress various stress-fluctuation formulae must be changed and especially Eq. (2.2.17) for the shear modulus G must be modified.

[4]It is well known that two-point correlations, as measured by the pair correlation function $g(r)$, do barely change at the glass transition [16]. Please note that the shear modulus G computed according to Eq. (2.2.17) is a properly defined thermodynamic correlation function characterizing not only two-point, but also three-point and four-point correlations. Apparently, these higher *static* correlations change qualitatively at the glass transition.

simulation boxes at constant volume. As discussed in the literature [20, 21, 84], we use a non-Euklidean metric tensor constructed from the so-called h-matrix describing the box shape, and change the shear strain γ according to a Metropolis MC scheme [20] similar to the changes of the box volume V in Sec. 2.3.2. Imposing a zero mean shear-stress for the shear strain fluctuations the modulus G can be obtained from the thermodynamic formula

$$G = \frac{k_{\rm B}T/V}{\langle\gamma^2\rangle - \langle\gamma\rangle^2} \tag{2.4.1}$$

which corresponds to Eq. (2.3.1) for volume fluctuations in the isobaric ensemble.[5] As shown for the pLJ model by the dashed line in the main panel of Fig. 2.4, this yields for all T, even for deeply quenched glasses, within numerical accuracy the *same* values as the stress-fluctuation formula *if* the impulsive corrections are taken into account. As shown by the solid line in the inset, the KA model is well fitted by a cusp-singularity

$$G(T) \approx G_0 \left(1 - T/T_{\rm g}\right)^{1/2} \text{ for } T < T_{\rm g} \tag{2.4.2}$$

with an empirical constant $G_0 \approx 23$. This suggests that the transition is very sharp albeit continuous in agreement with replica theory [87, 89]. Note that the number of data points close to $T_{\rm g}$ is, however, not sufficient to rule out completely the additive off-set suggested by MCT [16]. Thus, at present it is impossible to distinguish between the different theoretical scenarios proposed [16, 87, 88, 89]. In any case, it should be clear from Fig. 2.4 that a high-precision numerical characterization of the scaling of $G(T)$ around $T_{\rm g}$ necessitates the proper taking into account of the impulsive corrections.

[5] Since such a thermodynamic relation may be questioned for the strongly frozen systems, we have also determined G using the mechanical definition by linear regression from the observed conjugated instantaneous shear strain and stress. This yields the *same* values as Eq. (2.4.1).

Chapter 3

Hyperbranched polymers with Gaussian statistics

3.1 Introduction

Hyperbranched stars with Gaussian chain statistics. Regular exponentially growing starburst dendrimers, as sketched in Fig. 1.1, and more general starlike hyperbranched chains[1] with Gaussian chain statistics have been considered theoretically early in the literature [26, 27, 93, 94, 95, 96] and have continued to attract attention up to the very recent past [95, 97, 98, 99, 100, 101, 102, 103, 104, 105, 106]. One reason for this is that highly branched polymers [107] with sufficiently large spacer chains between the branching points (indicated by the filled circles) are expected to be of direct experimental relevance under melt or θ-solvent conditions [12, 13, 14, 108].

Assuming a tree-like structure and translational invariance along the chain contour, the root-mean-square distance $R_{\rm s}$ between two arbitrary monomers n and m, as shown in panel (a), is given by

$$R_{\rm s}^2 \equiv \left\langle (\underline{r}_m - \underline{r}_n)^2 \right\rangle = b^2 s^{2\nu} \tag{3.1.1}$$

where ν is the inverse fractal dimension of the spacer chains, s the curvilinear distance along the tree between both monomers and b the statistical segment size of the spacer chains [13]. As a consequence, the typical distance $R_{\rm e}$ between the central monomer and the end monomers is one possible observable measuring the molecule size,[2] scales as $R_{\rm e}^2 = b^2 SG$ with S being the length of the spacer chains (assumed to be monodisperse). Other moments are obtained from the normalized distribution $P(r, s)$ of the distance

[1] For simplicity, we call "stars" or "branched stars" all tree-like branched architectures, "regular dendrimers" the deterministic and exponentially growing stars shown in panel (a) of Fig. 1.1 and "power-law stars" hyperbranched stars of finite fractal dimension $d_{\rm f}$.

[2] The curvilinear length SG from the central monomer to the end monomers may, of course, in general be irrelevant for a *broad* distribution of branch lengths. For all systems of interest here $R_{\rm e}$ is seen, however, to give a fair and simple estimate similar, e.g., to the radius of gyration $R_{\rm g}$, as further discussed in Sec. 3.4.

$r = |\underline{r}_m - \underline{r}_n|$ which, irrespective of the specific topology of the branched structure, is given by

$$P(r,s) = \left(\frac{d}{2\pi R_{\rm s}^2}\right)^{d/2} \exp\left(-\frac{d}{2}\left(\frac{r}{R_{\rm s}}\right)^2\right) \tag{3.1.2}$$

with $d = 3$ being the spatial dimension.[3] Due to their theoretical simplicity such Gaussian chain stars (including systems with *short-range* interactions along the topological network) allow to investigate several non-trivial conceptual and technical issues, both for static [99, 102] and dynamical [70, 100, 101, 103, 109, 111] properties, related to the in general intricate monomer connectivity imposed by the specific chemical reaction history.

Aim of current study. We assume here that *(i)* the chemical reaction is irreversible (quenched), *(ii)* all molecules are monodisperse of length form the root to the end monomer GS and *(iii)* flexible down to the monomer scale and *(iv)* that the branching at the ends of the spacer ends is at most three-fold ($f = 3$) as in the examples given in Fig. 1.1. The aim is *(i)* to revisit various experimentally relevant conformational properties in the limit where the total monomer mass N and the total number $M = (N-1)/S$ of spacer chains become sufficiently large to characterize the asymptotic *universal* behavior, *(ii)* to sketch for different starburst architectures in the regimes where the Gaussian spacer chain assumption becomes a reasonable approximation and *(iii)* to prepare some definitions and concepts we shall need in the next Chapter where static properties of dendrimer melts will be considered numerically. We will focus on the large-S limit since this allows under θ-solvent[4] or melt conditions to broaden the experimentally meaningful range of the generation number G of spacer chains.

Fractal dimension. One dimensionless property characterizing the star classes considered below is their fractal dimension $d_{\rm f}$ which may be defined as [112, 69]

$$d_{\rm f} \equiv \lim_{R\to\infty} \frac{\log(N)}{\log(R/b)} \tag{3.1.3}$$

with N being the mass and R the characteristic chain size. (Less formally, this definition is often written $N \sim R^{d_{\rm f}}$ [69].) For the regular branched dendrimers shown in panel (a) the number of spacers increases as $M_g \approx (f-1)^g$ with the generation number g, i.e. the total mass $N(G)$ increases exponentially with the total generation number G, while the typical

[3] Although we focus on three-dimensional systems the general dimension d is often indicated since this may help to clarify the structure of the relations. The reader is invited to replace d by $d = 3$. For similar reasons we often make explicit the inverse fractal dimension ν of the spacer chains. It should be replaced by its value $\nu = 1/2$.

[4] Due to effective three-body monomer interactions strongly branched stars may yet swell in the θ-regime. In the limit of large spacer chains this effect should become negligible, however, as for unbranched stars for which it has been shown that the renormalized interaction vanishes in the limit of infinitely long chains [108].

chain size $R(G) \sim \sqrt{G}$ only increases as a power-law. That the fractal dimension thus must diverge, is denoted below by the shorthand "$d_f = \infty$". We shall in addition consider star classes of *finite* fractal dimension d_f focusing especially on more fluffy, not too dense systems which should be (at least conceptionally) of experimental relevance. Specifically, let us consider *(i)* marginally compact chains [66] of fractal dimension $d_f = d = 3$ and *(ii)* stars of fractal dimension $d_f = 2.5$ which might be thought to be assembled by diffusion limited aggregation (DLA) [67, 68, 69, 70].

Power-law stars. As sketched in panel (b), such hyperbranched stars of finite fractal dimension may be constructed most readily by imposing a number of spacer chains M_g per generation g such that the power law $M_g \sim g^{\alpha-1}$ holds. The "growth exponent" α of these so-called "α-stars" is set by the fractal dimension

$$\alpha = d_f \nu \tag{3.1.4}$$

as may be seen using $N \sim R^{d_f}$ and $R \approx R_e \sim (SG)^\nu$. While being a natural generalization of the regular dendrimer case, restricting the branching of star arms does, unfortunately, not lead to a *self-similar* fractal tree since the iteration $g \to g + 1$ is not a proper self-similar generator acting on *all* spacer chains [69, 112]. We therefore also consider truly self-similar fractal and multifractal stars, called β- and γ-stars,[5] generated iteratively as shown in panel (c) and panel (d) of Fig. 1.1 by the iterative application of a well-defined generator (or several generators) on *all* the spacer chains as in the recent theoretical work on Vicsek fractals [97, 98]. For the latter architectures one thus expects to observe for the intramolecular coherent form factor $F(q)$ the power-law scaling [12, 15, 66]

$$F(q) \sim 1/q^{d_f} \text{ for } d_f \leq d = 3 \tag{3.1.5}$$

in the intermediate regime of the wavevector q. Note that Eq. (3.1.5) only holds for open or marginally compact structures [66, 15]. Porod-like scattering is, of course, expected for more compact star classes.

Outline. The presentation of this Chapter follows closely the recently submitted manuscript Ref. [54]. We summarize first in Sec. 3.2 the numerical methods used and specify then in Sec. 3.3 the different topologies studied. Some real space properties are presented in Sec. 3.4 before we turn to the characterization of the intramolecular form factor $F(q)$ in Sec. 3.5. While most of this study is dedicated to strictly Gaussian hyperbranched stars, i.e. all excluded volume effects are switched off, we investigate more briefly in Sec. 3.6 by means of Monte Carlo (MC) simulations [20] effects of a weak excluded volume interaction penalizing too large densities. Even an exponentially small

[5] With "multifractal" I merely mean that more than one generator is used.

star type	d_f	G	$N/10^6$	$N_e/10^3$	$\frac{\langle s\rangle}{s_{max}}$	r.f.	R_e	R_g
Dendrimer	∞	17	12.6	197	0.87	0.11	23	22
α-star	6	50	22.6	41.6	0.74	0.19	40	34
α-star	5	80	10.4	10.0	0.70	0.22	51	42
α-star	4	200	7.2	2.2	0.63	0.29	80	64
α-star	3	2000	16.2	0.4	0.47	0.45	253	138
α-star	2.5	2000	2.4	0.05	0.36	0.61	253	108
β-star	3	2048	8.4	1.2	0.49	0.51	256	179
β-star	2.5	4096	1.1	0.03	0.45	0.56	362	171
γ-star	2.5	8192	11.1	0.3	0.47	0.54	512	351

Table 3.1: Various properties for different hyperbranched star types of spacer length $S = 32$: fractal dimension d_f, largest generation number G, total mass N, number of end monomers N_e in the last generation shell $g = G$, rescaled Wiener index $\langle s\rangle/s_{max}$ with $s_{max} = 2GS$ being the largest curvilinear distance between pairs of monomers, relative root mean-square fluctuation $\sqrt{\langle s^2\rangle - \langle s\rangle^2}/\langle s\rangle$ (r.f.) of the normalized histogram $w(s)$, root mean-square end distance R_e between the root monomer and the end monomers of the generation shell $g = G$ and radius of gyration R_g.

excluded volume is seen to change qualitatively the behavior of large regular dendrimers. Neglecting deliberately the long-range correlations expected as for linear chains [1, 23], we sketch in Sec. 3.7 the regime where the Gaussian approximation for melts of hyperbranched stars should remain reasonable for sufficiently large spacers.

3.2 Some computational details

Settings and parameter choice. Let us suppose that the monomers are connected by ideal Gaussian springs. The spring constant is chosen such that the effective bond length b, Eq. 3.1.1, becomes unity. Also, both the temperature T and Boltzmann's constant k_B are set to unity. All Gaussian spacers are of equal length S (which comprises one end monomer or branching monomer). With M being the total number of spacer chains, a chain thus consists of $N = 1 + SM$ monomers. If nothing else is said, $S = 32$ is assumed. (This slightly arbitrary choice is motivated by simulations of dendrimer melts presented elsewhere.) For $S = 32$ we sampled up to a generation number $G = 17$ for regular dendrimers and up to $G \approx 2000$ for power-law hyperbranched stars of fractal dimension $d_f = 3$ and $d_f = 2.5$. (Even larger G obtained using smaller S are included below where appropriate.) Some properties of the largest system computed for each investigated star architecture are listed in Table 3.1.

Local and collective MC moves. Due to their Gaussian chain statistics many conformational properties can be readily obtained using Gaussian propagator techniques [12] or equivalent linear algebra relations [99, 103, 104, 105, 106]. However, some interesting

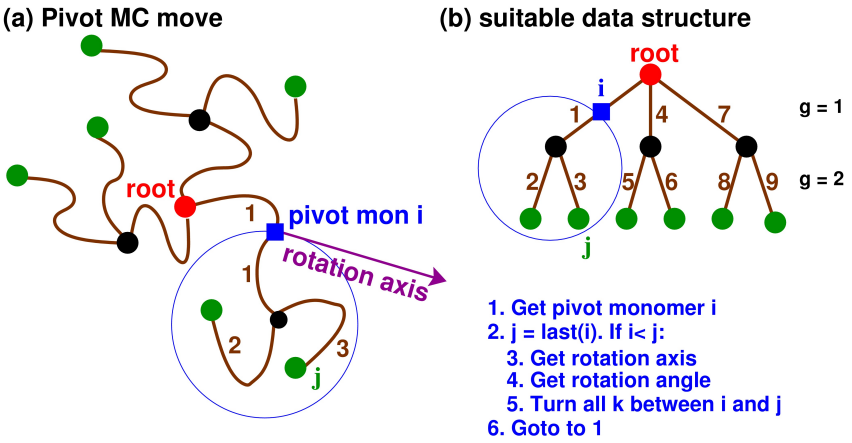

Figure 3.1: Sketch of pivot MC move (a) and data structure (b). A monomer i (filled square) is selected randomly and all attached monomers k closer to the ends (within thin circles) are rigidly turned by an angle θ. A suitable data structure consists in ordering the spacer arms (their index indicated by the numbers) and the monomers such that all monomers k become neighbors in the monomer lists ($i < k \leq j$). The tabulated monomer $j = last(i)$ is the last monomer to be turned.

properties, such as the eigenvalues λ_i of the inertia tensor, can be more easily computed by direct simulation which are in any case necessary if long-range interactions between the monomers are switched on (see below). As shown in Fig. 3.1, we use pivot moves with rigid rotations of the dangling chain end (as shown by the monomers within the thin circles) below a randomly chosen pivot monomer i. The monomers are collectively turned (using a quaternion rotation [20]) by a random angle θ around an also randomly chosen rotation axis through the pivot monomer. As illustrated in panel (b) of Fig. 3.1, it is useful to organize the data structure such that arms and monomers which are turned together are also grouped together. This allows to rotate all monomer k with $i < k \leq j$. The tabulated monomer $j = last(i)$, the last monomer to be turned, must be an end monomer. A pivot move does leave unchanged the distances between connected monomers. (If the connectivity of the monomers is the only interaction, a suggested move is thus always accepted.) To relax the local bond length distribution simple local MC jumps are added [20]. The root monomer at the origin never moves.

Excluded volume interactions. Due to excluded volume constraints the volume fraction occupied by a realistic chain can, obviously, not exceed (much above) unity. One simple way to penalize too large densities is to introduce an excluded volume energy through the lattice Hamiltonian

$$E = \frac{\epsilon}{2} \sum_{\underline{r}} n(\underline{r}) \; (n(\underline{r}) - 1) \tag{3.2.1}$$

using the monomer occupation number $n(\underline{r})$ of a simple cubic lattice. For all examples presented below we set $\delta x = \delta y = \delta z = 1$, i.e. the grid volume $\delta V = \delta x\, \delta y\, \delta z$ is unity and $n(\underline{r}) = \rho(\underline{r})\delta V$ measures the instantaneous local density. The Hamiltonian is similar to the finite excluded volume bond-fluctuation model for polymer melts on the lattice described in [1]. However, the particle positions are now *off-lattice* and only the interactions are described by the lattice. A local monomer or collective pivot move is accepted using the standard Metropolis criterion for MC simulations [20]. Note that the collective pivot moves are best implemented using a second lattice for the attempted moves.

3.3 Characterization of imposed intrachain connectivity

Introduction. We assume that the hyperbranched star topology is not annealed, i.e. not in thermal equilibrium, but irreversibly imposed by an unknown chemical reaction process. The first step for the understanding of such quenched structures is the specification and characterization of the assumed imposed connectivity, often referred to as "connectivity matrix" [99, 106]. A central property characterizing the monomer connectivity is the normalized histogram of curvilinear distances

$$w(s) = \frac{1}{N^2} \sum_{n,m=1}^{N} \delta(s - s_{nm}) \tag{3.3.1}$$

with s_{nm} being the curvilinear distance between the monomers n and m. Trivially, $w(s = 0) = 1/N$ and $w(s) \approx 2N/N^2 = 2/N$ for $0 < s \ll S$ since the same monomer pair is counted twice. Note that the histogram $w(s)$, sampled over all pairs of monomers of the chain, may differ in general from the similar distribution $w_0(s)$ of the curvilinear distances between the root monomer to other monomers. We remind also that for a linear polymer chain [1]

$$w(s) = \frac{2}{s_{\max}} \left(1 - \frac{s}{s_{\max}}\right) \text{ for } 0 < s \leq s_{\max} \tag{3.3.2}$$

with $s_{\max} = N - 1 \approx N$. For most of the star architectures considered the largest curvilinear distance $s_{\max}$ is given by $s_{\max} = 2SG$. The histogram $w(s)$ will be used below for the determination of experimentally relevant properties such as the radius of gyration R_{g} and the intramolecular form factor $F(q)$. The first and second moments of $w(s)$ are given in Table 3.1 for the different architectures studied. We remind that $N\langle s\rangle$ is sometimes called "Wiener index" W_1 [26, 106]. (For linear chains $W_1/N^2 = 1/3$.)

Regular dendrimers. Let us first summarize several simple properties of the regular dendrimers sketched in panel (a) of Fig. 1.1. As already mentioned above, the number

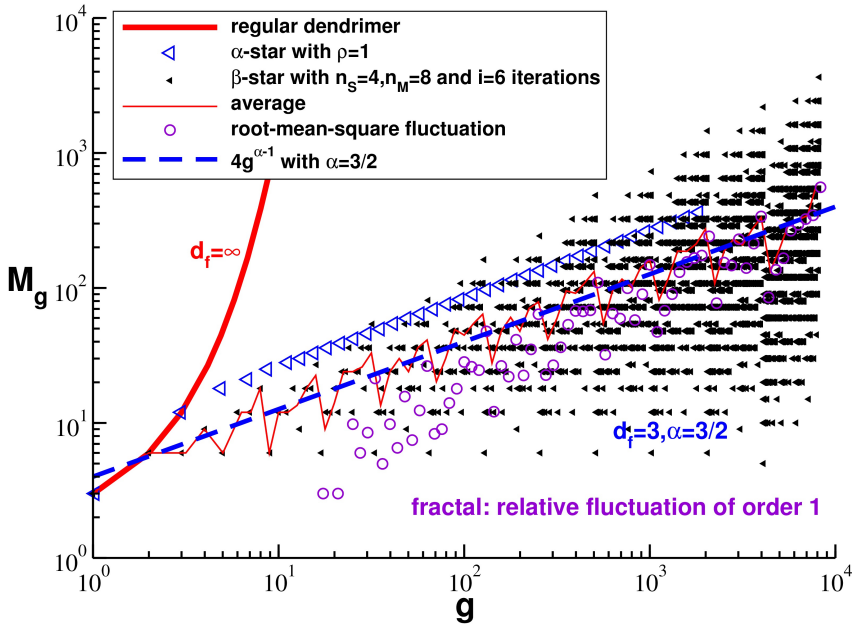

Figure 3.2: Number of spacer chains M_g for regular dendrimers (bold solid line) and hyperbranched power-law stars of fractal dimension $d_f = 3$ ($\alpha = 3/2$). The open triangles refer to an α-star, the small filled triangles to a self-similar fractal constructed using the generator A shown in Fig. 1.1(c). The logarithmically averaged number of arms (thin line) and the root-mean-square fluctuations (circles) are of same order.

M_g of spacer chains per generation shell $g \leq G$ increases exponentially as $M_g = 3\ 2^{g-1}$ as shown by the bold line in Fig. 3.2. Since we assume monodisperse spacer chains of length S, this trivially implies $w_0(s) \approx 2^{s/S}$ for $S \ll s \leq SG$ and that the total mass N at total generation number G must also increase exponentially, as shown in Fig. 3.3. The histogram $w(s)$ of curvilinear distances s for dendrimers is given in panel (a) of Fig. 3.4 (bold solid lines). The main panel gives a linear representation of the dimensionless rescaled histogram $w(s)s_{\max}$ as function of $s/s_{\max}$, the inset on the left-hand side a similar half-logarithmic representation. As one expects, the histogram increases exponentially for curvilinear distances $S \ll s \ll s_{\max}$ due to the exponential increase of alternative paths of length s starting from an arbitrary monomer. Using simple combinatorics it can be seen that the histogram must become

$$w(s) \approx \frac{2}{N}\ 2^{(s/S-1)/2} \text{ for } 1 \leq s \ll s_{\max}. \tag{3.3.3}$$

The cutoff observed for large $s \approx s_{\max}$ is caused, ultimately, by the finite mass of the star and the finite length of its branches, just as the finite length of a linear chain gives rise to Eq. (3.3.2). As seen from Table 3.1, the reduced first moment $\langle s \rangle / s_{\max}$ approaches unity for regular dendrimers and the relative fluctuations are the smallest for all architectures considered.

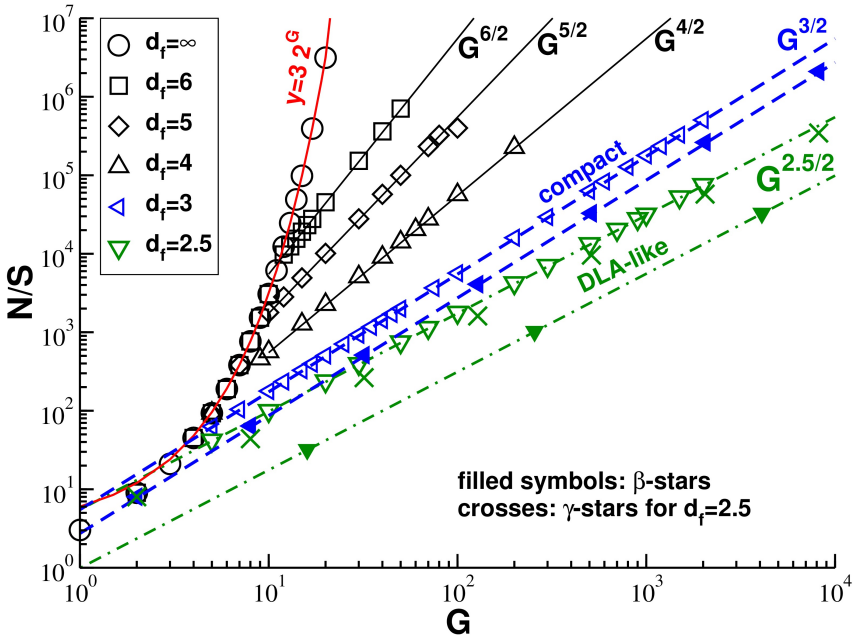

Figure 3.3: Reduced number of monomers N/S *vs.* total generation number G for different imposed topologies and fractal dimensions $d_{\rm f}$. Regular dendrimers are indicated by $d_{\rm f} = \infty$ (circles), α-stars by the other open symbols. The filled triangles corresponds to self-similar fractals of $d_{\rm f} = 3$ ($n_S = 4$, $n_M = 8$) and $d_{\rm f} = 2.5$ ($n_S = 16$, $n_M = 32$) dimensions, the crosses to multifractals of $d_{\rm f} = 2.5$.

Hyperbranched α-stars. As already noted in the Introduction, a simple way to generate stars of a finite fractal dimension $d_{\rm f}$ is to impose a power law $M_g = cg^{\alpha-1}$ for the number of spacers per generation shell with c being a constant.[6] This is done by randomly attaching M_g spacer chains to the end monomers of generation $g-1$ (with the constraint that at most two spacers can be attached per end monomer). An example for such an α-star with $\alpha = 3/2$ is given in Fig. 3.2 (open triangles). The corresponding total mass $N \approx SG^{\alpha}$ as a function of G is shown for $\alpha = 6/2$, $\alpha = 5/2$, $\alpha = 4/2$, $\alpha = 3/2$ and $\alpha = 2.5/2$ by open symbols in Fig. 3.3.[7] The histogram $w_0(s)$ of curvilinear distances from the root monomer increases as $w_0(s) \sim s^{\alpha-1}$ for $S \ll s \leq s_{\rm max}$ as implied by the M_g-scaling (not shown). The curvilinear histograms $w(s)$ over all pairs of monomers are presented in the main panel of Fig. 3.4(a). The histograms are again *non-monotonous* increasing first due to the branching and decreasing finally due to the finite length of the star arms. The latter decay becomes the more marked the weaker the branching, i.e.

[6]The constant c is assumed here to be S-independent. Imposing instead $M_g = \tilde{c}(Sg)^{\alpha-1}$ with $\tilde{c} \sim S^0$ leads to a total mass $N \approx (SG)^{\alpha}$ and, hence, to a typical density $\rho \approx N/R^d \approx (SG)^{\alpha-d\nu}$. The latter choice may, e.g., be useful to compare marginally compact α-stars at constant density for different spacer lengths.

[7]Hyperbranched stars or trees with fractal dimension $d_{\rm f} = 4$ have been discussed in the context of randomly branched polymers (often called "lattice animals") [93], dilute rings in a gel of topological obstacles [96] and as a possible model describing the topological interactions of unconcatenated melts of rings [96, 66]. All these models have in common that on the local scale the branched structure is described by Gaussian spacer chains. A fractal dimension $d_{\rm f} = 6$ would arise if a marginally compact star is constructed assuming *rigid* spacer chains which are then allowed to become flexible.

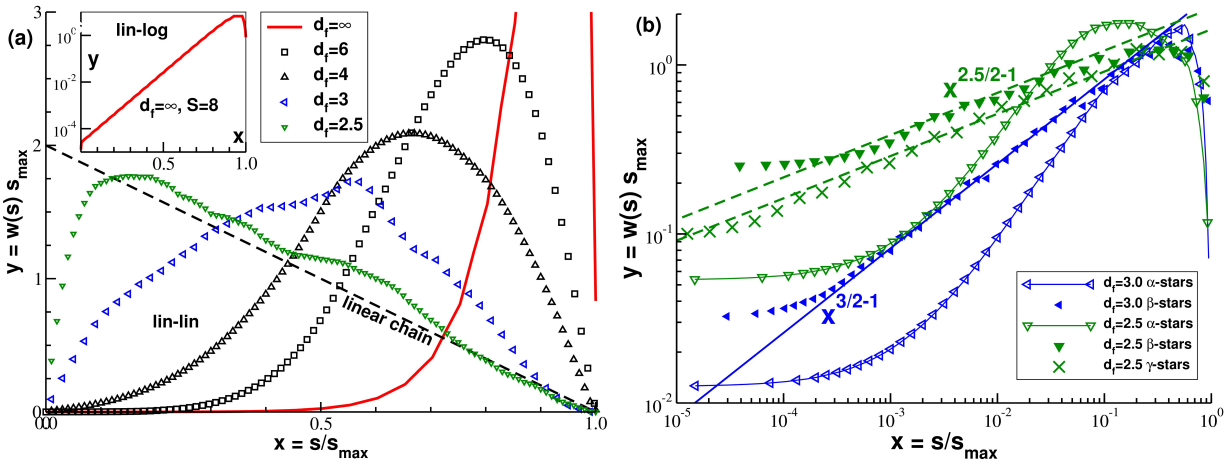

Figure 3.4: Connectivity histogram $w(s)$ measuring the number of monomer pairs at curvilinear distance s along the branched chain: **(a)** Regular dendrimers for $G = 20$ (bold line) and α-stars for different fractal dimensions (open symbols). The dashed line indicates the histogram for a linear chain of length $N \approx s_{\max}$. Inset: Half-logarithmic representation for regular dendrimers. **(b)** Double logarithmic representation for $d_f = 2.5$ (upper data) and $d_f = 3$ (lower data). As emphasized by the solid and dashed lines a power law $x^{\alpha-1}$ is observed for self-similar (multi)fractals chains.

the smaller α, getting similar for the smallest exponent $\alpha = 2.5/2$ studied to the linear chain behavior, Eq. 3.3.2, indicated by the dashed line. As may be better seen from the double-logarithmic representation chosen in panel (b) of Fig. 3.4, this class of stars *cannot* be described by a simple power law or exponential behavior for $w(s)$.[8]

Self-similar β-stars. This is different for self-similar fractals created starting from a $G = 2$ dendrimer of spacer length S_0 (as specified below) as initiator and iterating a generator as the one shown in Fig. 1.1(c). At every iteration step i a spacer of length S_{i-1} is replaced by n_M spacers of length $S_i = S_{i-1}/n_S$. Hence, $S_i = S_0/n_S^i$, $M_i = 9n_M^i$, $N_i - 1 = S_i M_i = 9S_0(n_M/n_S)^i$ and $G_i = 2n_S^i$ for, respectively, the spacer length, the number of spacers, the total mass and the generation number of the star. Importantly, the arms added laterally to the original spacer can always be distributed such that the root-mean square end-to-end distance of the original spacer (filled circles) still characterizes the typical size of the replaced spacer. Since $S_i G_i = 2S_0$ for the curvilinear distance between the root monomer and the end monomers in the largest generation shell $g = G_i$, the typical chain size R, thus remains *by construction* constant as we shall explicitly verify in Sec. 3.4. Note that the spacer length S_i of the final iteration step is set by

$$S \stackrel{!}{=} S_i = S_0/n_S^i, \tag{3.3.4}$$

[8]Note that with decreasing α the first moment $\langle s \rangle$ of α-stars decreases while the relative fluctuations increase (Table 3.1).

which fixes the mass $N_0 \approx S_0 \approx S n_S^i$ of the initiator star. Using $N_i \sim R^{d_\mathrm{f}} \sim N_0^{\nu d_\mathrm{f}}$ this implies

$$n_M = n_S^\beta \text{ with } \beta = d_\mathrm{f}\nu \tag{3.3.5}$$

relating thus both numerical constants n_S and n_M. As shown for $d_\mathrm{f} = 3$ ($n_S = 2^2$, $n_M = 2^3$) by the small filled triangles in Fig. 3.2, such a self-similar construction leads to a strongly fluctuating number M_g of spacers. However, as shown by the thin solid line the (logarithmically) averaged number of arms still increases as $M_g \sim g^{\alpha-1}$ with $\alpha = \beta = d_\mathrm{f}\nu$ in agreement with Eq. (3.1.4). Interestingly, the corresponding (also logarithmically averaged) root-mean square fluctuations (as indicated by open circles) are of the same order, i.e. the relative fluctuations of spacer number M_g per generation shell are of order one. The important point is here that all monomers are *statistically equivalent* and that the root monomer does not play any specific role which would break the self-similarity. (As we have verified, this implies $w(s) \approx w_0(s)$.) Averaging over all spacer chains, the total mass N scales, as expected, again as $N \approx SG^\alpha$ with $\alpha = d_\mathrm{f}\nu$ as shown in Fig. 3.3 by filled triangles for $d_\mathrm{f} = 3$ and $d_\mathrm{f} = 2.5$. The latter architecture, constructed using $n_S = 2^4$ and $n_M = 2^5$, is motivated by the fractal dimension $d_\mathrm{f} \approx 2.5$ which may characterize self-similar stars generated by DLA in $d = 3$ dimensions [67, 68, 69]. In our view this is one interesting universal limit of (at least conceptional) experimental relevance [70]. Being self-similar all monomers are equivalent and since the number of monomers at a curvilinear distance s must increase on average as $(s/S)^{\alpha-1}$, one expects for $S \ll s \ll s_\mathrm{max}$ the power-law scaling

$$w(s) \approx N \times \frac{1}{N^2}(s/S)^{\alpha-1} \approx \frac{1}{s_\mathrm{max}}(s/s_\mathrm{max})^{\alpha-1} \tag{3.3.6}$$

with $N \approx S(s_\mathrm{max}/S)^\alpha \approx SG^\alpha$. This is confirmed by the histograms (filled symbols) shown in Fig. 3.4(b).

Stochastic two-generator multifractals. Since the DLA limit is of some importance we have sampled a second system class of fractal dimension $d_\mathrm{f} = 2.5$ constructed by mixing the generator A for marginally compact stars shown in panel (c) of Fig. 1.1 with the second generator B shown in panel (d). Being constructed using more than one generator these so-called "γ-stars" are in fact multifractals [69, 68]. (We remember that DLA clusters are also multifractal [68]. No multifractal analysis [69] is required here, however.) For a given spacer we apply the generator A with a probability f_A and the generator B with a probability $f_B = 1 - f_A$. By choosing different values of f_A any fractal dimension between $d_\mathrm{f} = 2$ and $d_\mathrm{f} = 3$ can be sampled using both generators. By reworking the arguments leading to Eq. (3.3.5) it can be readily seen that choosing $f_A = f_B = 1/2$ corresponds to $d_\mathrm{f} = 2.5$. While the fractal stars are deterministic, the multifractals have a *stochastic* topology due to the random mixing of both generators and an ensemble average over

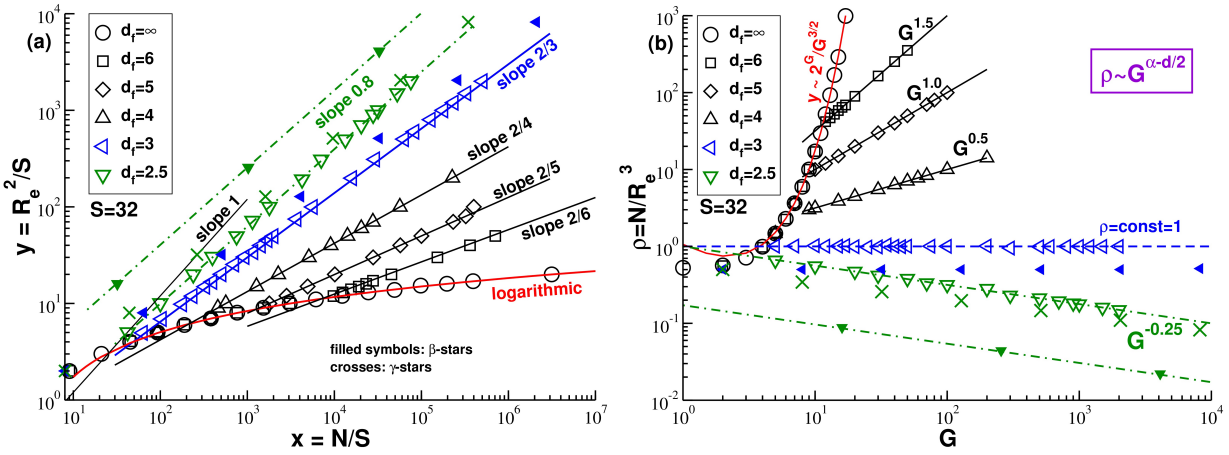

Figure 3.5: Core-to-end distance R_e for different imposed topologies: **(a)** Double-logarithmic representation of the reduced mean-squared end distance R_e^2/S *vs.* reduced mass N/S. **(b)** Density $\rho \equiv N/R_e^3$ *vs.* total generation number G for a spacer length $S = 32$.

several independent chains is thus taken. As may be seen from the crosses in Fig. 3.3 and Fig. 3.4(b), the properties of β- and γ-stars are, however, rather similar.

3.4 Real space characterization

End distance R_e. There are several ways to characterize the typical star size R all being equivalent from the scaling point of view. A double-logarithmic representation of the reduced mean-square end distance R_e^2/S *vs.* the reduced mass N/S is presented in panel (a) of Fig. 3.5. Note that the values of R_e obtained by direct MC simulations are within statistical accuracy identical to $R_e^2 = b^2SG$. Both data sets are lumped together. The regular dendrimer size increases, of course, logarithmically with the mass (circles and bold solid line). The power-law slopes indicated for finite-d_f systems are consistent with the definition $N \sim R^{d_f}$. As one measure of the overall density of a star one may define $\rho \equiv N/R_e^d$. (Obviously, a suitable order-one geometrical factor, such as $4\pi/3$, might be included in this definition.) As can be seen from panel (b) of Fig. 3.5, the density for regular dendrimers exceeds already at $G = 10$ an unrealistic order of 10 monomers per volume element. As indicated by the various power-law slopes, $\rho \sim G^{\alpha - d\nu}$ for hyperbranched power-law stars of finite fractal dimension, i.e. the overall density increases for $d_f > d$ and decreases for $d_f < d$ as it should.

Radius of gyration R_g. The radius of gyration R_g presented in Fig. 3.6 has been determined with identical results (lumped again together) either from the MC sampled

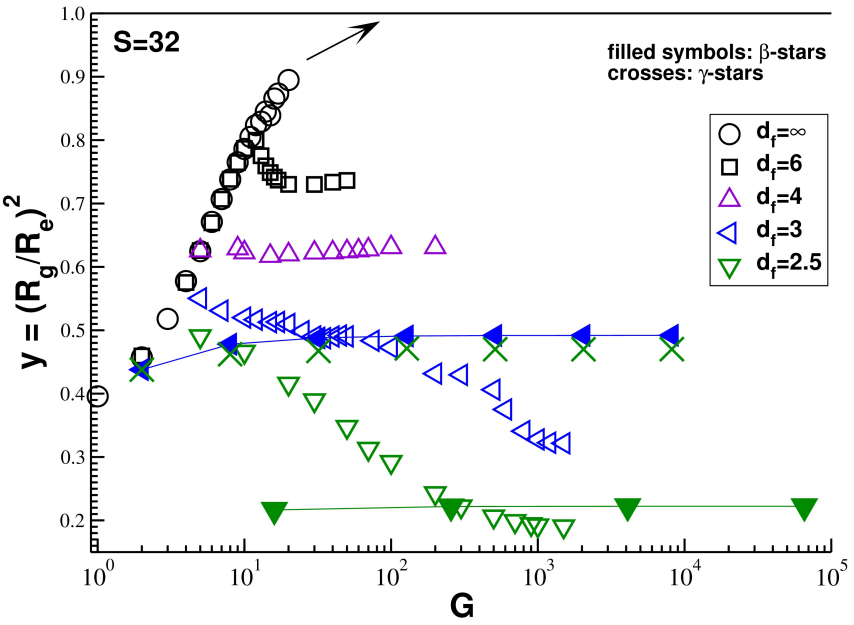

Figure 3.6: Reduced radius of gyration $y = (R_g/R_e)^2$ *vs.* generation number G. The ratio y becomes constant only for self-similar fractals (filled symbols) and multifractals (crosses).

configuration ensembles or by means the formula [13]

$$R_g^2 \equiv \frac{1}{2N^2} \sum_{n,m=1}^{N} \left\langle (\underline{r}_n - \underline{r}_m)^2 \right\rangle = \frac{1}{2} \sum_{s}^{s_{max}} w(s) R_s^2 \tag{3.4.1}$$

using the histogram of curvilinear distances $w(s)$ discussed above and the Gaussian chain property $R_s^2 = b^2 s$. Measuring thus the first moment of $w(s)$, the radius of gyration is equivalent for Gaussian chains to the Wiener index W_1. The reduced radius of gyration $y = (R_g/R_e)^2$ is plotted as a function of G. Since the end monomers dominate the mass distribution of regular dendrimers for large G, R_g becomes similar to R_e. As expected, y approaches unity from below (circles). Interestingly, the ratio y is constant for the self-similar β- and γ-stars, i.e. R_e and R_g are similarly rescaled by the iterative application of the generators. This confirms the choice of generators discussed in Sec. 3.3. We note finally that other observables characterizing the star size R, such as the hydrodynamic radius [13], have been found to scale similarly as the end distance R_e and the radius of gyration R_g.

Density profiles. Figure 3.7 presents various normalized density profiles $p(r)$ with r being the radial distance from the focal molecule point. The rescaled distribution $y = p(r)R^d$ is plotted as a function of the reduced distance $x = r/R$ with $R = R_e$ in panel (a) and $R = R_g$ in panel (b) and panel (c). The distribution of the end monomers for regular dendrimers ($G = 12$, $S = 32$) shown in panel (a) is a reminder of Eq. (3.1.2), i.e.

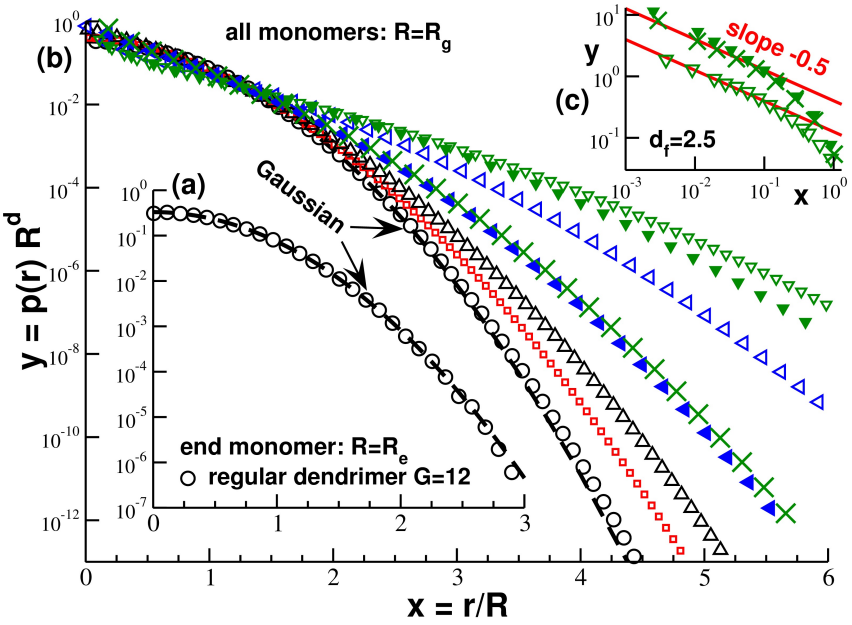

Figure 3.7: Spherically averaged density distributions $y = p(r)R^d$ with r/R being the reduced distance from the cebntral monomer: **(a)** End monomer distribution with $R = R_e$ showing the expected Gaussianity (dashed line), **(b)** total monomer density distribution rescaled with $R = R_g$ using the same symbols as in Fig. 3.6, **(c)** double-logarithmic representation for three architectures with $d_f = 2.5$. The power-law slope indicates the expected exponent $d_f - d = -0.5$.

of the trivial fact that the distances of *all* pairs of monomers have a Gaussian distribution (dashed line). The rescaled density $\rho(r) = p(r)N$ of all monomers is shown in panel (b) of Fig. 3.7 (using a half-logarithmic representation) for the largest star of each topology class. Note that the distribution $p(r)$ has been either obtained for masses up to $N \approx 10^6$ from our MC simulations or for larger systems using

$$p(r) = \sum_{s=0}^{s_{\max}} w_0(s) P(r,s) \tag{3.4.2}$$

with $w_0(s)$ being the already mentioned normalized histogram of monomers of same curvilinear distance from the central monomer and $P(r,s)$ the size distribution of a subchain of arc-length s given by Eq. (3.1.2). Since the density distribution of large regular dendrimers (circles) is dominated by the end monomers, $p(r)$ becomes essentially Gaussian (dashed line). We shall come back to this point at the end of Sec. 3.5. The histograms get naturally broader with decreasing d_f. Panel (c) on the right-hand side gives a double-logarithmic representation of the total monomer density distribution for three topologies with $d_f = 2.5$. As explained in de Gennes' book [12], the density should decrease as $n(r)/r^d \sim 1/r^{d-d_f}$ with $n(r) \sim r^{d_f}$ being the mass distributed within the volume r^d. The same power-law exponent is obtained using $w_0(s) \sim s^{\alpha-1}$ and integrating Eq. (3.4.2) for $d_f < d$ and $x \ll 1$. Even the not self-similar α-star (open triangles) is seen to follow the

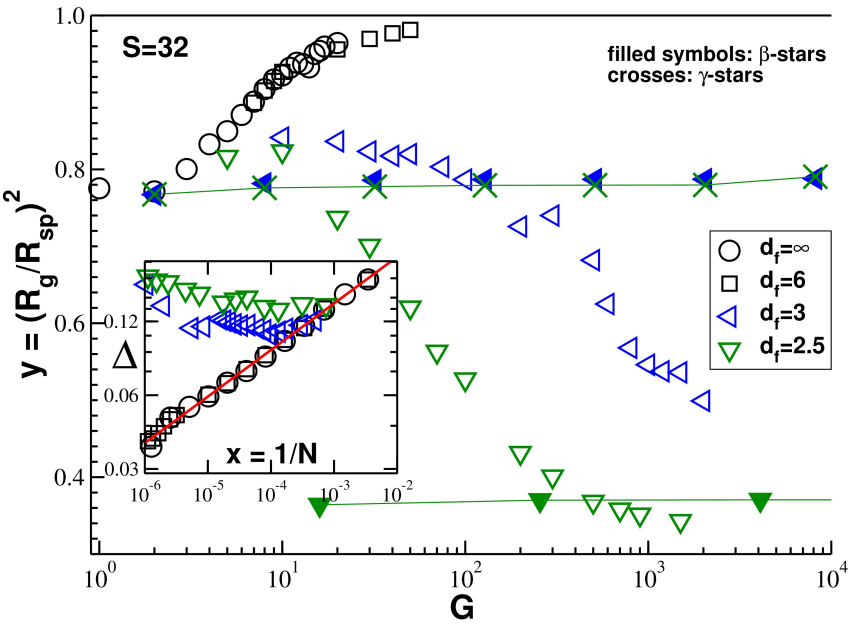

Figure 3.8: Aspherical fluctuations: ratio $(R_g/R_{sp})^2$ (main panel) and rescaled largest eigenvalue $\Delta \equiv \langle\lambda_1\rangle / R_g^2 - 1/3$ of the inertia tensor for regular dendrimers and α-stars (inset).

predicted slope (solid lines). It is sufficient for this property that $w_0(s)$ has a power-law asymptotics albeit $w(s)$ has not.

Center of mass fluctuations. Albeit spherically averaged density profiles may reasonably characterize *some* aspects of the conformational properties of our hyperbranched polymer stars [73] it is important to emphasize that a given instantaneous configuration may *not* be spherically symmetric and depending on the property probed experimentally or in a computer experiment these aspherical fluctuations may crucially matter. This issue is addressed in Fig. 3.8. The main panel compares the true radius of gyration $R_g^2 = \frac{1}{N}\sum_n \langle(\underline{r}_n - \underline{r}_{cm})^2\rangle$ with a spherical approximation of the mass distribution defined by $R_{sp}^2 \equiv \frac{1}{N}\sum_n \langle \underline{r}_n^2\rangle$ assuming the center of mass $\underline{r}_{cm}$ of the star to be set by the the central monomer at the origin for all configurations, i.e. $\underline{r}_{cm} \stackrel{!}{=} 0$. The main panel of Fig. 3.8 presents $(R_g/R_{sp})^2$ as a function of the generation number G for different topologies. The ratio is always smaller than unity. The ratio is seen to approach unity from below for regular dendrimers and α-stars with $d_f > d$. While the spherical approximation $\underline{r}_{cm} = 0$ becomes thus better with increasing size, stars with an incredible huge molecular mass are required to reach $R_g \approx R_{sp}$. Interestingly, the ratio actually *decreases* for α-stars with $d_f = 3$ and $d_f = 2.5$ (open triangles) while it is essentially constant for self-similar (multi)fractals (filled triangles and crosses). For these experimentally most relevant star classes the center-of-mass fluctuations remain thus relevant even in the asymptotic chain size limit.

Asphericity. The asphericity of the stars may be (also) characterized by computing the three eigenvalues $\lambda_1 \geq \lambda_2 \geq \lambda_3$ of the inertia tensor of each star and averaging over the ensemble. Since $R_g^2 = \langle\lambda_1\rangle + \langle\lambda_2\rangle + \langle\lambda_3\rangle$, the rescaled eigenvalue $\Delta \equiv \langle\lambda_1\rangle / R_g^2 - 1/3$ should vanish for perfectly spherical chains with $\langle\lambda_1\rangle = \langle\lambda_2\rangle = \langle\lambda_3\rangle$. We have plotted Δ as a function of the inverse mass for several topologies in the inset of Fig. 3.8. As expected from the consideration of R_{sp}, Δ is seen to vanish in the large-N limit for regular dendrimers and α-stars with $d_f > d$. (As shown by the solid line, Δ decays only *logarithmically* with mass.) The opposite behavior is found for smaller fractal dimensions as shown by the open triangles. Whether for these systems Δ becomes constant for $N \to \infty$ (as for linear chains) cannot be confirmed from our numerical data. The crossover to this likely plateau seems to be sluggish.

3.5 Form factor

Introduction. Conformational properties of branched and hyperbranched star polymers can be determined experimentally by means of light, small angle X-ray or neutron scattering experiments [113, 114]. Using appropriate labeling techniques this allows to extract the coherent intramolecular form factor $F(q)$ defined as

$$NF(q) = \left\langle \hat{\rho}(\underline{q})\hat{\rho}(-\underline{q}) \right\rangle = \left\langle || \sum_{n=1}^{N} \exp\left(\mathrm{i}\underline{q} \cdot \underline{r}_n\right) ||^2 \right\rangle \tag{3.5.1}$$

with $\hat{\rho}(\underline{q})$ being the Fourier transform of the instantaneous density and $\underline{q}$ the wavevector. The average $\langle \ldots \rangle$ is sampled over the ensemble of thermalized chains. The form factor is of interest since it allows to compare real experiments with theoretical predictions and numerical data [12]. For sufficiently large N and small $q \equiv ||\underline{q}||$ the radius of gyration R_g, as one possible measure of the star size, becomes the only relevant length scale. The form factor thus scales as [12]

$$F(q) = Nf(Q) \text{ with } Q = qR_g \tag{3.5.2}$$

being the reduced wavevector and $f(Q)$ a universal scaling function with $f(Q) = 1 - Q^2/d$ in the "Guinier regime" for $Q \ll 1$. In the opposite large-q limit the density fluctuations within the spacer chains are measured and the form factor becomes [13]

$$F(q) = \frac{12}{(bq)^2} \text{ for } \frac{1}{bS^{1/2}} \ll q \ll \frac{1}{b}. \tag{3.5.3}$$

For even larger wavevectors correlations on the monomer scale are probed. In the following we shall focus on the intermediate wavevector range $1/R_g \leq q \ll 1/bS^{1/2}$ between the Guinier regime and the trivial large-q limit.

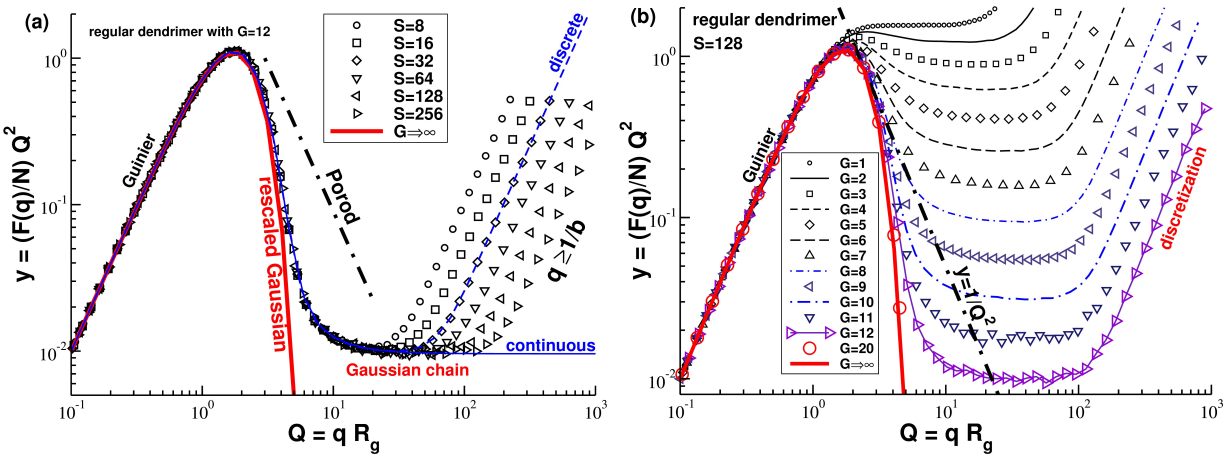

Figure 3.9: Kratky representation of the form factor $y = (F(q)/N)Q^2$ as a function of the reduced wavevector $Q = qR_g$ for regular dendrimers: **(a)** $G = 12$ for different spacer length S, **(b)** $S = 128$ for different generation number G.

Regular dendrimers. Focusing on regular dendrimers Fig. 3.9 presents a Kratky representation [15] of the form factor $y \equiv (F(q)/N)Q^2$ as a function of the reduced wavevector $Q = qR_g$. Panel (a) shows stars of different spacer length S for a generation number $G = 12$, panel (b) different generation numbers G for a fixed spacer length $S = 128$. The increase of the rescaled data for very large wavevectors $q \gg 1/b$ observed in both panels is trivially caused by the discrete monomeric units used in our simulations (see below). The scaling observed for different S in panel (a) for the intermediate wavevector regime, where the Gaussian spacer chains are probed, is due to the fact both the mass N and the radius of gyration R_g^2 are linear in S. The corresponding failure of Eq. (3.5.2) in panel (b) shows that there is more than one characteristic length scale. Note that the strong decay after the Guinier regime above $Q \approx 3$ becomes systematically sharper with increasing generation number G. The bold solid lines in both panels indicate the expected asymptotic limit for $G \to \infty$ as discussed at the end of this section. Note that the regular dendrimer with $G = 20$ (large circles) shown in panel (b) is rather close to this limit. The form factor of this huge chain has not been obtained by MC simulations but by computing numerically the equivalent discrete sum

$$F(q) = \sum_{s=0}^{s_{\max}} w(s) P(q,s) \tag{3.5.4}$$

with $w(s)$ being the curvilinear segment histogram discussed above and $P(q,s)$ the Fourier transform of the segment size distribution $P(r,s)$. Since $P(q,s) = \exp(-(aq)^2 s)$ with $a \equiv b/\sqrt{2d}$ for Gaussian chains, the form factor is readily computed yielding, as one expects, the same results as obtained from the explicitly computed configuration ensembles. This can be seen from the dashed line in panel (a) of Fig. 3.9 for a spacer length $S = 32$. To compute numerically the form factor using $w(s)$ has the advantage that the already

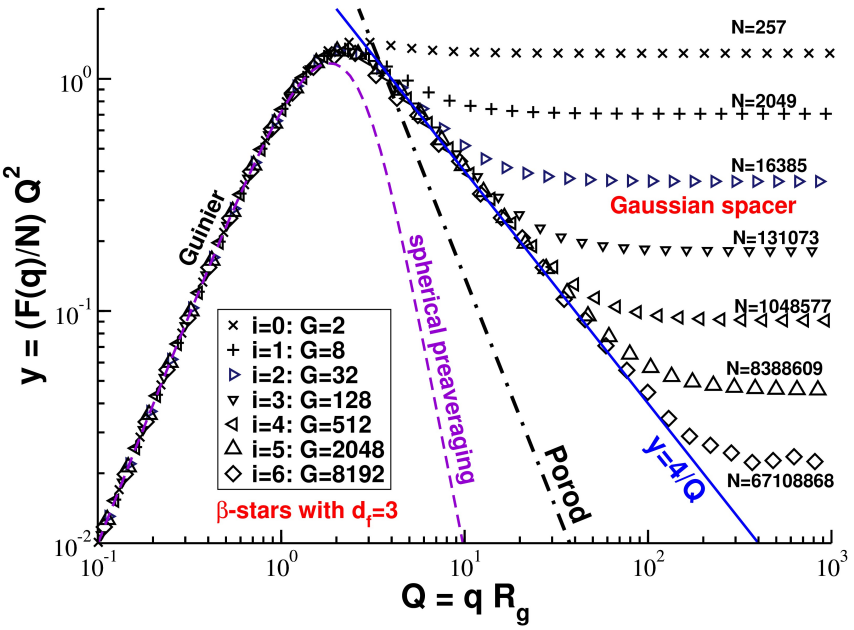

Figure 3.10: Kratky representation for β-stars with $d_\mathrm{f} = 3$. The reduced form factor approaches with increasing G the power-law slope -1 (bold line). The total monomer mass N is indicated for each iteration i. The dashed line has been obtained according to Eq. (3.5.5) by Fourier transformation of the spherically averaged density $\rho(r)$ for $i = 6$.

mentioned discretization effect at $q \gg 1/b$ can be eliminated. To do this the discrete sum Eq. (3.5.4) is replaced by a continuous integral for $s > 0$ and the $s = 0$-contribution to the form factor is added. As shown by the thin solid line in panel (a), this allows to get rid of the irrelevant discretization effect.

Marginally compact stars. Figure 3.10 presents the form factor obtained using the continuous version of Eq. (3.5.4) for self-similar fractals of marginal compactness ($d_\mathrm{f} = 3$). As one expects according to Eq. (3.1.5), the data approach with increasing generation number the power-law slope $2-d_\mathrm{f} = -1$ (bold line) expected for the intermediate wavevector regime. We remind that Eq. (3.1.5) can be derived from Eq. (3.5.4) and the scaling $w(s) \sim s^{\alpha-1}$ for self-similar fractals. Interestingly, Eq. (3.1.5) does *not* hold for the (not self-similar) α-stars as may be seen from Fig. 3.11. Note also that the large-q plateau of the rescaled form factor in Fig. 3.10 only decays as $R_\mathrm{g}^2/N \sim 1/N^{1/3}$ extremely slowly with mass. This makes the numerical confirmation of the power-law slope demanding. For real experiments this implies that the determination of a fractal dimension $d_\mathrm{f} \approx 3$ using the power-law scaling of the form factor for self-similar stars will also be challenging. We remind that a similar slow convergence of the intermediate wavevector regime is well-known for other more-or-less compact polymers such as polymers confined to ultra thin slits or melts of polymer rings [66, 115].

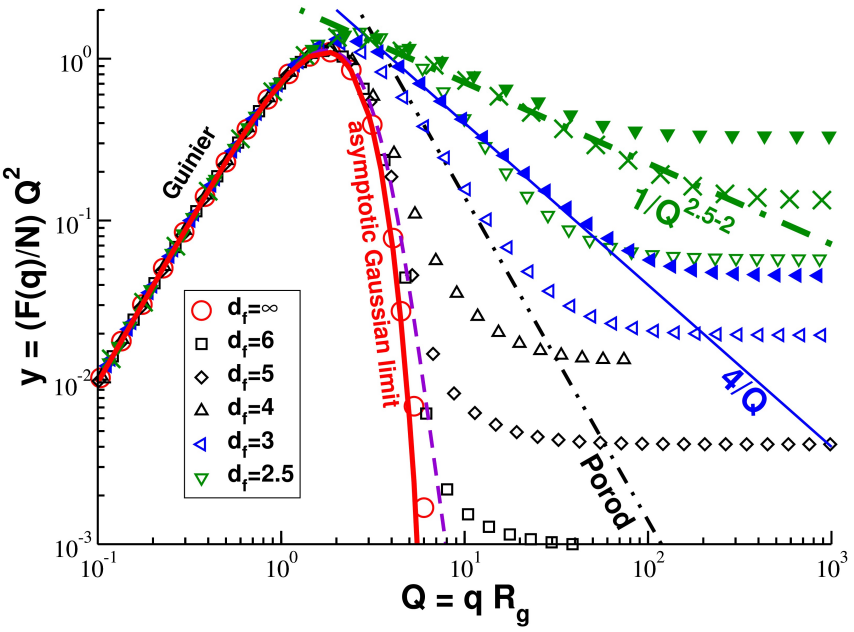

Figure 3.11: Rescaled form factor $y(Q) = (F(q)/N)Q^2$ for the largest stars available obtained using Eq. (3.5.4). The self-similar β- and γ-stars decay with a power law Q^{2-d_f} in the intermediate wavevector regime as shown by the thin solid line for $d_f = 3$ ($i = 6$) and by the dash-dotted line for $d_f = 2.5$. The dashed line indicates the preaverage approximation using Eq. (3.5.5) for α-stars of $d_f = 5$, the bold solid line the expected large-dendrimer limit.

Comparison of different architectures. The rescaled form factors for the largest chains considered for each studied topology are compared in Fig. 3.11. As expected, all data sets collapse in the Guinier regime below $Q \approx 2$ and become again constant for large wavevectors $q \gg 1/bS^{1/2}$. (The discretization effect for large q is again avoided using the continuous version of Eq. (3.5.4).) The decay of the reduced form factor in the intermediate wavevector is seen to become systematically stronger with increasing fractal dimension d_f. For the self-similar (multi)fractals this decay is described by Eq. (3.1.5) as emphasized by the solid and the dash-dotted power-law slopes for, respectively, $d_f = 3$ and $d_f = 2.5$. All other architectures decay stronger than a power law. Note that it is the shape of this decay which is the most central property to be tested experimentally to characterize, at least approximatively, the structure of hyperbranched stars.

Spherical preaveraging. As reminded at the beginning of this section, the intramolecular form factor is the ensemble average of the squared Fourier transform $\hat{\rho}(\underline{q})$ of the fluctuating instantaneous monomer density. Following the recent work by Likos *et al.* [51], this begs the question of whether in the limit of large and dense stars, where density fluctuations should become sufficiently small, one may replace $\hat{\rho}(\underline{q})$ by the Fourier transform $\rho(\underline{q})$ of the averaged density profile $\rho(\underline{r})$ discussed in Sec. 3.4. Due to the spherical

symmetry of our stars this suggests using Eq. (6.54) of Ref. [15] the approximation

$$F(q) \approx N \left(\int \mathrm{d}\underline{r}\; p(r)\; \frac{\sin(\underline{q}\cdot\underline{r})}{\underline{q}\cdot\underline{r}} \right)^2 \tag{3.5.5}$$

with $p(r) = \rho(r)/N$ being known from Eq. (3.4.2). As seen in Fig. 3.10 for marginally compact fractals, Eq. (3.5.5) is not useful for open ($d_\mathrm{f} < d$) and marginally open ($d_\mathrm{f} \approx d$) architectures for which the density fluctuations are yet too large. (The large-q density fluctuations within the spacer chains and on the scale of the monomers are integrated out by the preaveraging approximation and can thus in any case not be seen.) The approximation becomes systematically more successful, however, with increasing fractal dimension as seen in Fig. 3.11 for α-stars of fractal dimension $d_\mathrm{f} = 5$. Note that the striking decay of the rescaled form factor above the Guinier regime is accurately described by the approximation. As we have seen in Fig. 3.7, the distribution $p(r)$ becomes systematically more Gaussian with increasing star size and fractal dimension since the end monomers of the largest generation shell dominate the total density. Since the Fourier transform of a Gaussian is again a Gaussian, this implies

$$F(q) \approx N \exp\left(-(qR_\mathrm{g})^2/d\right) \text{ for } q \ll 1/bS^{1/2}. \tag{3.5.6}$$

As seen by comparing the solid bold lines in Fig. 3.9 and Fig. 3.11 with the form factors computed using Eq. (3.5.4) for our largest dendrimers (circles), the asymptotic behavior Eq. (3.5.6) gives an excellent fit to our numerical data.

3.6 Weak excluded volume effects

Introduction. Up to now we have only considered effects of the imposed monomer connectivity (topology) assuming all other interactions (persistence length, excluded volume, ...) to be switched off ($\epsilon = 0$). Since essentially all properties (apart the eigenvalues λ_i of the inertia tensor) can be obtained analytically or numerically using the Gaussian chain statistics, the presented MC simulations were less crucial. Direct simulations are, however, essential for testing the influence of (albeit weak) excluded volume interactions computed using the lattice occupation number Hamiltonian, Eq. (3.2.1), described at the end of Sec. 3.2.

Scaling of chain sizes. Figure 3.12 presents the excluded volume dependence of the radius of gyration R_g for regular dendrimers of four different generation numbers G. (Similar behavior is found for other characterizations of the typical chain size R.) As revealed in the main panel, the excluded volume effects are the more marked the larger the mass $N(G)$: The radius of gyration increases already at $\epsilon = 10^{-4}$ for $G = 12$ while it

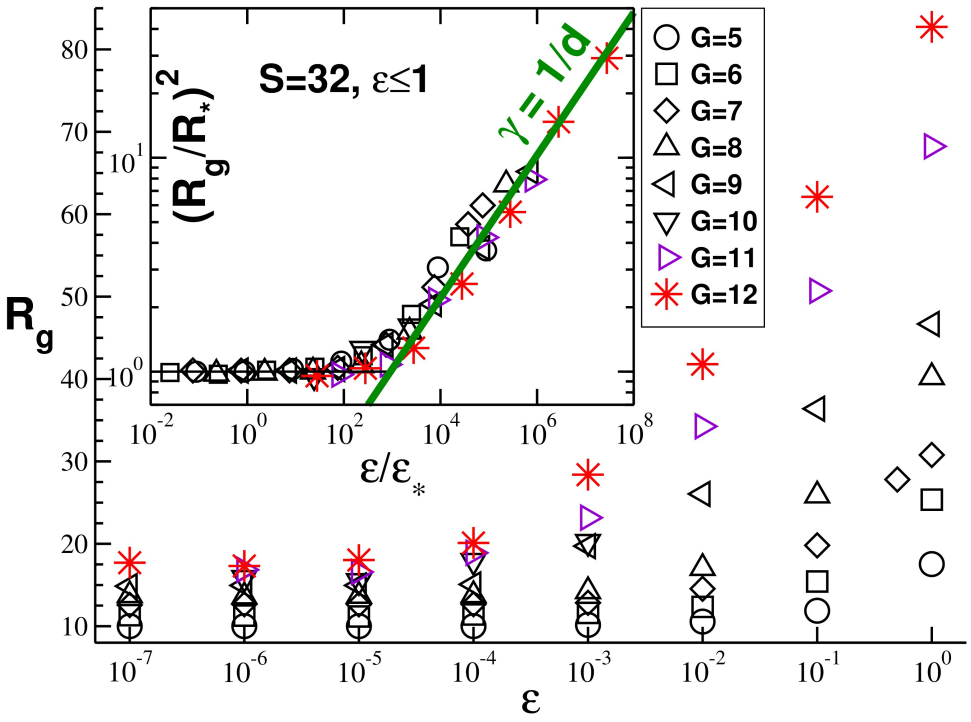

Figure 3.12: Radius of gyration R_g for dendrimers of generation number G as indicated *vs.* excluded volume energy ϵ. Main panel: Unscaled raw data for $S = 32$. Inset: Rescaled radius of gyration $(R_g/R_\star)^2$ as a function of $\epsilon/\epsilon_\star$ with $R_\star \approx (SG)^\nu$ and $\epsilon_\star \approx k_B T R_\star^d/N^2$. The bold slope corresponds (approximately) to the compact limit $N \sim R_g^d$.

has barely changed at $\epsilon = 0.1$ for $G = 5$. A successful data collapse is seen in the inset of Fig. 3.12 where the rescaled radius of gyration $(R_g/R_\star)^2$ is plotted as a function of the reduced interaction energy $\epsilon/\epsilon_\star$ with $R_\star \equiv R_g(\epsilon = 0) \approx (SG)^\nu$ being the typical size of the Gaussian dendrimer star and $\epsilon_\star \approx k_B T\ R_\star^d/N^2$ the characteristic energy scale below which the star remains Gaussian.

Fixman's criterion. This scaling is a direct consequence of Fixman's general criterion [13, 14]

$$1 \gg v\rho^2 R_\star^d \approx vN^2/R_\star^d \tag{3.6.1}$$

for the Gaussian chain approximation with $v \approx \beta\epsilon\delta V$ being the excluded volume, β the inverse temperature and $\rho \approx N/R_\star^d$ the overall density for Gaussian stars. As stressed by the horizontal asymptote indicated in the inset, this is confirmed by the data for small $\epsilon/\epsilon_\star$. The power-law slope $\gamma = 1/d$ (bold line) for large reduced interaction energies is only an *approximative* guide to the eye not taking into account logarithmic corrections. This can be seen *(i)* from the usual power-law scaling ansatz [12] $R_g^2 \approx R_\star^2\,(\epsilon/\epsilon_\star)^\gamma$, *(ii)* neglecting the weak logarithmic N-dependence of $R_\star$ (Fig. 3.5) and *(iii)* assuming that the dendrimers become essentially marginally compact, $N \sim R_g^d$, for large ϵ. The latter point has explicitly been checked. For stars with finite fractal dimension d_f a similar scaling behavior has been found (not shown). In terms of the generation number G and the spacer

length S, Fixman's criterion may be rewritten remembering that $N \approx S\ 2^G$ for regular dendrimers and $N \approx S\ G^{d_f \nu}$ for power-law stars. Hence, the Gaussian approximation must hold for $S \ll S_\star$ with an *upper* critical spacer length $S_\star$ scaling as

$$\begin{aligned} S_\star &\approx 1/\left(\beta\epsilon\ 2^{2G}/G^{d\nu}\right)^{1/(2-d\nu)} \text{ and} \\ S_\star &\approx 1/\left(\beta\epsilon\ G^{2\alpha-d\nu}\right)^{1/(2-d\nu)}, \end{aligned} \tag{3.6.2}$$

respectively, for dendrimers ($d_f = \infty$) and finite-d_f hyperbranched stars. In both cases $S_\star \sim 1/(\beta\epsilon)^2$ in $d = 3$ dimensions (while four-dimensional stars are only marginally swollen).

3.7 Conclusion

Summary. Following our recently submitted manuscript Ref. [54], we have revisited by means of direct analytical calculation, using for instance Eq. (3.5.4), and straightforward MC simulations (Sec. 3.2) several conformational properties of regular (exponentially growing) dendrimers and power-law hyperbranched stars (Fig. 1.1) assuming Gaussian chain statistics ($\nu = 1/2$). As emphasized, a central imposed property is the normalized weight $w(s)$ of curvilinear distances s between monomer pairs (Fig. 3.4). Focusing on experimentally measurable observables such as the radius of gyration R_g (Fig. 3.6) and the intramolecular form factor $F(q)$ (Figs. 3.9-3.11), we investigated the scaling for asymptotically long stars with different fractal dimensions d_f. Due to their topological simplicity regular dendrimers ($d_f = \infty$) have played a central role in our presentation (Fig. 3.9) as in other recent computational studies [29, 34, 36, 51, 73]. Being in our view experimentally and technically more relevant, we have also focused on stochastic architectures with $d_f = 3$ (marginally compact) and $d_f = 2.5$ as expected for stars created by DLA [69]. We compared "α-stars" constructed by imposing $M_g \sim g^{\alpha-1}$ arms per generation with truly self-similar so-called "β-stars" and "γ-stars" for which M_g becomes a strongly fluctuating quantity (Fig. 3.2). As shown in Fig. 3.11, only the latter two topologies show the power-law decay, Eq. (3.1.5), of the form factor in the intermediate wavevector regime expected for open self-similar systems [12, 66]. While large compact ($d_f > d$) stars may roughly be seen as dense colloidal spheres in agreement with Likos *et al.* [51], the instantaneous aspherical fluctuations can not be neglected for experimentally relevant properties for the smaller fractal dimensions studied (Fig. 3.8, dashed line in Fig. 3.10). We have commented briefly on the effects of gradually switching on an excluded volume potential. Coupling the (off-lattice) monomers by means of a (lattice) MC scheme (Sec. 3.2), we have sketched for different architectures the regimes ($\epsilon \ll \epsilon_\star$, $S \ll S_\star$) where the Gaussian star approximation can be assumed to be reasonable (Fig. 3.12).

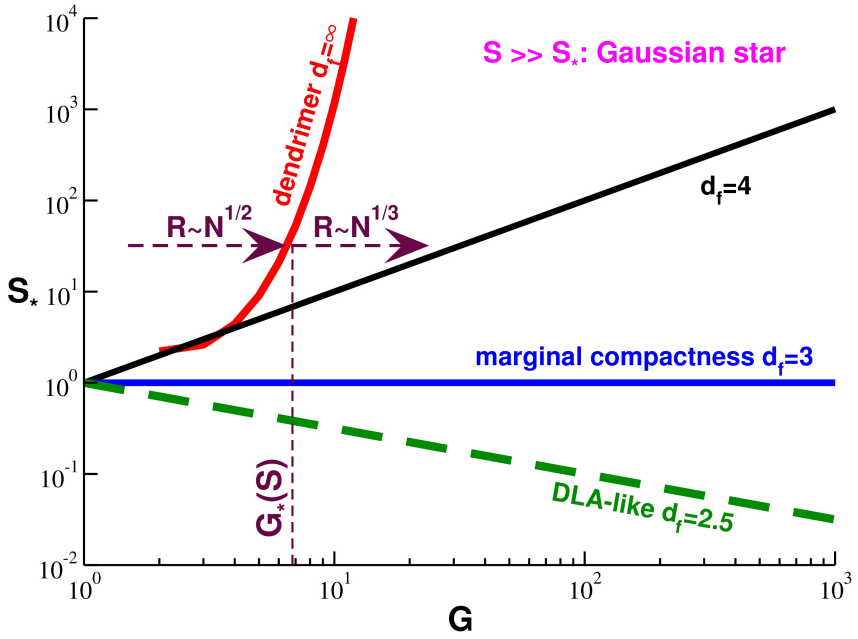

Figure 3.13: Sketch of critical spacer length $S_\star$ for melts for dendrimers ($d_\mathrm{f} = \infty$) and hyperbranched power-law stars with finite d_f as indicated. The Gaussian star assumption holds above the bold lines. Note that the scaling argument does not allow to fix the scale of the vertical axis. If the generation number G is increased at constant spacer length S, as indicated by the dashed arrows, ideal chain behavior is expected for small $G \ll G_\star(S)$, while the star becomes colloid-like for larger $G \gg G_\star(S)$. The number of chains interacting with a reference star should have a maximum at $\approx G_\star(S)$.

Conjectures for melts of hyperbranched stars. As already pointed out, the Gaussian star assumption should be relevant under melt conditions assuming a large spacer length $S \gg S_\star$. That this holds can be seen by rewriting Fixman's Gaussian chain criterion, Eq. (3.6.1), for melts

$$1 \gg \frac{v}{N}\, \rho^2 R_\star^d \approx v\ N/R_\star^d \tag{3.7.1}$$

remembering that the bare excluded volume $v \sim \epsilon$ has to be rescaled by the total chain mass N [12].[9] The hyperbranched stars should thus remain Gaussian below an interaction energy $\beta\epsilon_\star \approx R_\star^d/N$. Since $\beta\epsilon$ is not a parameter which can be readily tuned experimentally over several orders of magnitude, it is of some importance that Eq. (3.7.1) sets equivalently a *lower* bound $S_\star \ll S$ depending on the generation number G. Following the discussion at the end of Sec. 3.6 for excluded volume effects for single stars this

[9] A similar criterion $1 \gg \beta w \rho^3 R_\star^d$ should hold for θ-solvent conditions with $w > 0$ being the scale of the three-body interactions. Gaussianity thus requires $w \ll w_\star \approx R_\star^{2d}/N^3$. Note that the upper critical dimension for θ-solvents being $d = 3$, this condition does not depend (up to logarithmic corrections) on the spacer chain length S.

implies

$$\begin{aligned} S_\star &\approx \left(2^G/G^{d\nu}\right)^{1/(d\nu-1)} \text{ and} \\ S_\star &\approx \left(G^{(d_\mathrm{f}-d)\nu}\right)^{1/(d\nu-1)}, \end{aligned} \tag{3.7.2}$$

respectively, for regular dendrimers and for finite-d_f power-law stars in the melt. This scaling prediction is sketched in Fig. 3.13 for several architectures. Hyperbranched stars should remain thus Gaussian (albeit with a renormalized effective statistical segment length [13, 1]) as long as $S \gg S_\star$, if the interaction parameter $\beta\epsilon$ is switched on as in the recent study of linear chain polymer melts [1]. Details may differ somewhat, of course, since the spacer chains may not be rigorously Gaussian due to long-range correlations related to the overall incompressibility of the melt [23, 1]. It is thus possible that even the self-similar stars of imposed fractal dimension $d_\mathrm{f} = 2.5$ for the Gaussian reference ($\epsilon = 0$) may swell somewhat. We do conjecture, however, that this "swelling" for interacting large-S hyperbranched stars in the melt remains *perturbative* as long as $d_\mathrm{f} < d = 3$. Basically, each chain builds up a concentration $\rho_\star \approx N/R^d$ around its center of mass. Monomers belonging to other chains are depleted from this region, since the total density $\rho \gg \rho_\star$ can be assumed to be constant. This constraint causes an effective repulsion energy $\beta U \approx \rho_\star/\rho \sim N^{1-d/d_\mathrm{f}}$ between chains and chain segments [12, 23, 1]. The ensueing swelling becomes thus perturbative for $1 > d_\mathrm{f}/d$ [1].

Considering the dynamical properties of strongly interpenetrating hyperbranched stars for $S \gg S_\star$ assuming local MC moves or standard Langevin thermostat molecular dynamics [20], it will be of some interest to characterize the mean-square displacement of the star center of mass or, even better, the associated displacement correlation function [1]. As for the center of mass motion of linear polymer melts [1], strong deviations from the Rouse scaling are to be expected. Due to "viscoelastic hydrodynamic interactions" this should happen even if reptational effects [13] can be neglected as is the case for a finite $\epsilon \approx 1$.

I turn now to the description of static and dynamical properties of melts of regular dendrimers computed by molecular dynamics simulation of a variant of the Kremer-Grest bead spring model.

Chapter 4

Starburst dendrimer melt

4.1 Background

In this section the static and dynamical properties of starburst dendrimers will be discussed.

The field of hyperbranched star-like polymers, developed in the late 1970s [116], has exploded during the past decade [28, 117]. In the beginning considered only as a part of the polymer and material science, quickly this new class of macromolecules has found its place in the interdisciplinary field between organic chemistry, medicine, biology and biotechnology.
An evaluation of their structure and behavior details advantages that dendrimers have over other polymeric architectures in those fields. Just to name a few, their globular structure makes them perfect additives for lowering viscosity, multivalency could be a useful in the case for biomedical applications, possible cavities present in dendrimers could hinder other molecules or the active chemically terminal-groups to transport them to a target place. Those particular molecules hold huge potential addressing lots of potential applications.
Currently there is a controversy in the literature [118] as to whether those molecules can support hollow center structure and if they do become 'colloid-like' for high generations. This study is treating this problem by means of computer simulations.

The behavior of starburst dendrimers is related to their architecture that implies the space filling geometry where increase of degree of 'backfolding' comes along with growing generation number. Molecules should, at least in principle, collapse and form compact objects similar in their behavior to colloids. Encapsulation of the end groups leads to the isolation of the active sites. Usage of such materials can be fruitful. But what will happen if we will increase the branch length? That could promote molecules to form

entanglements and result in a gel.
We will try to answer to this, and other related questions in the following chapters.

4.2 Technical side

In order to solve the given problem we must choose methods that will satisfy our needs. There are a number of them, each of which has different functionality. To be successful in achieving our goals we have to balance between [119]:

1. System details (length scales),
2. Time scales of the simulations compared to the relevant experimental time,
3. Available computer power,
4. Effort needed to implement a method.

4.2.1 Methods

A central issue in the studies of complex structures is to understand the topological structure and then study its effects on the dynamical properties. Structure and conformation hold the static information and keep also the key to dynamic information that helps us to understand functionality and mechanism of the investigated material. Access to the dynamic information is limited due to the expensive calculation. Molecular simulations often requires millions of time steps to reproduce such behavior. Additionally growing complexity increases the difficulty of the calculations. For this reason one has to choose optimal method for the simulations.

Complex materials despite their continuum appearance at macroscopic scales have very fine structure at microscopic scale. It is tricky to efficiently build correlations between those two scales by catching the characteristics of the micro-world and reveal the behavior of the whole sample. Timescales at what laboratory experiment are performed are not reachable by the full atomistic computer simulations. For this reason a coarse-graining method is widely used [21, 84, 120]. It means that the chemical detail specific for each polymer are neglected and only excluded volume and topology (chain connectivity) are the properties that determine system behavior. In our simulations Kremer-Grest model [71] was used. Pairwise interactions between beads are govern by the purely repulsive interactions turned off for the nearest neighbors in a chain. A molecule swells and we end with what is called an excluded volume polymer. We used the flexible bead-spring model. The typical extension of a spring between connected beads $l_0 = 0.967\sigma$ prevents polymers from crossing during simulations. Term for the unbounded interaction describes van der

Waals repulsive interatomic forces in the form of shifted and truncated Lennard-Jones potential, Eq.(2.1.1).
The time evolution of the system is under the influence of a reservoir system formulated by the Langevin equation. Non-bonded interaction are treated by a Lennard-Jones shifted potential. Intramolecular interactions inside a molecule that are responsible for the restoring forces reactions are drawn by harmonic potential with strength $k = 3k_BT/l^2$, where k_B is a Boltzmann constant, T is the temperature and l is the equilibrium bond length.

Direct comparison to experiment is possible only under certain boundary condition imposed on a system [121].
Firstly, we have to determine *spatial boundary conditions*. To avoid any surface effect at the boundary of the simulated system, periodic boundary conditions are imposed. It means that the particles are enclosed in a box that is surrounded by infinite array of periodic copies of itself. When a bead leaves the box on one side it is replaced by the copy entering the cell on the opposite side. Still each bead is subject to the potential from all beads around.
To predict thermodynamical quantities from the simulations on has to provide *thermodynamical boundary conditions*. They can be selected from the range of extensive and intensive quantities like: total number of particles N_t, chemical potential μ, volume V, pressure P, energy E or related temperature T. Those quantities will specify the thermodynamical ensemble that is sampled during a simulations. One has to remember that more important then have very precise calculation is the sampling of a proper phase space. That will preserve fundamental dynamical properties such as energy, momentum, time-reversibility, and symplecticness [122]. According to statistical physics, physical quantities are described by large collection of systems, each representing the microscopic states (configurations), distributed in accord with a certain statistical ensemble.
For our purposed we have used the microcanonical (NVE) ensemble. To add the effect of the surrounding molecules on the motion, system was coupled with a thermal bath where constant temperature is kept by applying a random force together with a related fixed frictional drag force. That was done by introducing a Langevin dynamics obeying the fluctuation-dissipation theorem. This is equivalent to keeping the thermal bath in a state of thermodynamic equilibrium or close to it [123].
Another set of boundary conditions are purely *geometrical constraints*. An example would be the bond-length which on average is kept stable.
MD simulation provides a configurations that evolve according to Newtonian dynamics.

4.2.2 Technical information, calculation methods, data storage and visualization methods

The need of dealing with a realistically large system create a question of choosing a method and implementation. For our purposes of simulations of the large molecules in a melt we have decided to use Molecular Dynamic (MD) simulations [20, 21] that solve equation of motion for the trajectories of particles interacting through Lennard-Jones potential defined already by Eq.(2.1.1). This method been extremely successful to model classical many-body systems.

At each discrete time step positions and velocities of particles are written down and can be used to calculate equilibrium and transport properties of the system. That translates into the demand of large data space. The cost of such step is usually colossal. Fortunately used algorithms seem to translate well into parallel codes. A split in the memory usages into many processors made possible the simulations of larger and more complicated molecules such as our branched polymers. MD simulations is as well one of this areas where application of GPUs has grown significantly. Lack of the need of the message passing speed up the calculations. On the other hand for the largest systems calculation decomposition to spread the system among different processors and tasks is still more efficient. We have combined those two methods.

To equilibrate the system we have mostly used HOOMD-Blue (Highly Optimized Object-oriented Many-particle Dynamics – Blue Edition) [124] software designed to work on NVIDIA graphical cards. Their architecture was prepared for resolving complex computational problems in a little of time compared to a working time on CPU. This was as well a safety procedure since initial system, very unstable because of lots of overlapping molecules and loose Gaussian-type bonds, could not work well with task division and message passage between many processors. OpenMP (Open Multi-Processing) used by HOOMED-blue supports shared memory that supports the calculation on one machine what allows to increase the cutoff in case of the box division. Lack of the network communication speeds up the simulation.

For actual simulations we have used LAMMPS (Large-scale Atomic/Molecular Massively Parallel Simulator) [125] code written to work on single or multiple CPUs using MPI (Message Passing Interface). Such architecture allows for the spatial decomposition dividing the work into many processors. For large system it is a perfect solution that decreases the time needed for the simulation drastically.

Smaller simulated systems (approx. 700,000 monomers) were treated by using 48 CPUs while the large once (up to 1,600,000) by 64 CPUs. Already equilibrated systems being stable allowed us to submit jobs with higher parallelization level.

This project needed an intermediate degree of parallelization (48-128 processors communicating efficiently), but it was still necessary to study many such systems to test a big

parameter space (chain length, generation).
Both of the used codes performed NVE integration via Velocity-Verlet algorithm where position are updated every time-step. Time-dependent position of a certain monomer is given by $\mathbf{r_i}(\mathbf{t})$. Velocities $\mathbf{v_i}(\mathbf{t})$ are not generated directly but one can compute them from the positions. Their knowledge is essential since velocities determine the kinetic energy and temperature of the system.
From the point of view of statistical mechanics, MD is a method of conformational sampling [126] where structural and thermodynamic properties are created by averaging. Since the most stable configuration stand for global minimum by letting the program run for sufficiently long time we can hope to overcome energy barriers and fall into it. Next section will describe this procedure in details.

4.2.3 Equilibration of dendrimer melt

After energy minimization equilibration has been performed. It has allowed the system to relax and reach desired equilibrium configuration. Positions and velocities were updated each timestep with the use of NVE integrator. A limit $d_l = 0.05\sigma$ on the maximum distance an atom can move was imposed since an initial configuration contain lots of overlapping beads. To push them apart a soft sphere potential was used since, contrary to 'hard' potential like Lennard-Jones, the energy is not infinite when two molecules overlap and varies continuously depending on the relative positions of the particles. It computes pairwise interaction as below

$$E = A[1 + \cos(\frac{\pi r}{r_{cut}})], r < r_{cut}, \tag{4.2.1}$$

where r_{cut} is the cutoff radius. A coefficient A, that has energy units, was increased from $A = 1$ to $A = 100$ to penalize the overlap. At this point beads were separated and hard shifted Lennard-Jones potential was turn on. At the same time compression of the system from a dilute one do the dense melt was performed. After reaching desired number density $\rho = 0.85$ samples has undergone further equilibration under NVE integrator and Langevin thermostat (without the limit for the beads movement).
Letting the system undergo a thermal equilibration that disorders the system and drive a system into its global minimum. Nevertheless the real problem is that it is difficult to make a clear statement saying that a sample is fully equilibrated. We have decided that stable energy, pressure, and conformation (form factor and radius of gyration), as shown on Fig. 4.1, are enough to say that the real simulation can start. The timeframe for equilibration was dependent on the sample (different amount of particles, chain lengths, number of branching points that made the samples relax in a different timeframe). Apart of that we have checked if the orienational time correlation functions Fig. 4.2 for all bonds

in an arm[1] in the molecules given by the equation

$$P_1(t) = \langle \cos\theta(t) \rangle \tag{4.2.2}$$

$$P_2(t) = \frac{1}{2}\langle 3\cos^2\theta(t) - 1 \rangle \tag{4.2.3}$$

Fast decay to zero of the correlation function at longer times show that the bonds does not favor any specific direction and the system is fully equilibrated.

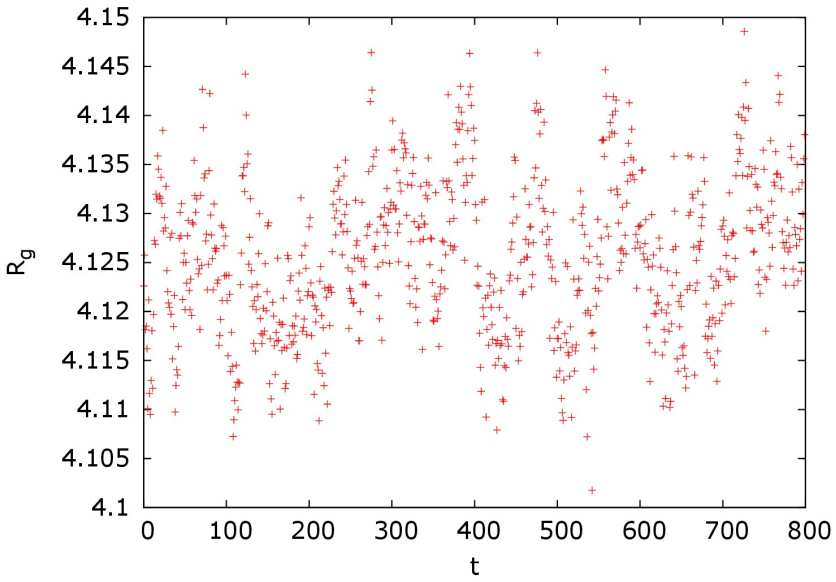

Figure 4.1: Equilibration of dendrimer melt. System equilibrium is established when pressure, total energy, radius of gyration and form factor are stable through time. Data for a system with $S = 4$ spacers in a branch and generation $G = 3$.

[1]By 'arm' we mean here a path between the core bead and the terminal group

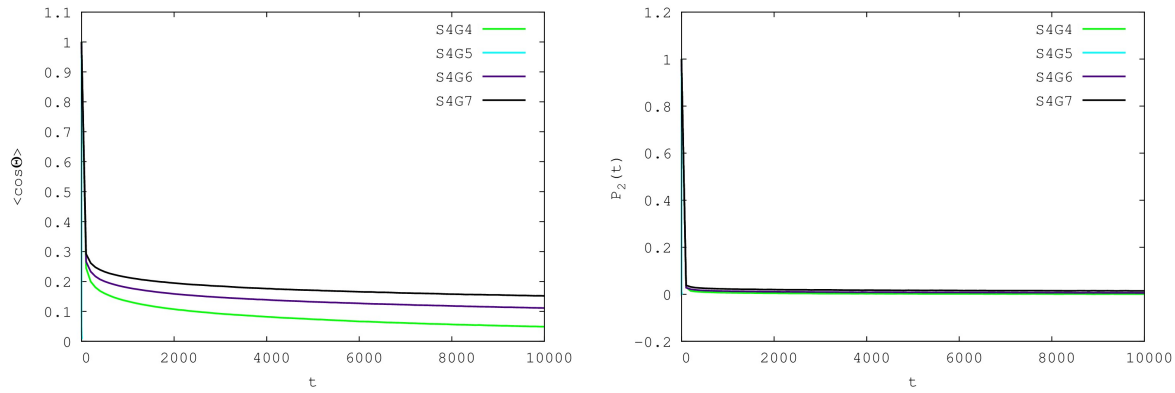

Figure 4.2: The time depencence of orientational correlation functions for the chains defined as the path between the core and the terminal group for all such chains in the system plotted as a function of simulated time t for starburst polymer with spacer $S = 4$ ($D_{4,4}$).

4.2.4 Simulated samples

Dendritic molecules can be built by repetitive growth stages that are called generations branched to a central core with, in our case, functionality $f = 3$. Let $D_{G,S}$ ($G \geq 0$, $S \geq 1$) be a dendrimer with G generations[2] and S a branch length (length of an attached chain functioning as one of the branches). To form a dendrimer we start with one bead and attach to it $f = 3$ linear chains of length S. A dendrimer $D_{0,S}$ is a star and has three arms each of them terminated by an end group (terminal group). Any further grow step is constructed by linking an end group with two chains of length S. Let $N(G, S)$ denote the number of beads in $D_{G,S}$ added at last iteration, then

$$N(G, S) = 3S \cdot 2^G \tag{4.2.4}$$

as it was already stated in a previous chapter.
Despite of its self-similar architecture, dendrimers are not fractals since mass growth is exponential and volume increase much slower so the number of iterative steps is limited. That result in an infinite fractal dimension.
What interests us, is the limit of long branches. It would not be correct to make simply bonds longer. For this reason, to make the branches longer, we place more beads between branching points that are in a distance not allowing them for crossing.
Those open, covalently bonded assemblies when radially symmetrical are called starburst dendrimers and simply dendrimers when there is one unit between branching points.

[2]We have to make a remark at this point that in this Chapter we start counting generations from "0", while in the previous one, a star was treated as having generation "1".

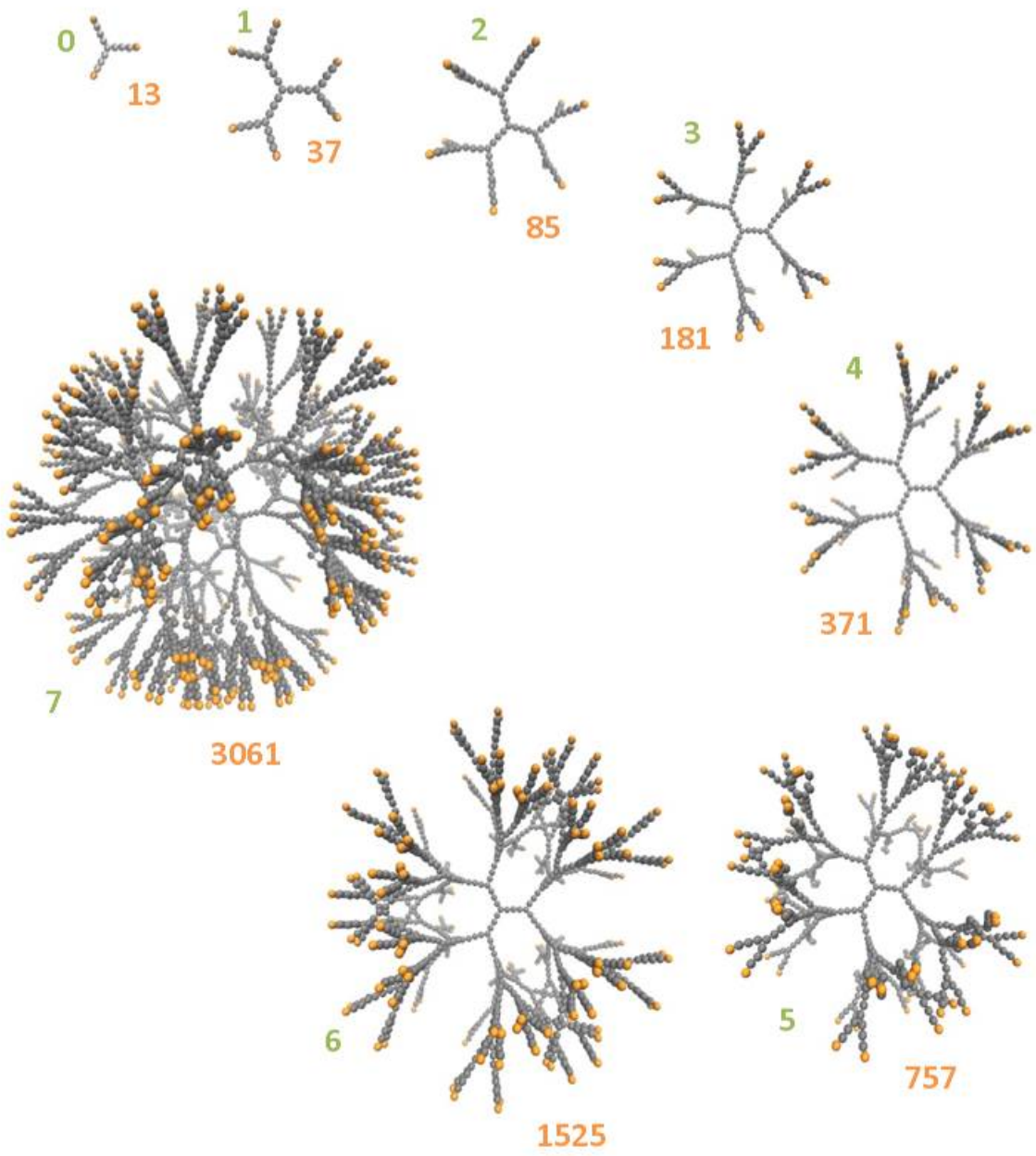

Figure 4.3: Step growth of the hyperbranched starburst polymers, with $S = 4$ and generations from $G = 0$ to $G = 7$ (green numbers). Under each molecule its mass is given (orange numbers). Those snapshots shows only stretched molecules to increase the visibility. For the same reason terminal groups are represented by orange beads contrary to the rest that is grey.
From those snapshots it is visible how fast does the mass grow with each generation and how dense a molecule itself become.

Table 4.1: All simulated dendrimer systems. Parameters that we were changing were the length of the arm from $S = 2$ to $S = 64$ and generation number from $G = 0$ to $G = 7$ (and $G = 9$ for $S = 2$). By construction mass of each molecule grows fast with generation. For having good statistics it is better to have lots of molecules in on simulation box. This number varies a lot because of the available computational time limitations.

S	G	N	nr of molecues in a box	nr of beads in a box
2	0	7	1000	7000
2	1	9	1000	19000
2	2	43	1000	43000
2	3	91	1000	91000
2	4	187	1000	187000
2	5	379	1000	379000
2	6	763	512	390656
2	7	1531	343	525133
2	8	3067	125	383375
2	9	6139	125	767375
4	0	13	1728	22464
4	1	37	1728	63936
4	2	85	1728	146880
4	3	181	1728	213768
4	4	373	1728	644544
4	5	757	512	387584
4	6	1525	216	329400
4	7	3061	216	661176
8	0	25	1728	43200
8	1	73	1728	126144
8	2	169	1728	292032
8	3	361	1728	623808
8	4	745	512	381440
8	5	1513	216	326808
8	6	3049	216	658584
8	7	6121	216	1322136
16	0	49	1728	84672
16	1	145	1728	250560
16	2	337	1728	582336
16	3	721	512	369152

16	4	1489	512	762368
16	5	3025	216	653400
16	6	6097	125	762125
16	7	12241	125	1530125
32	0	97	1000	97000
32	1	289	1000	289000
32	2	673	1000	673000
32	3	1441	216	311256
32	4	2977	216	643032
32	5	6049	125	756125
32	6	12193	125	1524125
32	7	24481	64	1566784
64	0	193	1728	333504
64	1	577	512	295424
64	2	1345	216	290520
64	3	2881	216	622296
64	4	5953	64	380992
64	5	12097	64	774208
64	6	24385	64	1560640
64	7	48961	27	1321947

4.3 Static properties of hyperbranched star-like polymers

4.3.1 Radius of gyration

Now we will bring our attention to the size changes of the molecules. The radius of gyration indicates the extension of a molecule giving information about the spatial distribution of a mass within a molecule. Here it is useful to remind the concept of a fractal geometry that, in short, provides a rational description of a complicated structures.
A molecule can be considered as a mass fractal if its growth leads to self-similar structures over an extended scaling regime and is translationally invariant.
Polymer fractality is visible only on length scales of the mean square radius of gyration (it is a finite construction) $\langle R_g^2 \rangle = \langle (r_i - r_{CM})^2 \rangle$, where r_i and r_{CM} are coordinates of the beads and center of mass of the molecules, respectively. A square root of this quantity will be further called simply R_g. It indicates the overall size of the macromolecule by reflecting the distribution of the beads in a relation to each other. For linear chain polymers the radius of gyration scales as[12]

$$R_g := \sqrt{R_g^2} \sim N^{\nu} \sim N^{1/d_f} \tag{4.3.1}$$

as defined before by Eq.(3.1.1). The fractal dimension d_f of the object quantifies the degree to which it fill the space and can be used as a useful measure of the spatial complexity of the whole system [127]. Albeit fractal dimension is often used to quantify the degree to which an object fills its space, dendritic structures are not fractal objects in the strict mathematical sense. As a consequence a simple relation between dendrimer properties and its fractality cannot be stated. Still this value could be used to quantify space-filling tendency.
Some of the experimental results [128, 129, 130], and computer simulations [36, 131] exhibit $d_f = 3$ what means that starbust dendrimers are compact, and space-filling objects. If one would consider a certain branched objects, as Zimm and Stockmayer [93] did, $d_f = 4$. Even stronger tendency to occupy any available space were indicated for high generations by Lescanec and Muthukumar [34] whose $\nu = 0.22$ ($d_f = 4.55$) and Wallace [132] with same results. All the results where $d_f > 3$ suggest that each newly added monomer has to be located in the periphery of the molecule since the structure is compact and homogeneous already. This is consistent with the model of de Gennes and Hervet [29] where end groups always occupy an outer shell. On the other hand their density profiles differ much from other results. They assumed that the R_g grows linearly with G, the outer shell density grows progressively and this is why density decreases when approaching the central bead.

Let us remind that the total mass of the dendrimer is calculated as

$$N = 3S(2^{G+1} - 1) + 1 \tag{4.3.2}$$

and the number of branching points (special case for a mass for a real dendrimer where $S = 1$) is equal

$$N_B = 3(2^{G+1} - 1) + 1. \tag{4.3.3}$$

We can see that by construction mass N is proportional to the spacer number S and if grows as a power of the functionality of the branching points $b = 2$ to the power G. In principle the spacer number acts as a scaling factor for the mass. So, object with the same generation and different S are self similar.

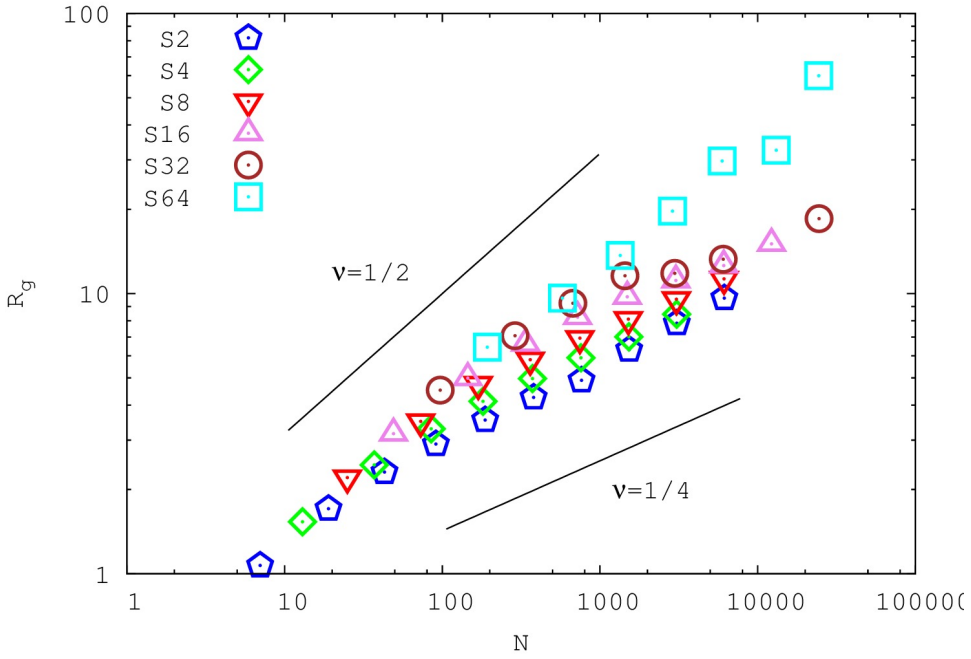

Figure 4.4: Double logarithmic plot of R_g against the mass N of the molecule. A power law for Gaussian chain $R_g \sim N^{1/2}$ and dense packing limit sketch boundaries for the molecule growth.

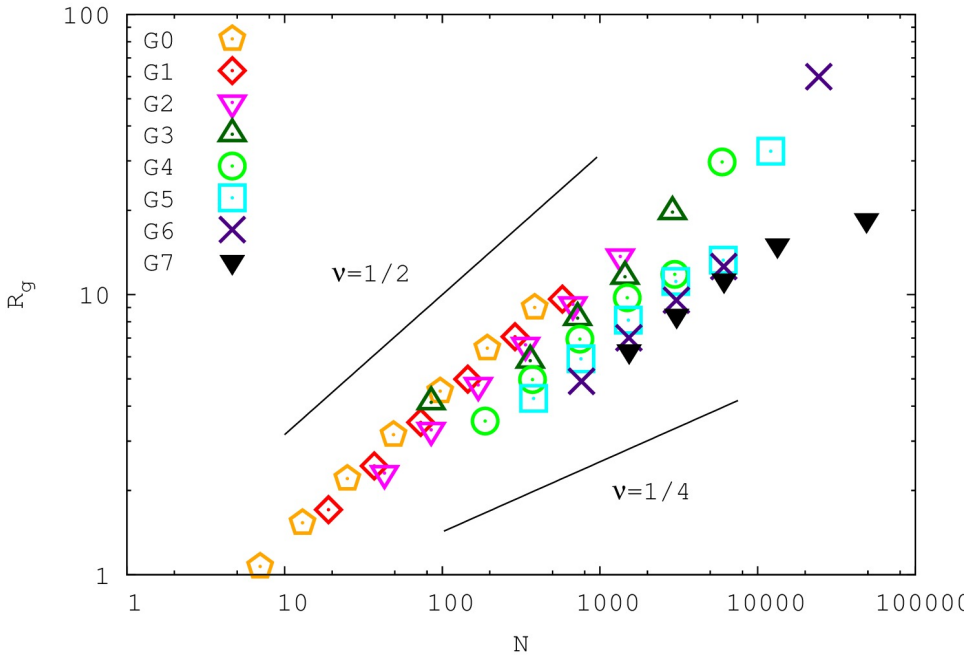

Figure 4.5: R_g as a function of mass colored by generation. Transition from loose like Gaussian limit to a compact structure through generation is visible

The scaling of the R_g with mass N does not work for all kind of simulated systems for the reasons mentioned above. Plotting R_g against a mass N gives us a distribution of points rather then a scaling law, see Fig. 4.4 and Fig. 4.5. Both plots are drawn in a double logarithmic scale to emphasize the changes. Both of them represent the same points but in the first one (Fig. 4.4) points are differ by the branch length S while in the second one (Fig. 4.5) by the generation G. As the mass N grows, the range of R_g widens but we can still sketch some limiting cases. Certainly the size cannot be more steep then the slope $R_g \sim N^{1/2}$ which characterize molecular growth for Gaussian chains with rather loose structure. Local fit to the molecules with the smallest growth follows the power-law $R_g \sim N^{1/2}$ which suggests that those starburst polymers grow as more and more compact globules.

Fig. 4.4 suggest as well that longer branches (bigger S) are closer to the Gaussian limit. Molecules with $S = 2$ are getting compact quite fast while those with $S = 64$ and $S = 128$ are more loose.

On the other hand we study the evolution of the R_g as a function of G on Fig. 4.5 (different coloring for the same points as on Fig.4.4). We can see that they to follow straight lines, what means that the $R_g(G)$ is related by power law with the mass. We find that the fractal dimension d_f increases as the G grows.

All above suggest that it is both spacer length S and the generation number G that affect the morphology of the studied systems. Actually its multiplication gives us the distance between the core monomer and the terminal group so the total arm length. As it is seen

on a Fig. 4.6 dependence of the radius of gyration R_g on the $S \cdot G$ is with agreement with a gaussian picture. The average conformation of the arm resemble that of a linear chain.

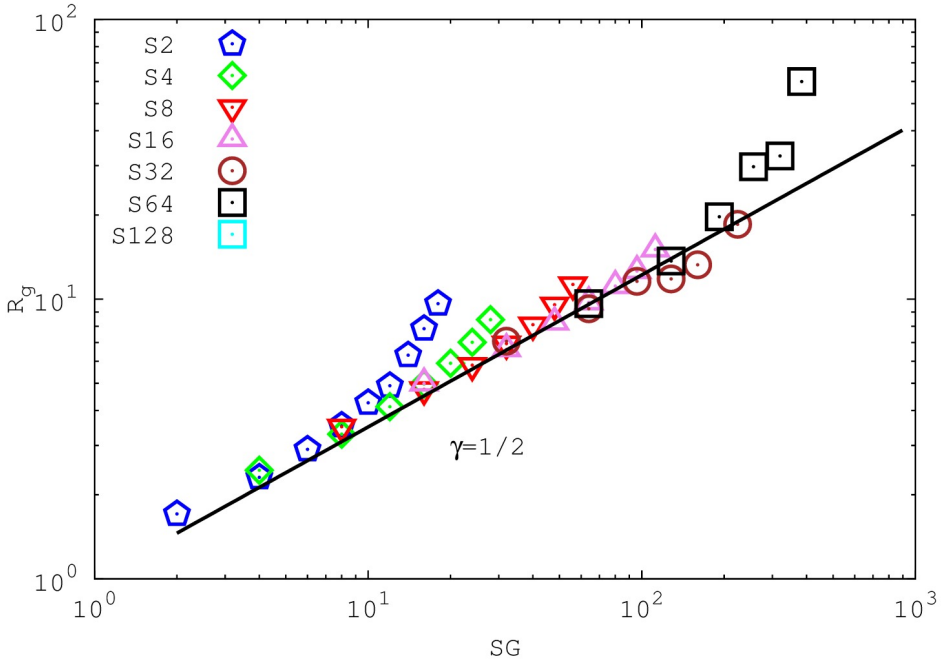

Figure 4.6: R_g as a function of the maximum path from the center to the terminal group. Same limit ($\nu = 1/2$) describes Gaussian stars.

Last plot Fig. 4.7 in this subsection depicts the changes in the molecules densities. The smallest generation number G follows the power law 1/2 what is expected for the Gaussian chain. Further on we can see nonmonotonous behavior. Firstly the density decreases to become more and more dense and finally, probably, saturate. With further measurements we will try to put more light on this behavior.

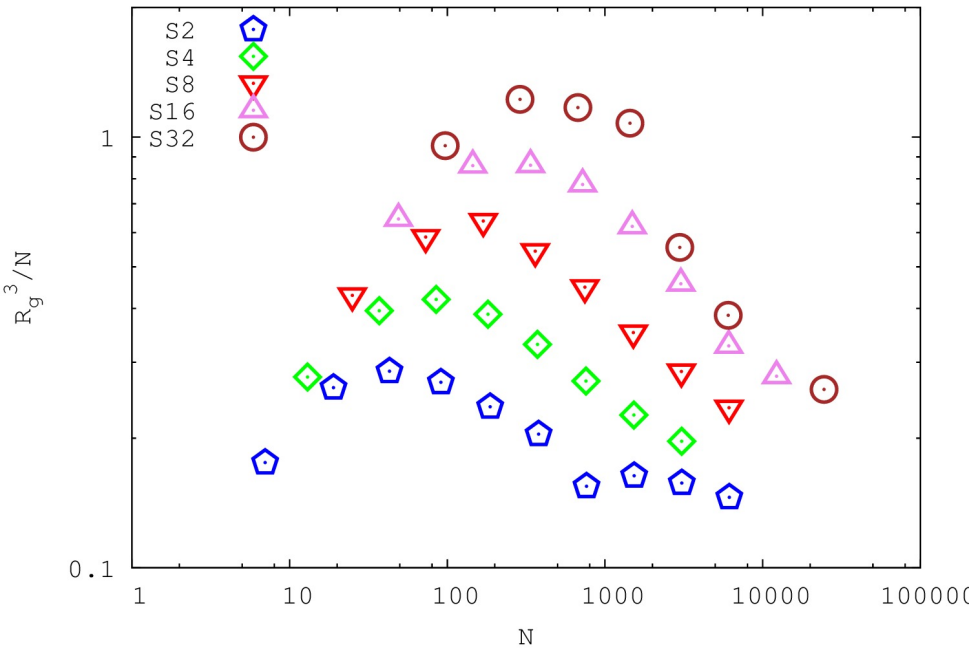

Figure 4.7: Inverse of the average molecule density as a function of its mass.

4.3.2 Contact number

The question arises if the systems show any evidence of entanglements or not. Molecules with long arms could penetrate neighboring ones easily. The longer the arm, the less constrained are its movements since branching points are further one from another. Finding the maximum number of molecules that touch a given one would give us a hint. We call it a contact number N_C.

Each bead has an assigned cutoff distance ($r_{cut} = 1.122$). Two approaching beads can form a new contact if the distance between their centers is equal or smaller then $d_C = 2 \cdot r_{cut}$. Same-molecule contacts and already counted between molecules were rejected from the calculations of the number of contacts.

N_C provides an evidence for both intermolecular penetration and retraction of terminal groups. Firstly, it grows with generation and arm length, Fig. 4.8. An arm growth make the structure more open and allow for more intermolecular communication. The maximum appears at generation three and it falls down starting with generation four. This provides a picture of two competing effects: growing of the steric crowding importance with increasing generation and flexibility that is stronger for long branches and allows to interpenetrate molecules. Interestingly for all arm lengths the contact number drops down (probably) to twelve. That is a contact number for non-overlapping spheres of the same size [133, p. 21]. It is easy to arrange twelve spheres so that each touches a central sphere. This leads us to the conclusion that starlike dendrimers are collapsing and resemble dense objects. Such behavior is very different from the linear chain conformation that tend

to entangle more when a molecular weight is increased. Still for such arrangements of spheres there is a lot of space left over. In principle, for hard spheres there is enough of a free space that two surrounding outer spheres can exchange places through a continuous movement in such a way that non of those twelve spheres will not lose contact with a central one. This is why we cannot say at this point if they are shaped as spheres or rather their outer arms are still wandering around.

Two plots demonstrate the situation Fig. 4.8. First one is scaled with the generation number. Systematic shift with spacer number is visible. Although mass could be identified as one of the factors in volume changes, it is not. When scaling N_C with it, the plots collapse to one line (dendrimers with the same mass but different branch length S have the same N_C) until generation 3-4. From this point the interplay between G and S is evident. N_C collapses for each S with different power. This is with agreement with previously calculated R_g^3/N (Fig. 4.7) where density was nomnonotonous due to, firstly, spreading arms around and penetrating neighboring molecules, and then getting more compact.

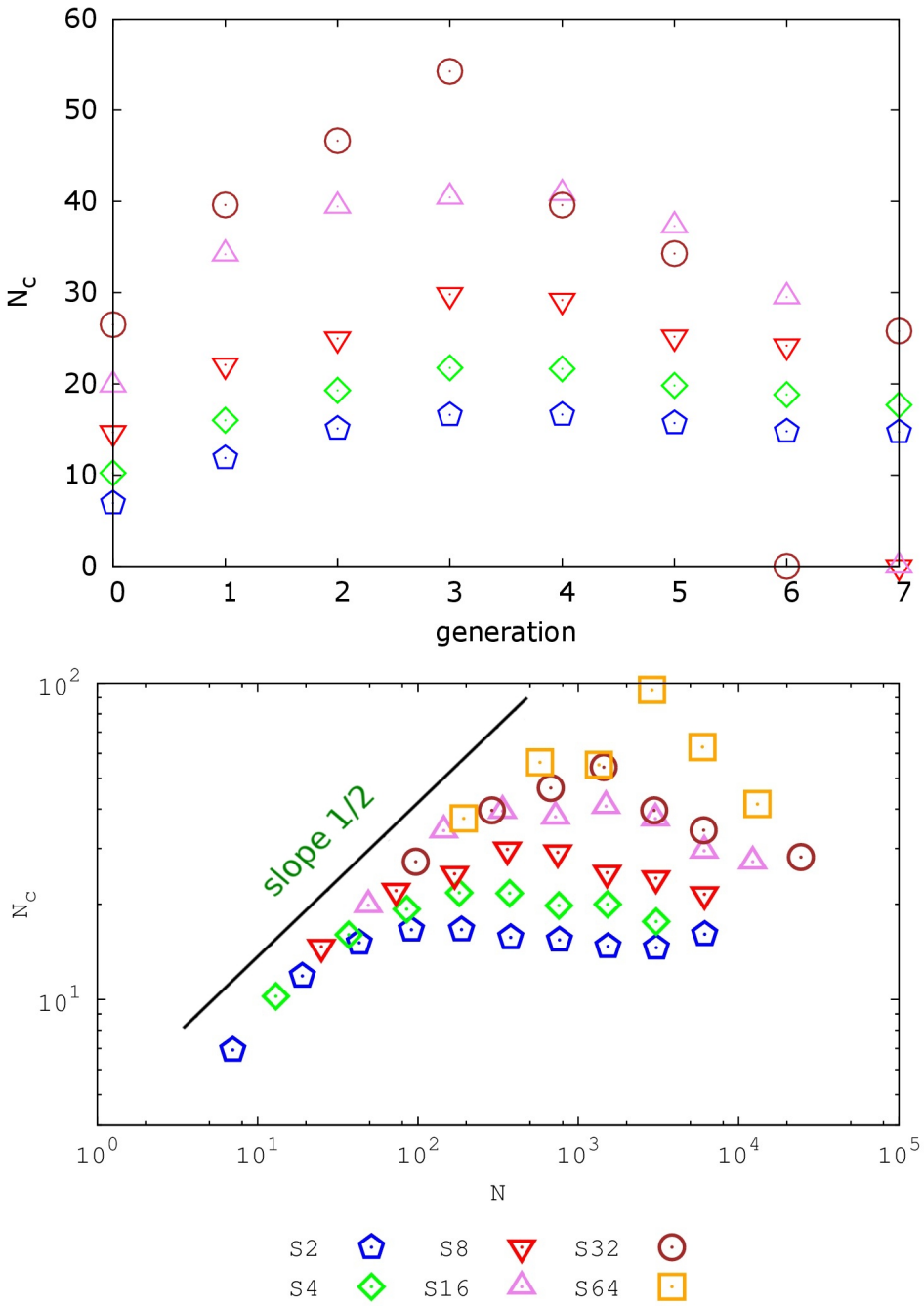

Figure 4.8: Number of contacts N_c for a given molecule as a function of generation (first panel) and molecular weight N (second panel). Each of the molecules approach a maximum around generation 3 and 4 to start decreasing for higher ones. At high generation number these molecules form compact coil structures, with the interior protected from penetration by neighboring ones.

4.3.3 Terminal groups

The situation common for many polymers is where their end-groups are chemically distinguishable from the backbone of the polymer. In a melt of linear chains the end groups

have negligible influence since, especially for high molecular weights, their amount is little in comparison with the whole mass. In this case reactive functional groups are only at the end since rest is spend to produce the polymer backbone. Differently to that dendritic structures posses large amount of end-groups despite of the synthetic procedure. These end groups can be used as easily accessible chemical modificators that can change physical material property. This is why it is essential to localize them within the molecule.

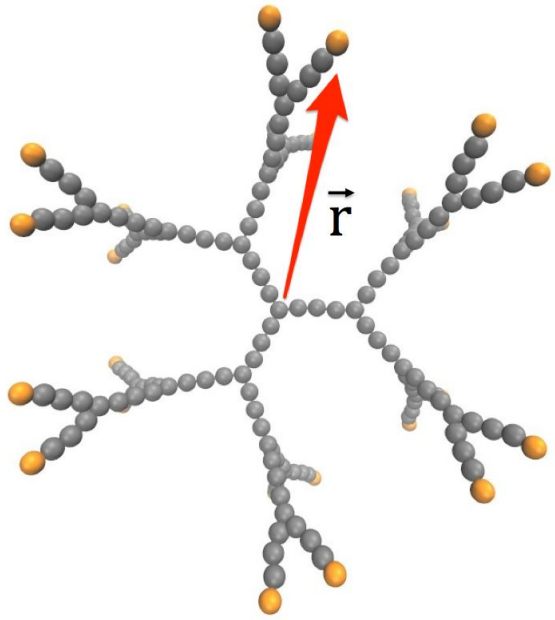

Figure 4.9: Sketch of a dendrimer with the core-to-end vector used for calculating terminal groups distribution.

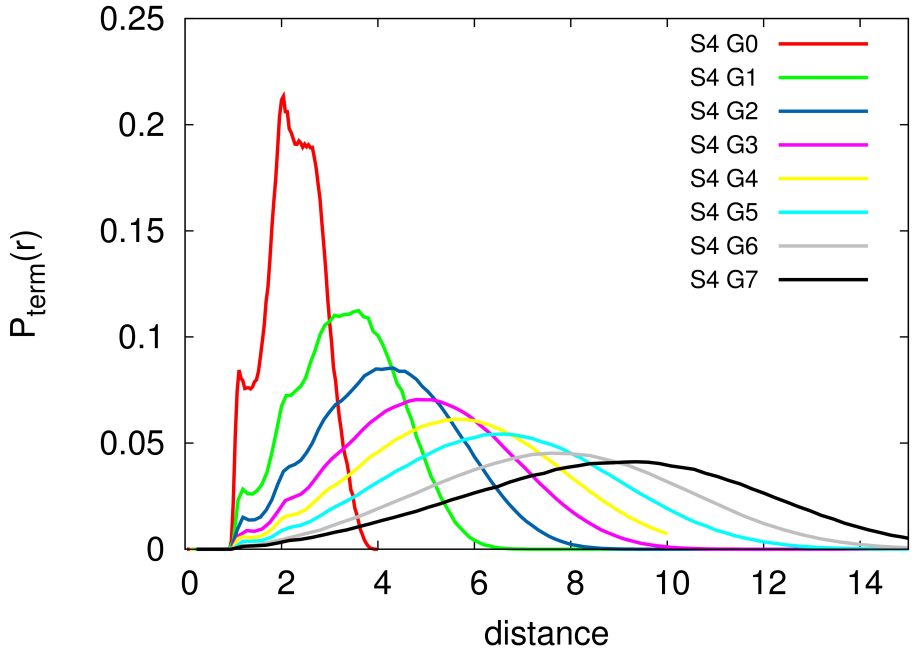

Figure 4.10: Terminal group distribution plotted as a function of the distance from the focal molecule. Terminal groups are spread through the whole molecule.

Closer look on the end-group distribution will shed light on the situation. In Fig. 4.10 information about the center-to-end vectors is given calculated from $\langle(r_T - r_0)\rangle$, where r_T is the position of the terminal group, and r_0 position of the core monomer.
End groups do not lie near the outer shell line but rather are dispersed throughout the molecule. That would happen only if the structure were rigid or other interactions, e.g. polar groups, were present.
Each end group has at its disposal more free volume then a backbone monomer. The number of possible conformation and mobility grows with increasing free volume. For this reason dendritic molecules tend to fold back or contract rather then stay stretched as it was suggested by de Gennes and Hervet [29]. Large mobilities allow branches to fold inwards in the direction of the center of the molecule. A significant retraction of the peripheral groups release steric crowding at the outer part of the molecule provoked by the architecture. This reduces its radius of gyration and a molecule shrinks.

4.3.4 Orientational correlations

To have a full characterization of a structure formed by branched arms, it is also necessary to investigate the behavior of their orientational degrees of freedom. While the beads are expected to rotate freely, geometrical constraints may push branches to form specific conformations. As it was suggested already, they may fold back to the center or be rather

retracted in the direction of the center. Both behaviors lead to a drastic condensation inside the molecule and pushing out the neighboring chains.

In order to check further the orientational conformation predictions we will calculate the first and the second order orientational correlation for average part of the branch (each of the path from the center to the end group are taken into account and averaged for better statistics). Since each branch is composed of consecutive vectors, first one is taken as a reference. When calculating orientational distribution correlation, function is calculated by taking the average of the projection of one bond onto another and plotted as a function of a number of vectors. This value will tell us how does the direction of the chain change with its length. These values are given by

$$P_1 = \langle \cos\theta \rangle \tag{4.3.4}$$

$$P_2 = \frac{1}{2}\langle 3\cos^2\theta - 1 \rangle \tag{4.3.5}$$

where θ is the angle between the orientation of the first bond and the orientation of the consecutive bonds. In Fig. 4.11 below, the orientation distribution function of vector composing the path 'core - terminal group' is presented.
Values for P_1 are enclosed in a range $[-1, 1]$, where 1 indicates that no orientational change was performed while -1 correspond to head-to-tail alignment. Plotting P_2 - result in a range $[0.5, 1]$.

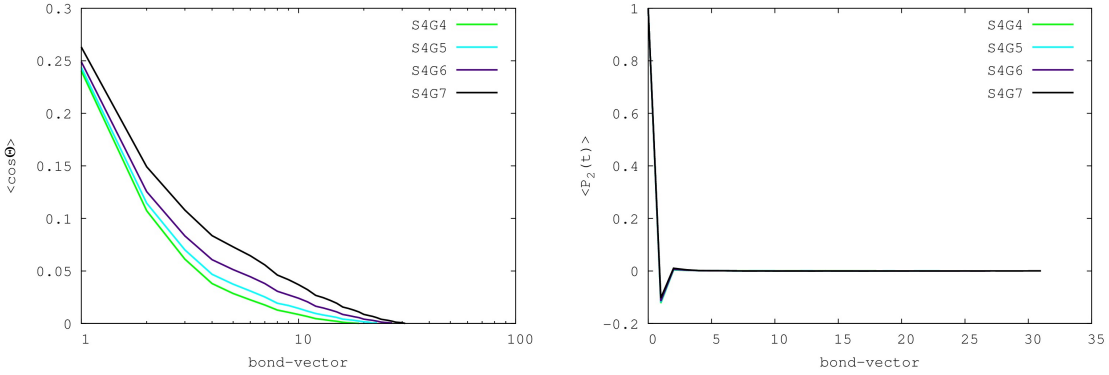

Figure 4.11: Orientational distribution function for the chains defined as the path from the central bead to the terminal group. $bond - vector$ stands for consecutive bonds in a chain counting from the focal molecule's bead. Data for the dendrimer of type $D_{4,G}$.

Our results indicate that bonds belonging to one branch do stay correlated over a certain distance, Fig. 4.11, what is stressed by representing the projection of the bond s in a semi-logarithmic plot. It becomes more prominent with growing generation. That could be an indication that the bonds have preferred directionality, i.e. they are stretched out.

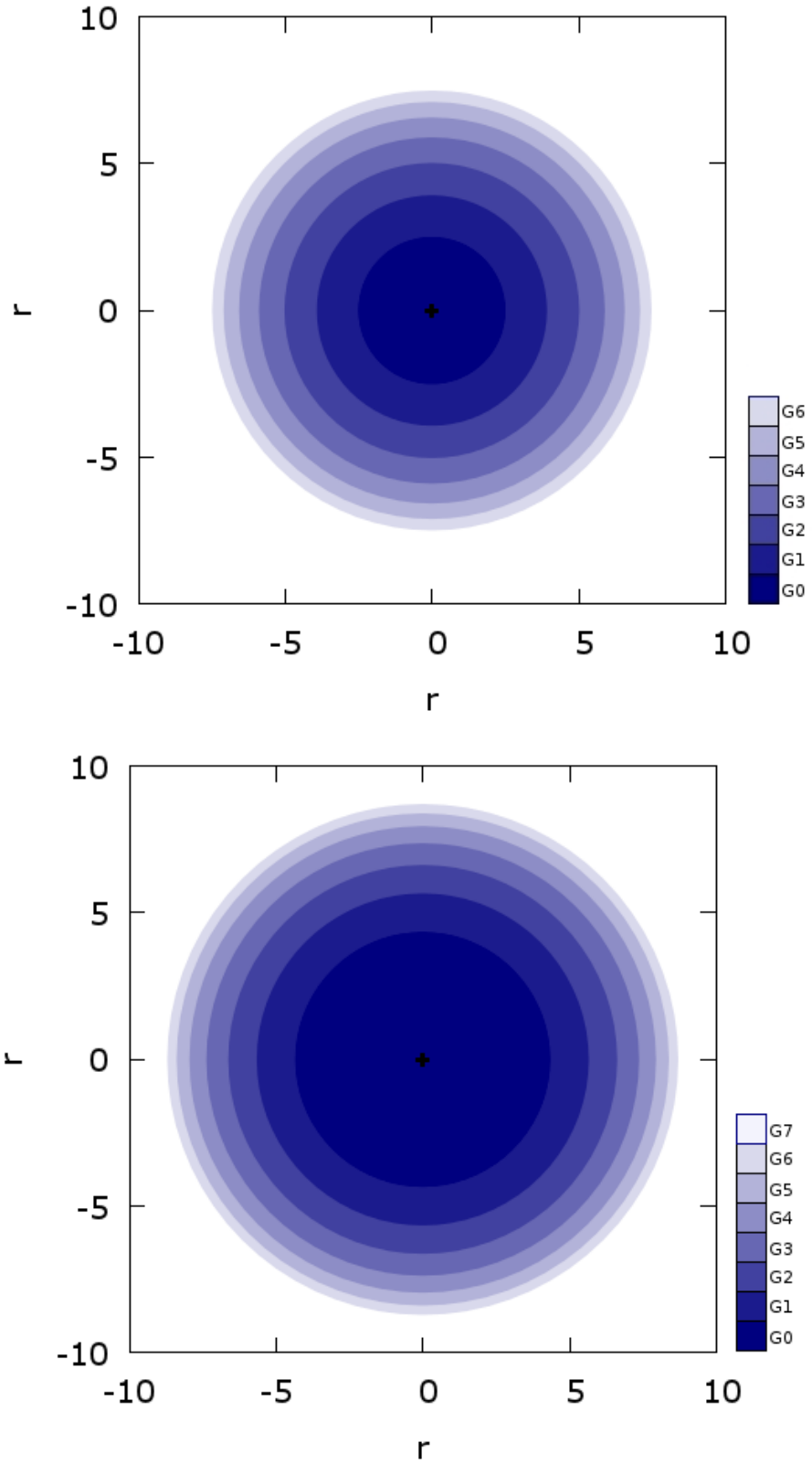

Figure 4.12: Average distance of the branching point for consecutive shells from the central bead for a molecules $D_{4,6}$ and $D_{4,7}$. Drastic change in the area sketched by the most inner circle suggest strong stretching of the central chains for molecules with high generation number.

A glance on Fig. 4.12 depicting positioning of the shells in a molecule for the case of $D_{4,6}$ and $D_{4,7}$ confirm this prediction. Border of each circle represents average position of branching point for consecutive generations. There is a drastic change in the radius of the most inner circle denoting the average positioning of the branching points of the $G = 0$. For the $D_{4,7}$ the radius of this sphere is much larger then for the $D_{4,6}$. This actually means that the central chains are stretched when the molecules generation is high enough.

4.3.5 Pair distribution function

To characterize the structure of the system it is not necessary to know the exact position of all monomers. Alternatively, one can use a quantity that will determine the probability of finding pairs of monomers with given relative position. Interactions among particles have no preferred direction in the homogenous fluid in equilibrium. For this reason, one can simplify the distribution function to one dependent on distances only. It is the pair radial distribution function $g(r)$, that envisage the probability of finding a monomer at certain distance from another one compared to the ideal gas distribution [11]. The $g(r)$ can be calculated by

$$g(r) = \frac{V}{8\pi r^2 N^2} \langle \sum_{i=1}^{N} \sum_{i \neq j} \delta(r - r_{ij}) \rangle, \tag{4.3.6}$$

where $r_{ij} = |\mathbf{r}_i - \mathbf{r}_j|$, N is the number of particles and V the volume of the system. For liquids, systems between highly ordered crystals and completely chaotic gases, it has a small number of peaks that are decaying to a constant value at larger distances.

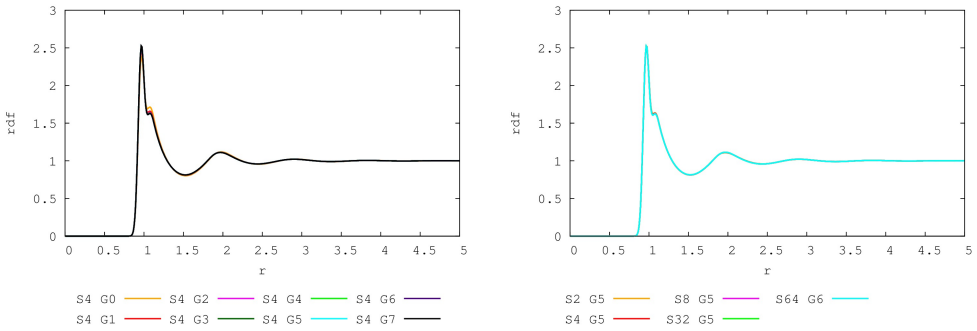

Figure 4.13: Radial distribution function for all monomers for various generation ($D_{4,G}$) and for changing spacer length ($D_{S,5}$). All plots collapse to one apart of the little shelf that emerges on the further from the center slope of the first maximum.

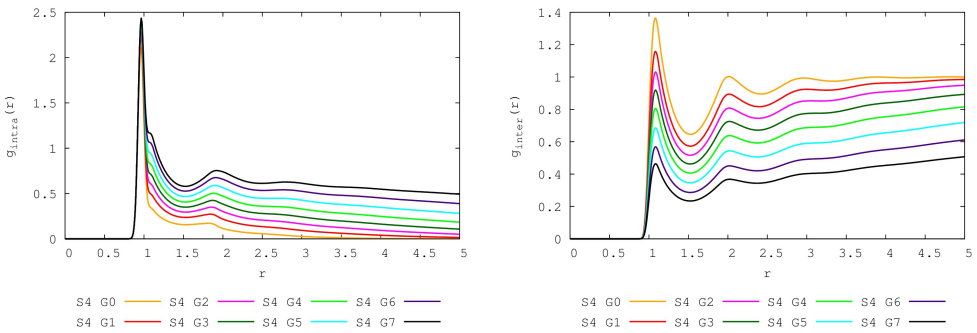

Figure 4.14: Intra- and inter-molecule contribution (left and right plots) to the pair radial distribution function.

Total radial pair distribution function, meaning for all monomers in a system, of starburst polymers are shown in Fig. 4.14. In all cases plots are almost identical with peaks corresponding to different generation shells. First appears at position $r = 1$, just after rising from zero due to the strong repulsive forces between neighboring monomers. Interesting point is the broadening of the first peak by a small shelf. It means that there exist non negligible amount of nearest neighbors for which the average distance separating them is bigger then it is predicted by the bead-spring construction. Further maxima are of the liquid type and they do follow a standard trend and drop out $g(r) \longrightarrow 1$ at large distances.
Second plot in a panel shows the $g(r)$ as well for all monomers but across different spacer lengths to show that systems, if not account for the molecules structure individually, are very similar.
Both inter- and intra-interactions contribute to the total radial distribution function Eq.(4.3.6). Left plot in a panel 4.14 broaden our understanding of the molecules structure. It depicts the intra-molecular radial distribution function $g_{intra}(r)$. Low generation number have a shape standard for a liquid where single peaks decay quite fast. The growth of the first maximum and the appearance of the second one as a function of generation is a consequence of higher molecule mass constrained to a certain volume and in a stronger ordering inside the molecule. What is more interesting, as well the previously mentioned 'shelf' attached to the first peak appears. It broadens in a very organize way the volume where the first shell around the center of a mass appears. This means that some of the nearest neighbors, that naturally would be placed in the closest possible distance taking into account a repulsive forces, are actually pushed, or pulled, further from the center. The amount of them is big enough to see a strong effect in a radial distribution function. Last plot in a panel 4.14 shows the inter-molecule contribution $g_{inter}(r)$ to the radial distribution function. Position of the first peak brings contribution to the 'shelf' in a $g(r)$. Contrary to intra-molecule part, it decays with generation. For higher generations G molecules are more compact and penetration inter-penetration is weak. As a consequence

all peaks are smearing out and plots are lowering values.

An analysis of the performed calculations shows that a short range order is establish in the range of first coordination shell. Broadening of the first peak by incorporation a shelf into it indicates that some of the beads are subject to additional forces beyond the short-range repulsive one between monomers.

4.3.6 Form factor

Form factor $F(q)$ reflects the intramolecular interferences in the range of chosen $\underline{q}$, a Fourier variable that is representing a scattering wave vector, and characterizes single molecule size and shape [15]. It has been defined already before Eq.(3.5.1).

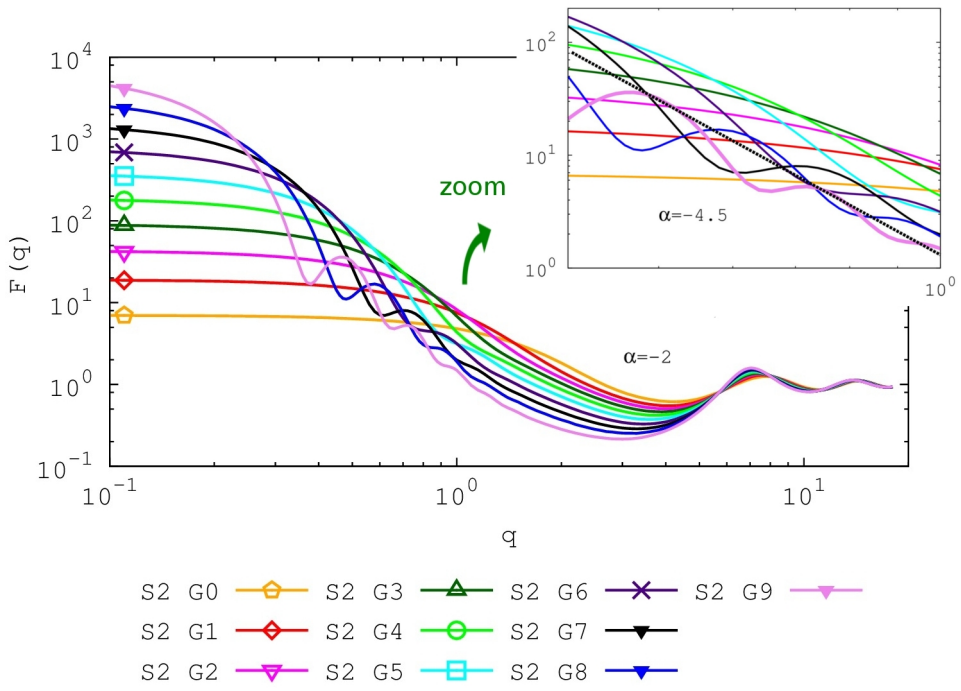

Figure 4.15: Form factors as a function of $\underline{q}$ vector for molecules with $S = 2$. To underline the influence of the generation on the molecular shape, those molecules were simulated up to generation $G = 9$. As generation grows the curves changes from the smooth linear one in the intermediate regime to one with bumps revealing more compact structure where light scatters mostly from its "surface". For better visibility this regime was zoomed. A form factor for a sphere with a radius $R = \sqrt{5/3}R_g$ was fitted to underline the compactness of the molecules with high generation $G = 9$ (dashed line).

In experiments, form factors can be measured only in the dilute regime where particles are considered as independent, non-interacting scatterers [1]. When analyzing the data

from the simulation, we consider a single molecule, forgetting about the neighboring ones, so there will be no direct interactions contributing to the scattering function coming from other molecules.

For the small $\underline{q}$ where $\underline{q} \cdot \underline{r}_{ij} \leq 1$ ($\underline{r}_{ij}$ refers to the displacement between two scattering elements, beads in our case), the light scattered from both i-th and j-th scattering sources is essentially in phase, resulting in the constructive interference [134]. The amplitudes of the scattered $\underline{q}$ vectors sum up. As a consequence $F(q)$ measures molecular mass. This is visible in the limit $\underline{q} \longrightarrow 0$ in Fig. 4.15. At higher $\underline{q}$, where $q > R_g^{-1}$, with R_g the radius of gyration, measurement is sensitive to the internal structure of a polymer. What interests us the most is actually the intermediate scattering regime. Those wave vectors enter the regime where the internal molecular structure is probed. In this case $\underline{q}$ corresponds to the probe length comparable with the dimension of the molecule.

For lowest generation $G = 0$ we observe smooth curve typical for a Gaussian chain that, by increasing generation G, changes into a curvy one exploring emerging sphere-like shape - another indication for strong arm retraction and molecule shrinking. Such oscillatory structure appears for the first time for $G = 5$, in agreement with previous simulation studies [35, 38, 40, 135].

Once the $F(q)$ is calculated, on can try to interpret it by going through different equations proposed for $F(q)$. We have found a very good fit with a form factor $F(q)$ for a sphere

$$F(q) = 9(\sin(qR) - qR\cos(qR))^2/(qR)^6 \tag{4.3.7}$$

where $R = \sqrt{5/3}R_q$ (that relation holds for a sphere [136]), and R_g was taken from previous calculations. Even the maxima pointing the overall molecules size are indicating the same values for the $F(q)$ calculated for a starburst dendrimer and a sphere. That confirms the previous predictions that starburst dendrimer resamble a compact sphere for high G-values. Such change in the slopes shape is with a good agreement with experimental studies [137, 138, 139].

Actually similar results but for multi-arm polymer stars were provided by Pakula [140] for the molecules with high functionality f. This is reasonable since dendrimers with large number of branching points (high generations), that shape them into a colloidal structure, act like large amounts of arms for a stars.

Finally we reach distances at which we probe scattering from individual monomers. Since all beads are identical and the number density was kept same for all of the systems, plots collapse at this point.

The Kratky plot provides valuable information on the overall shape of the molecules and the size of segments. The interpretation comes from the Debye's formulas characterizing a Gaussian coil that was used by Kratky, Porod and coworkers. It has been used to inter-

pret a scattering experiment data. The Kratky plot gives the scattering pattern as $q^2I(q)$ versus q. On the other side Porod predicted a power law $F(q)_{q\to 0} \sim \frac{K_P}{q^4}$ where K_P is the Porod constant. A tail of such a curve will drop to a plateau at distances where sharp interfaces are visible (revealed as the coherent scattering). The intensity of light diminishes proportionally to the reciprocal of the fourth power of $\underline{q}$. Corresponding Kratky plot will reveal bell shape for a well defined globular molecules. In a random coil the coherence is destroyed by randomizing the directions of the scattered phonons. Therefore, this plot of a Gaussian chain will exhibit a plateau in high $\underline{q}$-region.

Morphology is well reflected in the form factors calculated for all samples. The Kratky plot of the form factor, $F(q)q^2R_g^2$ vc. qR_g is plotted in Fig. 4.16 for $S = 2$ and different generations. Such representation highlights the changes in the intermediate $\underline{q}$-regime [33] where we can see the evaluation of the shape due to the changing generation G. By plotting a scattering data in this form we remove the length scale dependence and emphasize the differences rising from density distributions. The x-axis qR_g is unit-less and R_g was determined by direct calculations. It is seen that plots go through all kinds of conformations from coil-like shape $G = 0$ to the compact one $G = 7$. Any deviations from an asymptotic curve indicates a non-Gaussian behavior of investigated systems. At low $\underline{q}$-values, all curves tend to collapse to one revealing a universal behavior. Only for high generation number, where topology alter the compact shape, first peak is clearly resolved due to a high density of the branching points [33, 38, 113]. Location of the first order-peak is shifted to the higher $\underline{q}$-values for less compact molecules which is visible as well in Fig. 4.17. The maximum lies in the range $1.64 \ll qR_g \ll 1.93$.
From this we can read that the overall shape does change drastically with generation and slightly but still visibly with a spacer length S. The maximum become more pronounced with increasing branching density [113] that is the generation number G which is visible in Fig. 4.17. Besides the major peak at $qR_g \approx \sqrt{3}$, a secondary peak appears for the system with high density of branches and is placed around the value $qR_g = 4.8$ what is consistent with previous simulations [38] and positioning of the second maxima of a solid sphere with the same R_g. Lower G and sparser branching causes dying out of the secondary peak where chains are trying to recover the horizontal asymptote.

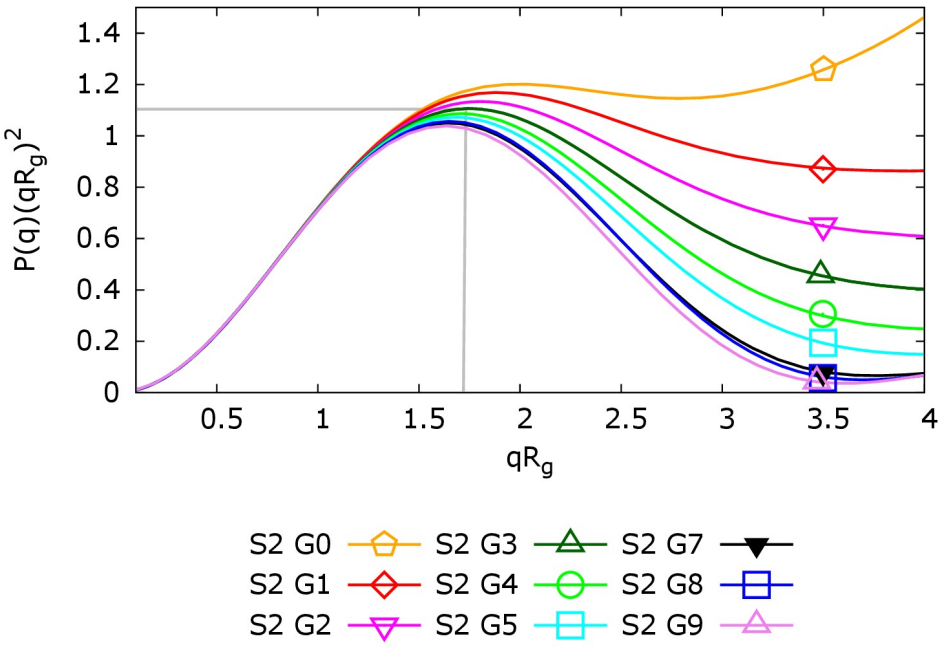

Figure 4.16: Kratky plot for the studied systems of the type $D_{2,G}$ with changing generations.

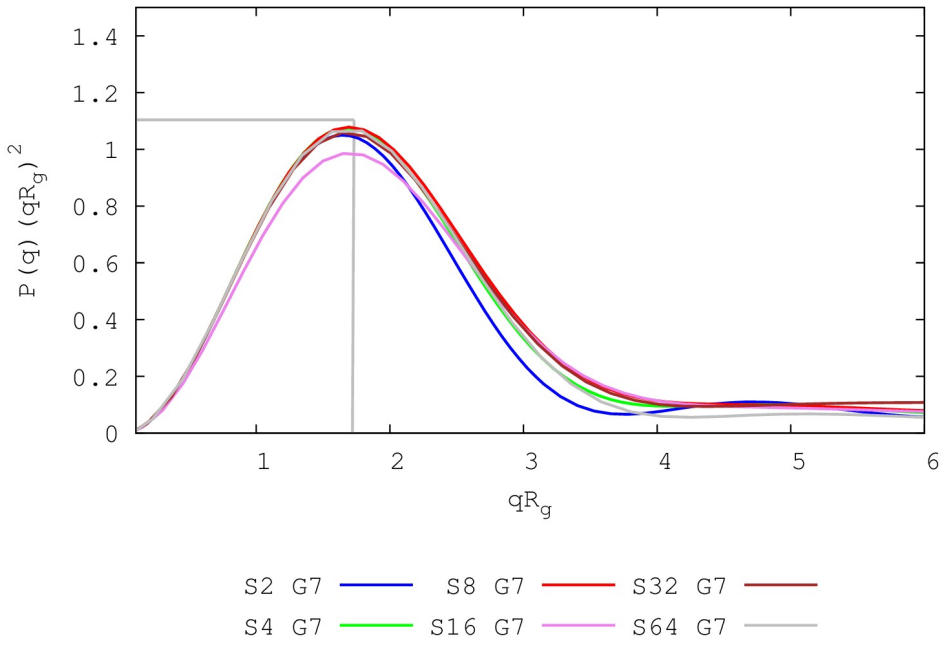

Figure 4.17: Kratky plot of the structure factor for $G = 7$. Molecules takes a compact form what is reflected by the bell-shaped Kratly plot. Maxima stayes at the same point, and minor peak appears.

4.3.7 Static structure factor

The interparticle static structure factor $S(\mathbf{q})$ is defined as the autocorrelation function[11, 141]

$$S(\mathbf{q}) = \langle \rho_{\mathbf{q}} \rho_{-\mathbf{q}} \rangle, \tag{4.3.8}$$

where

$$\rho_{\mathbf{q}} = \sum_{j=1}^{N} \exp(-i\mathbf{k} \cdot \mathbf{r}_j) \tag{4.3.9}$$

is the Fourier transform of the microscopic (total) density, N is the number of particles and $\mathbf{r}_j$ is the position of the j-th particle. The contribution from $S(q)$ cannot be neglected for a dense systems like a melt where molecules interact strongly. The structure factor $S(\mathbf{q})$ is dependent on the local degree of order in the measured sample (a spatial distribution of the scattering sources) and an interaction potential between them. Static structure factor for solids has a form of sharp peaks. In liquids, due to the thermal motion, the intensity of Bragg peaks is reduced and leads to a significant suppression as an indication of loss of structural correlation [142]. As we can see in Fig. 4.18 and Fig. 4.19, a large first peak corresponds to the most probable distances between the monomers, and is followed by a sequence of peaks with decreasing intensity, confirming the loss of spatial correlation. In the simulation, we are restricted in measurement to certain distances and for this reason we can see only part of the scattering spectrum. First one, at a distance $q \approx 6.9$ corresponds the the diameter of a bead, which is the smallest distance that can divide two of them.

Two plots, $F(q)$ and $S(q)$ merge to qualitatively similar values at distances corresponding to short range repulsive interactions between beads. That situation changes with decreasing a topology complexity. Substantial penetration of non-bonded beads into the closest neighbor shell stimulate an overestimation of the first peak. As for systems with rather loose construction, where chains are strongly interpenetrating, ($G = 0$), collective interactions ($S(q)$) dominates over single-chain ones ($F(q)$) as shown on Fig. 4.18.

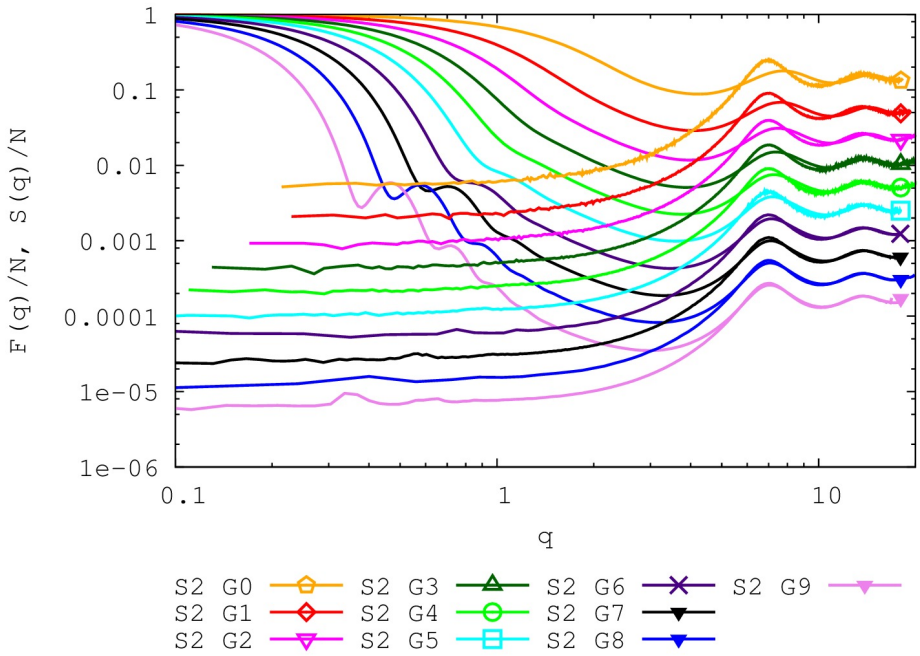

Figure 4.18: Form factor $F(q)$and static structure factor $S(q)$ corresponding to the radial distribution functions of the samples $D_{2,G}$ both normalized by mass to make the plots distinguishable at high $\underline{q}$. At the distance corresponding to the interparticle distances in a system, for low generation number intensity of the $S(\underline{q})$ peak dominates over the one coming from $F(\underline{q})$ indicating high level of molecule penetration.

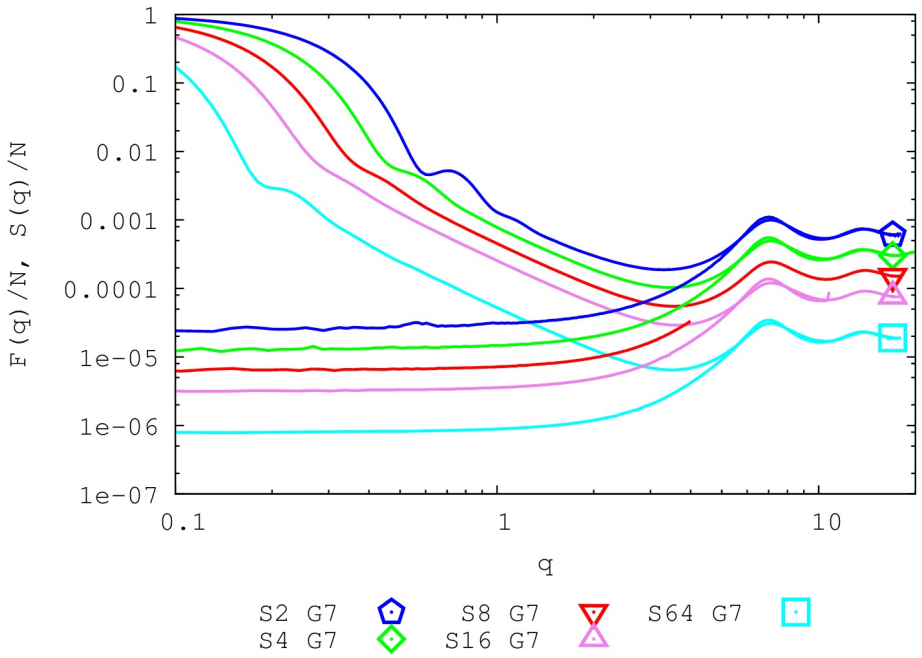

Figure 4.19: Form factor $F(q)$ and static structure factor $S(q)$ normalized by mass for high generation numbers corresponding to the radial distribution functions in Fig. 4.13 of the samples with high generation number $G = 7$.

4.3.8 Compression modulus

When changing $\underline{q}$ we can focus on different length scales in the system. By probing low $\underline{q}$-values we get information about the structure of the molecule. High $\underline{q}$-values contains information about the smallest elements of the molecule in a melt. Going down to really small $\underline{q}$ values, no small-scale information can be obtained anymore. In this regime scattered intensity depends only on the osmotic pressure fluctuation. In that (hydrodynamic) limit one can describe a melt by a bulk compression modulus, which is a measure of a fluid's incompressibility. It is of fundamental importance since it helps to control the melt flow properties. For this reason its measurements are of extreme value.
Previously, in Sec. 2.3.2 compressibility was calculated from the volume fluctuations Eq. 2.3.1. When using this equation it is necessary to investigate system for many different densities which is a disadvantage. For this reason we will probe the data from the previously calculated structure factor $S(q)$

$$\kappa = \lim_{q \to 0} \frac{S(q)}{k_B T \rho} \tag{4.3.10}$$

where low-wavevector limit of the structure factor $S(q)$ was approximated at its plateau to 0.
In general, since we are not changing the density, compressibility stays the same for all

simulated samples, $\kappa = 0.04$. There are no deviation even for high generation number G.

4.3.9 Density profiles

Next attempt to characterize the conformation has been done by calculating dendrimer internal density profile. For dendrimers it is given by the number density as a function of the radial distance r from the core,

$$\rho(r) = N(r)/4\pi r^2 \delta r, \tag{4.3.11}$$

where $N(r)$ is the number of monomers in a given shell. The output is determined by the amount of beads in every shell of the thickness $\delta = 1.0\sigma$ apart of the first one where only one bead is closed (we end up with an onion-type shell structure).
The commonly accepted model assumes a box shaped density profile called sometimes a dense core model. It predicts that the density is the highest in the center and it decays monotonously (of course the highest density would be in the strict center where the central bead is placed).
In the case of a star ($G0$), density decreases with a distance r from the central monomer Fig. 4.20. In general, for coil like conformations, the monomer density $\rho(r)$ is expected to be high in the center and decay in the limit of $\sigma \ll r \ll R_g$. De Gennes [12] showed using general arguments for self-similar objects, that the number density $\rho(r)$ follows the equation used already in a Sec. 3.4 $\rho(r) = \frac{1}{r^{d-d_f}}$, where d is the actual dimension of the system and d_f a fractal dimension of investigated object. For coil-like conformations the relation takes simply a from $\rho(r) = 1/r$ which is the case of zero potential interactions. It can be compared with the density distribution of the starburst objects (G0) with long branches Fig. 4.20. Long-branched stars in a melt are similar with their behavior to self-avoiding walk due to their simple topology. However, the higher the generation, the more branching points are present what leads to complicated connectivity and an increase of potential interactions that modify the density profile [143].

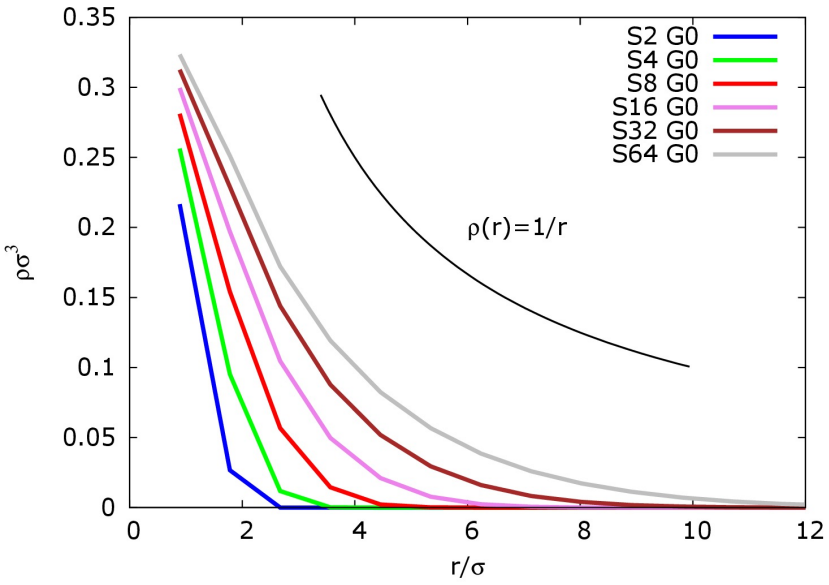

Figure 4.20: Density profile for star polymers ($G = 0$). The decay similar to one of the coil-like model conformation is visible.

From Fig. 4.21 (two top panels) startling information emerges. Deviations from commonly accepted density profile occurs at higher generations where a hollow center appears. The highest density is at the very center of the molecule that contains a central bead. For clarity this point was taken out from all the plots in the Fig. 4.21. The functions show significant differences for molecules with different generations.

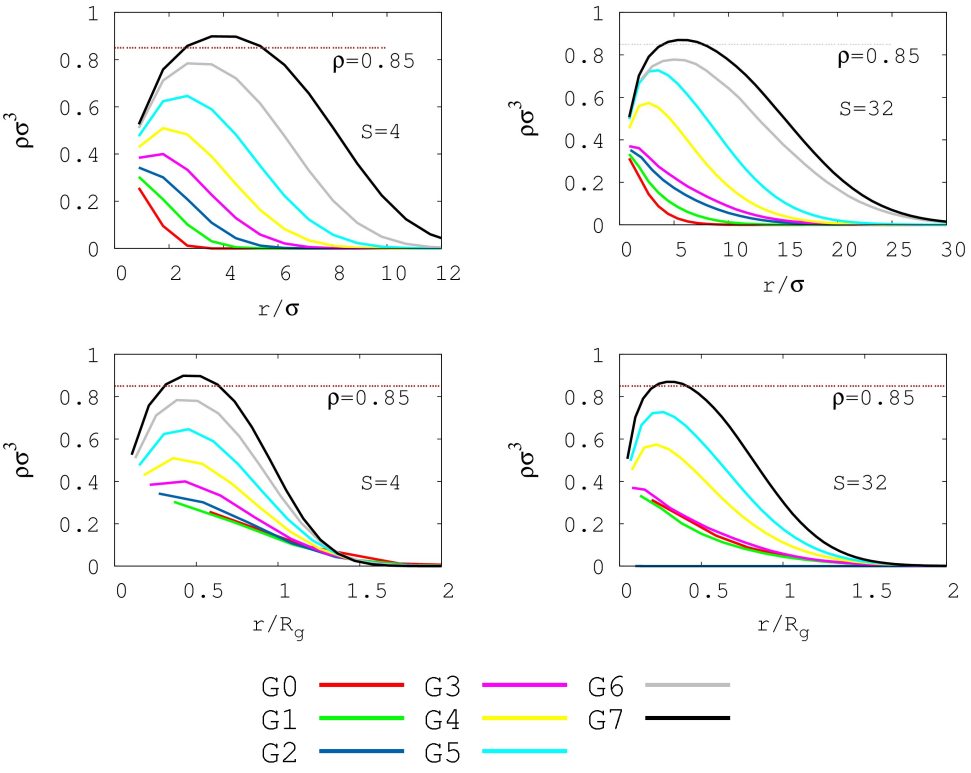

Figure 4.21: Density profiles for different starburst systems. Two panels on the left are plotted for systems with $S = 4$ and different generations. Panels on the right are done for the systems with $S = 32$ and changing generations. Top panels represent densities at certain distance. Two bottom panels shows same type of data but plots are scaled with R_g to highlight universal behavior. Dendrimers manifest a non-uniform radial density profile with a depletion near the central bead. What is interesting, for the highest generation $G = 7$ density around a center is even higher then the the number density of a system $\rho = 0.85$. This makes it impossible for other molecules to penetrate into the central part of the molecule.
A point at $r = 0$, effectively symbolizing the central bead, was taken out from the plot to clarify the figures.

In order to investigate this case further we have plotted same densities but scaled them with corresponding radius of gyration Fig. 4.21 (bottom panels). Density profile normalized with the radius of gyration does demonstrate a systematic shift. Maximum is not necessarily placed in the center or any specific point on the horizontal scale. In the case of low generation it is obvious that dendrimers undergo backfolding since there is no dense outer shell. This is due to the high flexibility of the scaffold.
Since the number of end groups is large in such systems, a free volume is increased, chains have more space to move making it more mobile and flexible. A 'dense-core' picture can be applied for the molecules with a low generation number.
Increasing generation comes along with hollow part close to the center in the density

profile. Typically for generations $G > 5,6$ $\rho(r)$ is going through a minimum around the center to increase significantly and then decrease towards the exterior of the molecule. Total density of the starburst polymers is constituent in a large amount of the last generation where 50% of the mass is enclosed. Since there are no significant changes in the end-group distribution, they are spread through the molecules. This effect is due to the inner generations that changes their distribution. This effect is stronger with increasing G and this dip is broadening with increasing S.
Central chains shall carry the load of the excluded volume effect of whole branches [35]. Tension imposed on the bonds is unevenly distributed over different segments since beads placed at higher generation suffer from crowding and are pooling central ones outside. Tension is concentrated in the close neighbor of the focal branching point in the center. Intriguing fact is that in the literature one can find examples of density profile with a hollow center for systems without explicit excluded volume interactions. One possible explanation is due to the entropy gain. Stretched central chains are unfavorable energetically but such construction increase a space and number of possible conformations for part of the molecules places further from the center and as a consequence an entropy. Since volume of shells grows as square of the distance from the center this gives a significant gain in volume and place for exploring different conformations. For this reason effect of hollow center should be more visible with growing the chain length because the gain in entropy for the beads far from the center would be bigger. As it is visible at increasing the length of the chain makes this effect more pronounced.
To conclude: conformational entropy rises due to the stretched central chains. Interaction between monomers that did come back close to the configurational center causes steric crowding. Because of those two effects only specific conformations, with hollow center, are favored. The maximum density is between a core and the periphery because of the backfolding of the end-chains.
Similar results were obtained earlier [35, 38, 39, 50, 144, 145, 146, 147].

All of this suggest that we are not dealing with fully collapsed molecules. Due to the chain stretching close to the center the inner part has a low density that increases to reach a maximum.

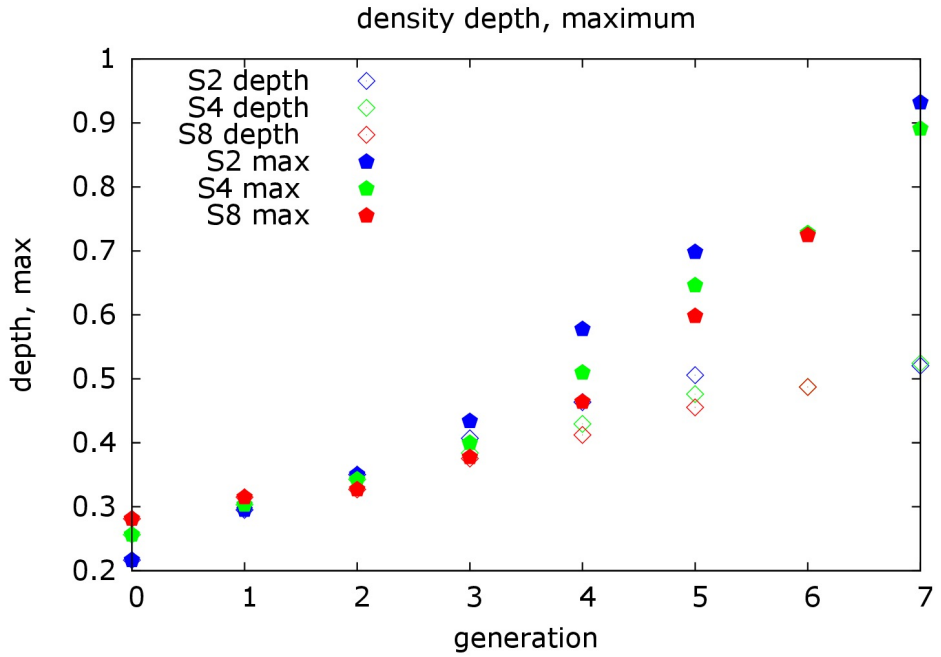

Figure 4.22: Number density at hollow part close to the center and at a point with a maximal density. This figure suggest that with growing generation difference in densities between those two points grows. Increasing spacer length S makes this effect slightly less pronounced.

4.4 Dynamical properties of starburst polymer melt

This section addresses the questions relevant to the dynamical melt behavior in equilibrium and under an external field condition. Because of a specific structure the flow behavior of those fluids is expected to be quite unlike that of simple chain polymers. Even for large spacer S (in the regime simulated by us), as it was pointed out before, there are no entanglements that would slow down the dynamics drastically. On the other hand, the intrinsic viscosity is expressed in volume per mass and relation between those two quantities is not (as it was shown in a previous section) given by unequivocal relation. The interplay of those effects could reveal an interesting behavior.

4.4.1 Self-diffusion

We will start with calculation of the mean square displacement (MSD) directly from the simulated trajectories of the particles. It is defined as

$$MSD = \langle |r_i(t) - r_i(0)|^2 \rangle \tag{4.4.1}$$

where $r_i(t)$ is the position of particle i at a time t and the average is taken over ensemble of particles. Alternatively, we can define center of mass mean square displacement (CM MSD)

$$CMMSD = \langle |r_{CM,i}(t) - r_{CM,i}(0)|^2 \rangle \tag{4.4.2}$$

with $r_{CM,i}$ being the center of mass position of the i-th molecule.

In the limit of long times, particles follow Einstein's relation describing a long time diffusion. It can be obtained by monitoring in time the mean squared displacement of tracer beads or of the center of mass of the molecules

$$D_S = \lim_{t\to\infty} \frac{1}{6t} \langle |r_i(t) - r_i(0)|^2 \rangle. \tag{4.4.3}$$

with D_S being the self-diffusion coefficient.

The time-dependent diffusion coefficient at sufficiently long times reaches the plateau that characterize the time-independent diffusion coefficient. Fig. 4.25 shows the computed curve for the CM MSD. Self-diffusion coefficient D_S, that is attributed to the thermal motion is equivalent to the diffusion for low concentrations of solute that determines the slope of the MSD and can be obtained from curve of MSD versus time. With increasing mass its value drops down rapidly (Fig. 4.26) in a similar manner even if architectures of the simulated molecules are different. Most of the points follow the -1 scaling with mass. Only the points for $D_{16,2}$ and $D_{16,3}$ are dropping down more rapidly. That could be a

consequence of strong interactions with neighboring molecules (we remind at this point that for generation $G = 3, 4$ the contact number N_C has its maximum).

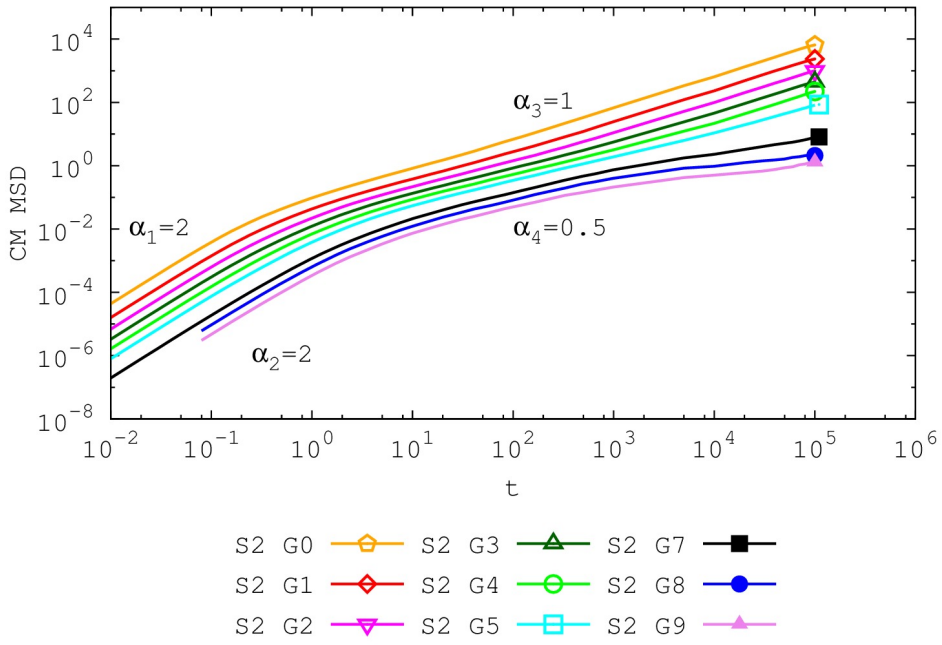

Figure 4.23: CM MSD for samples with spacer length $S = 2$. α_i refers to the coefficient of the local slope of the CM MSD.

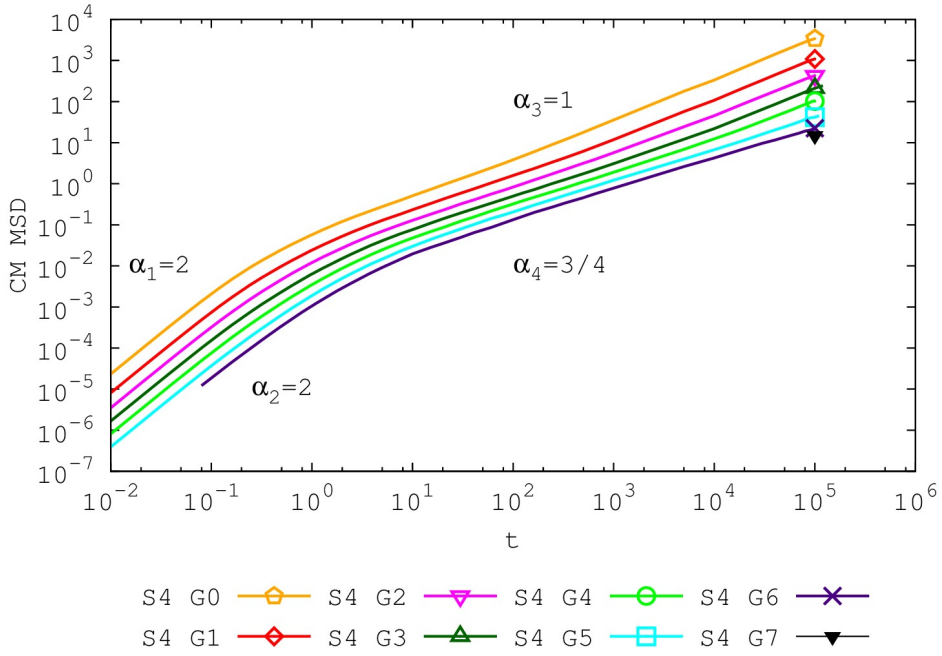

Figure 4.24: CM MSD for samples with spacer length $S = 4$

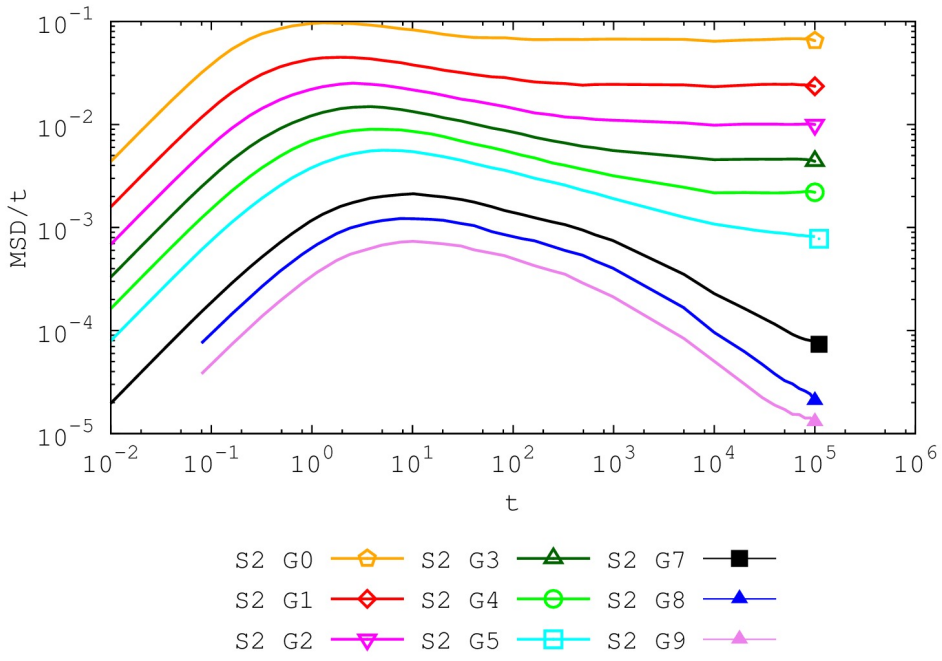

Figure 4.25: CM MDS curves which are divided by time for all generations of $S = 2$. The values from the plateau are used to calculate diffusion coefficient D_S. Not all systems were simulated long enough to reach a plateau, hence, for those ones the coefficient D_S cannot be determined.

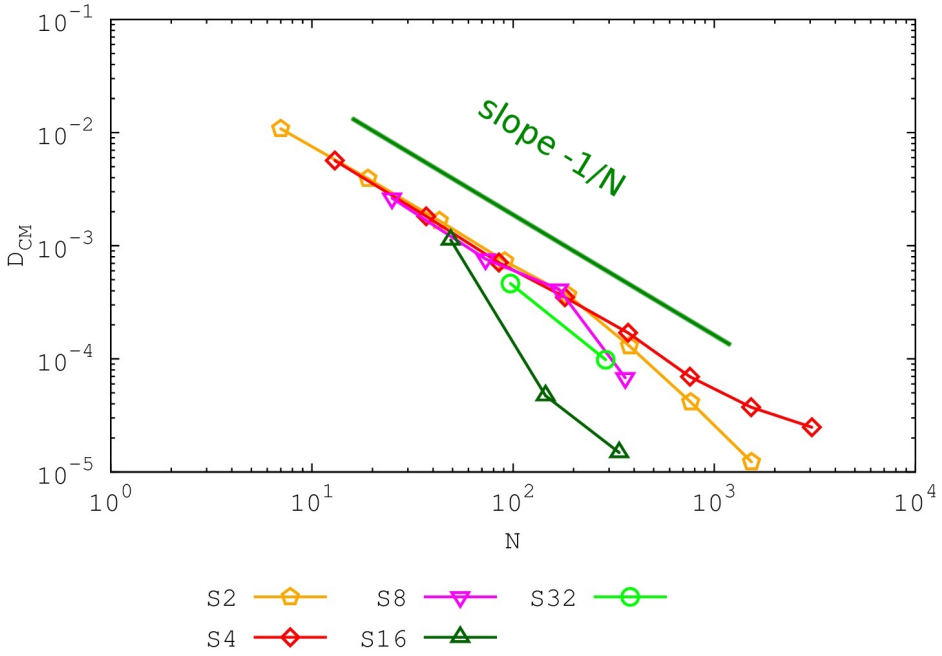

Figure 4.26: Self-diffusion coefficient calculated for the center-of-mass of simulated molecules and it drops down drastically with N.

The branched nature of the molecules results in a range of diffusion timescales that are

dependent on the architecture. Just the presence of the branching points results in a decrease of local mobility. Obviously, a molecule as a whole is always less mobile then certain parts of it. But if we will compare all beads contained in a molecule and compare its behavior to the branching points only we can see that the latter ones are less mobile Fig. 4.27. Since for each branching bead there are three springs attached to it that are pulling it into different directions so its movements are constrained in comparison to linear part of chains.

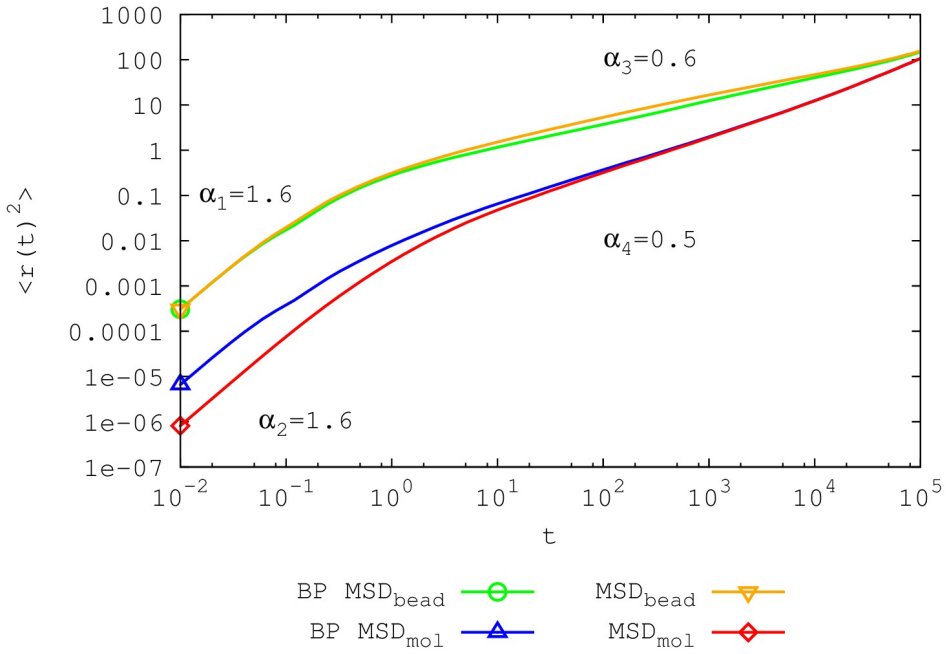

Figure 4.27: Comparison of mean square displacements for different sets of particles for one type of molecule ($S4G4$). The green line follows the movements of the individual branching points, blue center of mass of them, orange indicates MSD of all molecules separately and red center of mass of a molecule as a whole. For the most of the time branching points move slower then other particles. Whole molecules move slower then the individual beads or part of the molecule, but in the long time limit, the monomers have of course to follow the center-of-mass behavior.

4.4.2 Shear relaxation function

Equilibrium approach to calculate viscosity. There is a connection established by the statistical-mechanical theory between the microscopic time-correlation fluctuations and macroscopic coefficients. Such deviation from the equilibrium state can by caused bu the externally imposed perturbation or naturally occurring fluctuations [9, 11, 148]. The essence of that theorem is the fact that one can determine the transport properties of an investigated system from the fluctuations around the equilibrium state. The shear

relaxation function can be expressed as [20, 149]

$$G(t) = \frac{1}{k_B T V} \langle \sigma_{xy}(t) \sigma_{xy}(0) \rangle \tag{4.4.4}$$

and was already discussed in Sec. 2.3.3 with $\sigma_{\alpha\beta}$ being an element of a stress tensor. For better statistical accuracy we have average over additional components of the stress tensor [150].

Since thermal motion of the beads provoke internal stresses that relax with time, with $G(t)$ defined in such a way we can probe the viscoelastic properties of the whole system. A liquid's shear relaxation function and viscosity are related by

$$\eta = \int_0^t G(t')dt' \tag{4.4.5}$$

where η is the shear viscosity, t stays for the last calculated timestep. In many applications of rheology, measuring shear modulus if essential for fundamental understanding of the flow and the performance of the system and further controlling the flow properties like drag reduction. Calculation of $G(t)$ were performed for all simulated samples Fig.4.28 and integrated out to obtain a viscosity η. Stress components were written down every 10 timesteps as in the case of the Gaussian stars for trajectories of 10^6 timesteps in total. As we can see $\eta(t)$ does not reach an expected plateau and the data is not systematic, i.e. the noises are still too high. Sampling was not frequent enough and the trajectory length was too short. It is quite of a computational challenge to increase those two values. For this reason in the next chapter we will try to calculate the viscosity by using a different method.

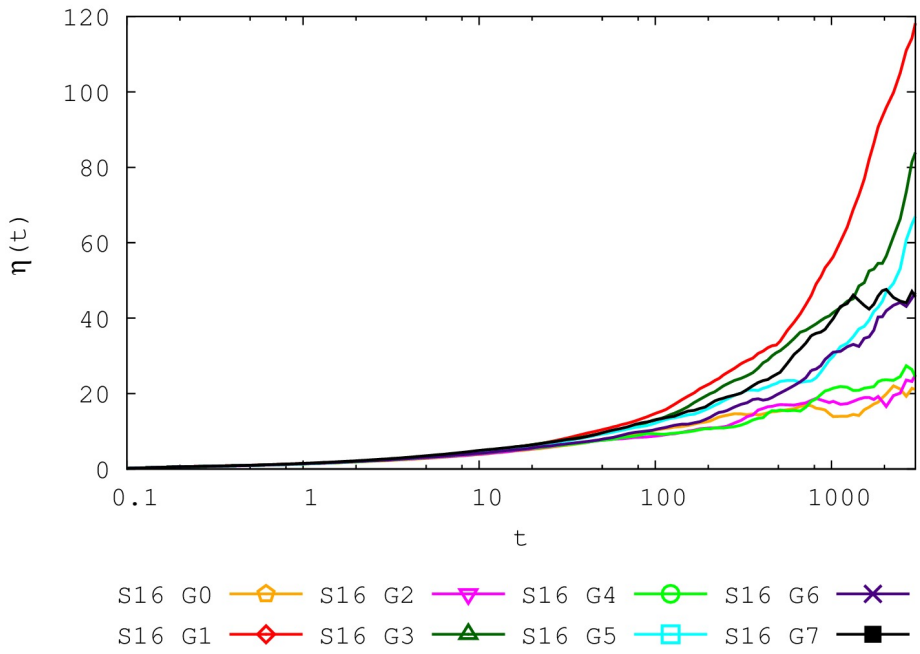

Figure 4.28: Shear relaxation modulus for the samples with $S = 16$ and growing generation. Not systematic shift of the $G(t)$ plateau can suggest large noises in the system disturbing the calculations.

Calculation of the viscosity from molecular dynamics simulations using equilibrium methods suffers significant difficulties due to the small signal in comparison with the background noise. Expression that are relating the fluctuations of off-diagonal elements of the pressure tensor with the viscosity are exact only in the infinite time limit and infinite box length [11], which means extrapolating to the zero frequency ($\omega \to 0$) and zero wave vector ($k \to 0$) [151] (thermodynamic limit). In simulations terms it means that time needed for simulations is large and sampling frequency has to be very high.

4.4.3 Shear viscosity (out-of-equilibrium)

Non-equilibrium approach to computing viscosity. It is the non-equilibrium MD (NEMD) approach that can avoid some of the computational costs by generating a signal significantly larger then the background noise. The method used for further calculations was introduced by Müller-Plathe [151, 152]. The idea of this method is to impose an exactly known momentum flux and calculate rising shear rate or velocity profile which is opposite to standard computational methods where momentum flux appears as an effect of the imposed shear rate. For this reason this method is often called reversed non-equilibrium (RNEMD) method. The RNEMD box is divided into slabs (in performed simulations 20 of them) as seen on Fig. 4.29. The heat flux is created by exchanging velocities of particles of opposing slabs by picking ones with closely matching the absolute

value but opposing directions of momentum. As a result box is divided into "hot" and "cold" slabs and the gradient of velocity is created as seen on Fig. 4.30. Since all the beads have the same mass, total linear momentum and kinetic energy are conserved and no additional thermostat is needed. Such momentum exchange process leads eventually to a steady-state velocity (temperature) gradient. It is the swap frequency that determines the total imposed flux of the system that is given by

$$j_{xz}(p_x) = \frac{p_{tot}}{2tL_xL_y} \tag{4.4.6}$$

where $p_{tot} = \sum(p_{x,n_c} - p_{x,n_1})$ is the total exchanged momentum between slabs, L_x and L_y are the lengths of the simulation box, t states for time.
Viscosity acts as a proportionality coefficient between the momentum flux and the shear rate

$$\eta = \frac{p_{tot}}{\dot{\gamma}}. \tag{4.4.7}$$

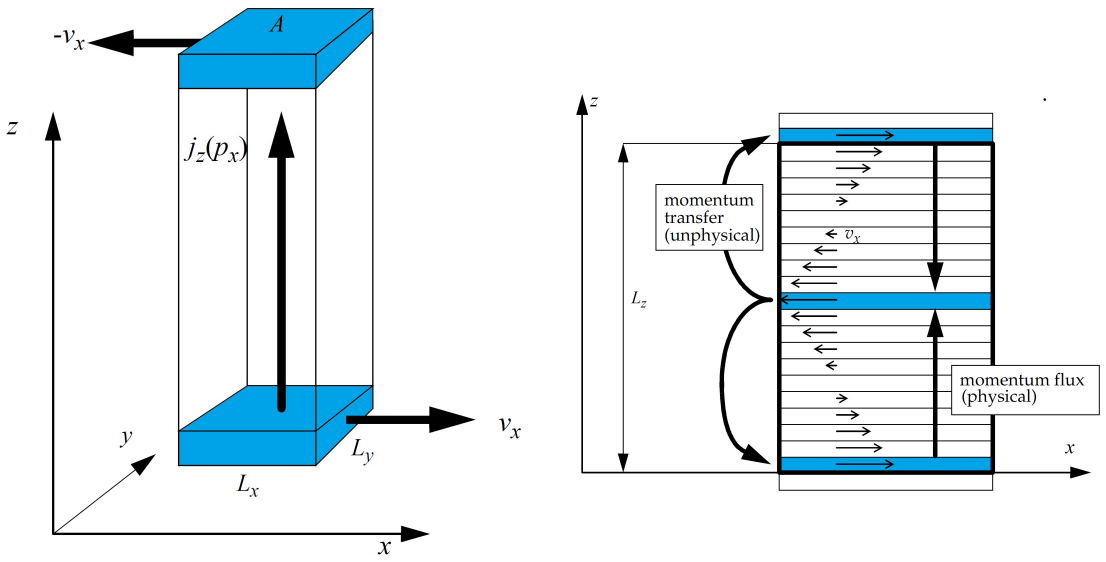

Figure 4.29: RNEMD principles. The box is divided into layers. Unphysical momentum transfer is provoked by a momentum exchange between particles in different layers. As a result physical momentum transfer appears that works against the created velocity gradient. Figures based on those from the article [151].

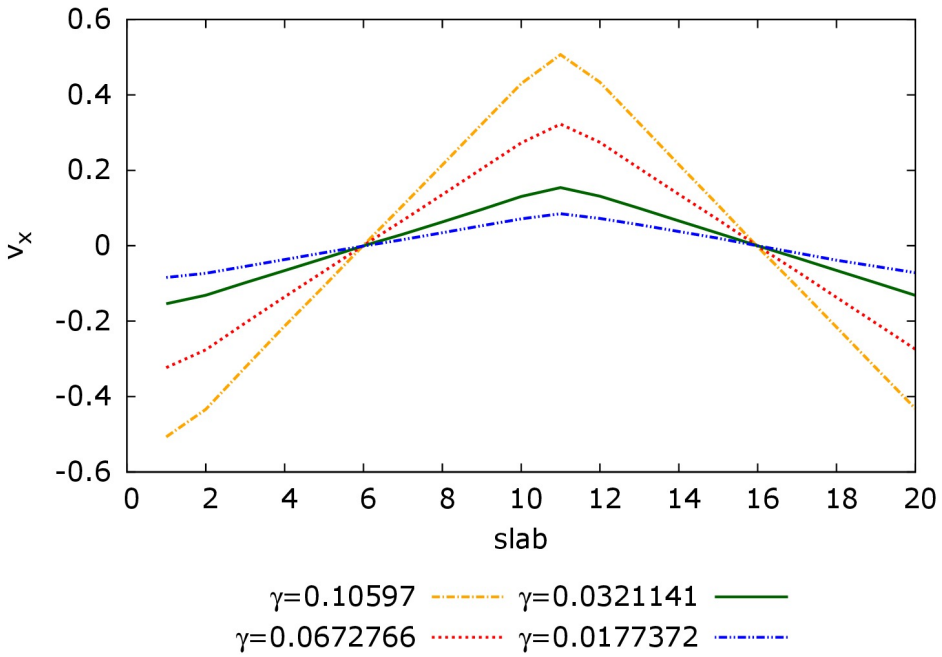

Figure 4.30: Final velocity gradient in the z direction for the samples $S = 8$, $G = 0, 1, 2, 3$. For sufficiently small shear rate $\dot{\gamma}$ (average of the unsigned slopes of v_x versus z) the velocity gradient is linear.

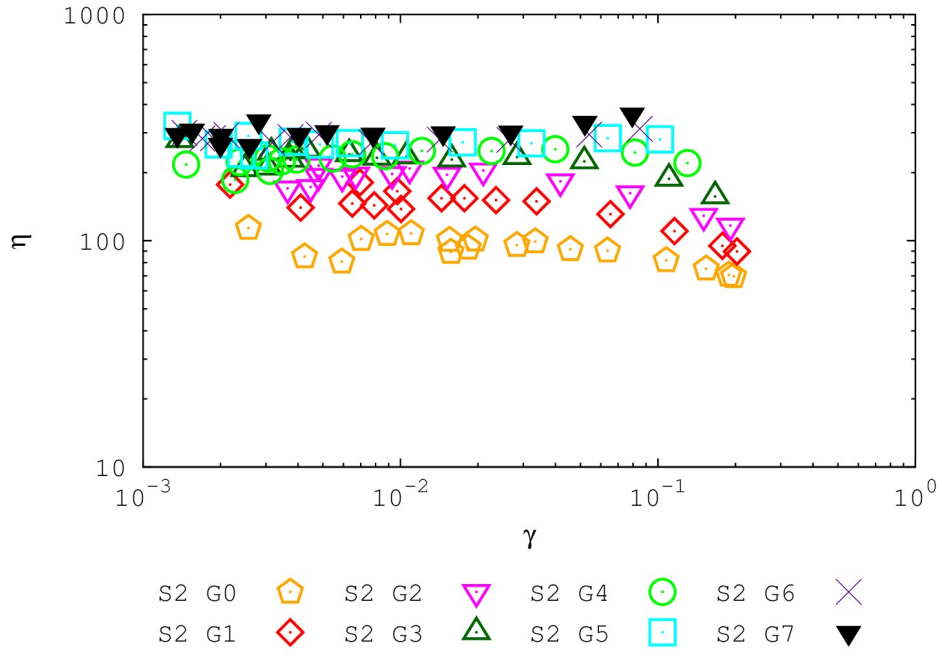

Figure 4.31: Typical flow curve showing the shear viscosity $\eta(\dot{\gamma})$ plotted as a function of shear rate $\dot{\gamma}$ for different systems with $S = 2$. One can see an increase of η with generations G (mass grow). The shear viscosity exhibits constant value η that tends to zero shear viscosity η_0 for small $\dot{\gamma}$.

As the generation grows, the flow curves changes for higher values of viscosity η, as may be seen on Fig. 4.31. This is a specific feature of dendritic-type molecules [153].

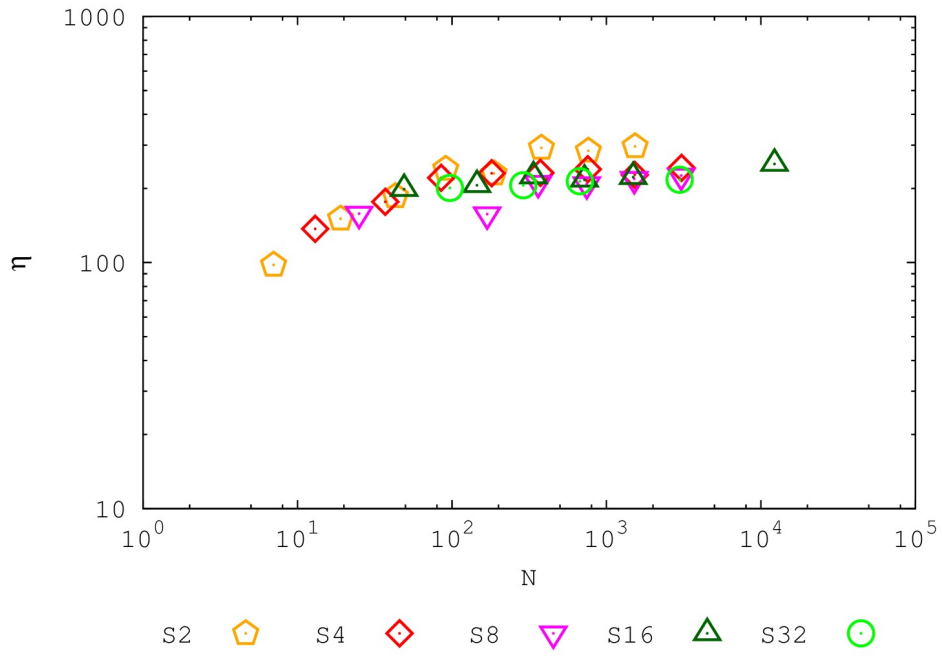

Figure 4.32: Zero shear viscosity η_0 plotted for all simulated systems as a function of mass. The mass dependence becomes surprisingly small.

For linear polymers zero-shear viscosity η_0 is related to the molecular weight N, by the Mark-Houwink Equation

$$\eta_0 = KM^{\alpha} \tag{4.4.8}$$

where η_0 is a Staudinger index (intrinsic viscosity), K is a system dependent constant, M states for molecular mass and α is an index which directly depend on the shape of the dendrimer ($0 \leq \alpha \leq 2$) [153, 154]. In the case of dendritic molecules this law is apparently broken. To the very core of the matter, viscosity arises because of the inter-molecular interactions within a fluid [155]. Owing to the lack of chain entanglement that play a role of the physical bonds, starburst dendrimers, despite their high molecular weights, are not tough materials. What we could observe in our simulation, is that at certain molecular mass η_0 reaches plateau despite of the molecule type (Fig. 4.32). Actually most of the experimental [50, 156, 157] and simulation [34, 36, 50] results predicts a maximum in the intrinsic viscosity with increasing molecular weight. Even though this is not what we can see, one can expect such behavior for higher generation numbers and probably longer simulation times, what would be consistent with our previous results. On the one hand molecule weight grows with generation what leads to viscosity growth. Additionally the amount of arms able to penetrate neighboring molecules increases which slows down the motion as well. On the other hand molecules gets more compact, interaction with nearby

chains are less intense and as a consequence viscosity decreases.

4.5 Conclusion

In this Chapter we have described a behavior of a melt of starburst dendrimers. This time (contrary to the previous Chapter 3) our approach takes into account not only the connectivity but also purely repulsive interactions imitating excluded volume effects.
Starburst dendrimers are monodisperse polymers that go through conformational metamorphosis with increasing generation number G and spacer length S. At high generation number G they adopt a compact, well defined three-dimensional shape. What more, as shown in Sec. 4.3, the total density profile of starburst dendrimers is found to have a strong depletion close to the root monomer. One possible explanation for this effect is that bonds close to the root monomer are strongly stretched due to the huge mass of the dendrimer arms they must tether to the root.
As shown in Sec. 4.4, the diffusion coefficient decreases inversely with mass for most of the investigated systems. Interestingly, a strong slowing down of the diffusion is observed with increasing spacer length. The latter effect is expected due to the increasing interpenetration of the dendrimers which makes topological constrains and the ensuing reptation-like dynamics more relevant. Unfortunately, due to insufficient statistics it was yet not possible to determine the zero-shear viscosity η_0 by integrating the shear-stress relaxation modulus $G(t)$.
Further attempt to measure shear viscosity, this time using NEMD method, shows that there is no simple relation between the zero shear viscosity η_0 and mass N. Presented data reach a plateau for all values of mass despite of the architectural differences. We expect that nonmonotonous behavior could appear as it is visible in experiments [50, 157].

Chapter 5

Conclusion

5.1 Summary

Over the last three years (since october 2010) I had the opportunity to study mainly numerically by means of computer simulations of strongly simplified coarse-grained models various static and dynamical problems of dense colloidal and polymeric systems. While attempting within the frame of the IRTG Soft Matter to bring together the interests of the research groups in Freiburg (Prof. A. Blumen, Prof. C. Friedrich), in Metz (Prof. H. Xu) and at the ICS in Strasbourg (Prof. J. Baschnagel), my studies have let already to several publications [1, 2, 3, 4, 5, 6, 7, 53] and one submitted manuscript [54]. Several of these papers [1, 3, 4, 5, 6, 7, 53] have been co-authored by Prof. Xu from Metz, one paper [4] by the fellow IRTG PhD students C. Gillig and J. Helfferich from Freiburg. Two papers [57, 56] are currently under preparation. In the presented PhD manuscript I have focused on two research areas which have been of particular concern to me:

(i) the determination of linear elastic properties in dense soft matter systems including colloidal glasses [4, 5, 6, 7]. As demonstrated in Chapter 2, *impulsive corrections* to the standard Born terms of the stress fluctuation formalism are required for systems sampled using *truncated* (and shifted) pair potentials [7]. As discussed briefly in Sec. 2.4 and more in detail in Ref. [6], this finding should be of particular importance for the precise determination of the shear modulus G at the solid/glass-liquid transition which is important to distinguish between the different theoretical scenarios proposed [16, 87, 88, 89, 158].

(ii) the characterization of hyperbranched polymer stars revisiting first some properties of systems with Gaussian chain statistics [54] and presenting then my much more extensive (yet unpublished) molecular dynamics simulations of melts of regular dendrimers [57]. The latter study has revealed two unexpected and not completely understood striking findings. As shown in Sec. 4.3, the total density profile of the dendrimers is found to have a *strong depletion* close to the root monomer of the

star, i.e. at variance to various statements made in the literature (mainly in context of dilute dendrimers) the density profile is strongly non-monotonous. As shown in Sec. 4.4, for large generation numbers the zero-shear viscosity η_0, obtained using an out-of-equilibrium method [62], becomes essentially independent of mass N. This finding might be due to the fact the stars adopt increasingly compact configurations.

5.2 Perspectives

Looking beyond my presented studies into yet on-going and possible immediate future work, I would like to take the opportunity to sketch several avenues which appear promising to me:

- In an attempt to understand the strong density depletion in dendrimer melts we are currently computing *dilute* regular dendrimers increasing gradually the excluded volume interaction ϵ of the lattice Hamiltonian, Eq. (3.2.1).[1] As already noted in Chapter 3.6, these dendrimers become increasingly compact ($d_f \to d$) with increasing generation number G and excluded volume ϵ. Confirming older work [36, 72], a weak local density minimum at the core is clearly observed. The systematic scaling of the effect still needs to be characterized and understood. Theoretical guidance is clearly warranted here.

- Using the same Monte Carlo approach it should be rewarding to sample dendrimer melts as a function of ϵ in analogy to the recent study of linear chain melts [1]. A question is then of whether indeed the depletion effect becomes more pronounced as for dilute chains albeit the overall pressure must increase. It will be also of some interest to characterize the mean-square displacement of the star center-of-mass or, even better, the associated displacement correlation function [1]. As for the center-of-mass motion of linear polymer melts [1, 2, 24, 159], strong deviations from the Rouse scaling are to be expected albeit reptational effects must be irrelevant at, say, $\epsilon = 1$.

- To understand better the *local* thermodynamic properties of dendrimer melts such as the pressure tensor and its fluctuations or the Born (affine) contributions in spherical coordinates around each root monomer, the *lattice* Monte Carlo approach is not suitable, however, and one should use the *off-lattice* bead-spring model discussed in Chapter 4 albeit it is much slower to compute.[2] It is of some interest to see whether it is possible to determine the (negative) surface tension as a function of r from

[1] One may simulate θ-solvent conditions imposing $E = \epsilon/6 \sum_{\underline{r}} n(\underline{r}) \; (n(\underline{r}) - 1) \; (n(\underline{r}) - 2)$.

[2] From the density profiles of free monomers added to the melt on may obtain an estimate of the chemical potential as a function of r.

the stress-fluctuation formalism and whether the (negative) Laplace pressure [19] is consistent with the gradient of the radial pressure component.

- The sampling times presented for the equilibrium dynamics in Sec. 4.4 were clearly insufficient to determine for the larger dendrimers the diffusion coefficients $D(N)$ and the terminal relaxation time $\tau(N)$ of the samples. This appears to me a natural and feasible task for the near future. Also the estimate of the viscosity using the Green-Kubo equilibrium formula should be improved by writing down the stress-tensors for every MD sweep and taking advantage of longer trajectories. This is important to check the viscosity for all the samples possible, specially for high generation values, where compactness could diminish measured viscosity values.

Bibliography

[1] J. P. Wittmer, A. Cavallo, H. Xu, J. E. Zabel, P. Polińska, N. Schulmann, H. Meyer, J. Farago, A. Johner, S. P. Obukhov, and J. Baschnagel. Scale-free static and dynamical correlations in melts of monodisperse and flory-distributed homopolymers. *Journal of Statistical Physics*, **145**(4):1017–1126, 2011.

[2] J. P. Wittmer, P. Polińska, H. Meyer, J. Farago, A. Johner, J. Baschnagel, and A. Cavallo. Scale-free center-of-mass displacement correlations in polymer melts without topological constraints and momentum conservation: A bond-fluctuation model study. *The Journal of Chemical Physics*, **134**(23):234901, 2011.

[3] J. P. Wittmer, N. Schulmann, P. Polińska, and J. Baschnagel. Note: Scale-free center-of-mass displacement correlations in polymer films without topological constraints and momentum conservation. *The Journal of Chemical Physics*, **135**(18):86101, 2011.

[4] J. P. Wittmer, H. Xu, P. Polińska, C. Gillig, J. Helfferich, F. Weysser, and J. Baschnagel. Compressibility and pressure correlations in isotropic solids and fluids. *The European Physical Journal E*, **36**(11):1–17, 2013.

[5] J. P. Wittmer, H. Xu, P. Polińska, F. Weysser, and J. Baschnagel. Communication: Pressure fluctuations in isotropic solids and fluids. *The Journal of Chemical Physics*, **138**(19):191101, 2013.

[6] J. P. Wittmer, H. Xu, P. Polińska, F. Weysser, and J. Baschnagel. Shear modulus of simulated glass-forming model systems: Effects of boundary condition, temperature, and sampling time. *The Journal of Chemical Physics*, **138**(12):12A533, 2013.

[7] H. Xu, J. P. Wittmer, P. Polińska, and J. Baschnagel. Impulsive correction to the elastic moduli obtained using the stress-fluctuation formalism in systems with truncated pair potential. *Phys. Rev. E*, **86**:046705, Oct 2012.

[8] T. Witten and P.A. Pincus. *Structured Fluids: Polymers, Colloids, Surfactants*. Oxford University Press, 2004.

[9] P.M. Chaikin and T.C.Lubensky. *Principles of Condensed Matter Physics*. Cambridge, 2000.

[10] J.S. Rowlinson. *Liquids and liquid mixtures*. Butterworths Scientific Publications, 1959.

[11] J. Hansen and I. McDonald. *Theory of Simple Liquids*. Academic, New York, 1986.

[12] Pierre-Gilles de Gennes. *Scaling Concepts in Polymer Physics*. Cornell University Press, 1979.

[13] M. Doi and S.F. Edwards. *The Theory of Polymer Dynamics*. Clarendon Press, 1986.

[14] M. Rubinstein and R. Colby. *Polymer Physics*. Oxford, 2003.

[15] J.S. Higgins and H.C. Bienoît. *Polymers and Neuron Scattering*. Oxford Science Publications, 1994.

[16] W. Götze. *Complex Dynamics of Glass-Forming Liquids: A Mode-Coupling Theory*. Oxford University Press, 2009.

[17] Herbert B. Callen. *Thermodynamics and an Introduction to Thermostatistics*. Wiley, 1985.

[18] L.D. Landau and I.M. Lifshitz. *Statistical Physics*. Pergamon Press, 1959.

[19] L.D. Landau and I.M. Lifshitz. *Theory of Elasticity*. Pergamon Press, 1959.

[20] M.P. Allen and D.J. Tildesley. *Computer Simulation of Liquids*. Oxford University Press, 1987.

[21] D. Frenkel and B. Smit. *Understanding Molecular Simulation – From Algorithms to Applications*. Academic Press, 2002.

[22] J. Thijssen. *Computational Physics*. Cambridge University Press, 1999.

[23] J. P. Wittmer, H. Meyer, J. Baschnagel, A. Johner, S. Obukhov, L. Mattioni, M. Müller, and A. N. Semenov. Long range bond-bond correlations in dense polymer solutions. *Phyical Review Letters*, **93**:147801, Sep 2004.

[24] J. Farago, H. Meyer, and A. N. Semenov. Anomalous diffusion of a polymer chain in an unentangled melt. *Physical Review Letters*, **107**:178301, 2011.

[25] B. Schnell, H. Meyer, C. Fond, J. P. Wittmer, and J. Baschnagel. Simulated glass-forming polymer melts: Glass transition temperature and elastic constants of the glassy state. *The European Physical Journal E*, **34**(9):1–13, 2011.

[26] H. Wiener. Structural determination of paraffin boiling points. *Journal of the American Chemical Society*, **69**(1):17–20, 1947.

[27] W. Burchard, K. Kajiwara, and D. Nerger. Static and dynamic scattering behavior of regularly branched chains: A model of soft-sphere microgels. *Journal of Polymer Science Part B: Polymer Physics*, **20**:157, 1982.

[28] J. Dewald M. Hall G. Kallos S. Martin J. Roeck J. Ryder D. A Tomalia, H. Baker and P. Smith. A new class of polymers: Starburst-dendritic macromolecules. *Polymer Journal*, **17**:117–132, 1985.

[29] P. G. de Gennes et H. Hervet. Statistics of starburst polymers. *Journal de Physique Lettres*, **44**(9):351–360, 1983.

[30] O.V. Borisov, E.B. Zhulina, and T.M. Birshtein. Persistence length of dendritic molecular brushes. *ACS Macro Letters*, **1**:1166, 2012.

[31] O.V. Rud, A.A. Polotsky, T. Gillich, O.V. Borisov, F.A.M. Leermakers, M. Textor, and T.M. Birshtein. Dendritic spherical polymer brushes: Theory and self-consistent field modeling. *Macromolecules*, **46**:4651, 2013.

[32] A. Gurtovenko and A. Blumen. Generalized gaussian structures: Models for polymer systems with complextopologies. **182**:171–282, 2005.

[33] R. La Ferla. Conformations and dynamics of dendrimers and cascade macromolecules. *The Journal of Chemical Physics*, **106**(2):688–700, 1997.

[34] R. L. Lescanec and M. Muthukumar. Configurational characteristics and scaling behavior of starburst molecules: a computational study. *Macromolecules*, **23**(8):2280–2288, 1990.

[35] M. L. Mansfield. Monte Carlo Studies of Dendrimers. Additional Results for the Diamond Lattice Model. *Macromolecules*, **33**(21):8043–8049, 2000.

[36] M. Murat and G. S. Grest. Molecular dynamics study of dendrimer molecules in solvents of varying quality. *Macromolecules*, **29**(4):1278–1285, 1996.

[37] O. V. Borisov, E. B. Zhulina, F. A. M. Leermakers, M. Ballauff, and A. H. E. Müller. Conformations and solution properties of star-branched polyelectrolytes. In Axel H. E. Müller and Oleg Borisov, editors, *Self Organized Nanostructures of Amphiphilic Block Copolymers I*, volume **241** of *Advances in Polymer Science*, pages 1–55. Springer Berlin Heidelberg, 2011.

[38] K. Karatasos, D. B. Adolf, and G. R. Davies. Statics and dynamics of model dendrimers as studied by molecular dynamics simulations. *The Journal of Chemical Physics*, **115**(11):5310, 2001.

[39] A. V. Lyulin, G. R. Davies, and D. B. Adolf. Location of Terminal Groups of Dendrimers : Brownian Dynamics Simulation. **33**:6899–6900, 2000.

[40] I. O. Götze and C. N. Likos. Conformations of flexible dendrimers: a simulation study. *Macromolecules*, **36**(21):8189–8197, 2003.

[41] C. J. Hawker and J. M. J.Frechet. Preparation of polymers with controlled molecular architecture. a new convergent approach to dendritic macromolecules. *Journal of the American Chemical Society*, **112**(21):7638–7647, 1990.

[42] J. M. J. Fréchet, S. Aoshima M. R. Leduc M. Henmi, I. Gitsov, and R. B. Grubbs. Self-condensing vinyl polymerization: An approach to dendritic materials. *Science*, **269**:1080–1083, 1995.

[43] A. H. E. Müller, D. Yan, and M. Wulkow. Molecular parameters of hyperbranched polymers made by self-condensing vinyl polymerization. 1. molecular weight distribution. *Macromolecules*, **30**(23):7015–7023, 1997.

[44] A. Morikawa, M. Kakimoto, and Y. Imai. Synthesis and characterization of new polysiloxane starburst polymers. *Macromolecules*, **24**(12):3469–3474, 1991.

[45] R. H. E. Hudson and M. J. Damha. Nucleic acid dendrimers: novel biopolymer structures. *Journal of the American Chemical Society*, **115**(6):2119–2124, 1993.

[46] Y. Rio, G. Accorsi, H. Nierengarten, J. L. Rehspringer, B. Hönerlage, G. Kopitkovas, A. Chugreev, A. Van Dorsselaer, N. Armaroli, and J. F. Nierengarten. Fullerodendrimers with peripheral triethyleneglycol chains: synthesis, mass spectrometric characterization, and photophysical properties. *New Journal of Chemistry*, **26**:1146–1154, 2002.

[47] Ch. Erbacher M. Weber, J. Dennig. Targeted transfection of cells using a biotinylated dendrimer, May 2003.

[48] Hiroyasu Yamaguchi and Akira Harada. Antibody dendrimers. In Ch. A. Schalley and F. Vögtle, editors, *Dendrimers V*, volume **226** of *Topics in Current Chemistry*, pages 237–258. Springer Berlin Heidelberg, 2003.

[49] H. L. Crampton and E. E. Simanek. Dendrimers as drug delivery vehicles: noncovalent interactions of bioactive compounds with dendrimers. *Polymer International*, **56**(4):489–496, 2007.

[50] M. L. Mansfield and L. I. Klushin. Monte Carlo Studies of Dendrimer Macromolecules. *Macromolecules*, **26**:4262–4268, 1993.

[51] N. Likos, M. Schmidt, H. Löwen, M. Ballauff, D. Pötschke, and P. Lindner. Soft interaction between dissolved flexible dendrimers: theory and experiment. *The Journal of Physical Chemistry B*, **34**:2914, 2001.

[52] D. Boris and M. Rubinstein. A self-consistent mean field model of a starburst dendrimer: dense core vs dense shell. *Macromolecules*, **29**(22):7251–7260, 1996.

[53] N. Schulmann, H. Xu, H. Meyer, P. Polińska, J. Baschnagel, and J. P. Wittmer. Strictly two-dimensional self-avoiding walks: Thermodynamic properties revisited. *The European Physical Journal E*, **35**(9):1–16, 2012.

[54] P. Polińska, J. P. Wittmer, and J. Baschnagel. Hyperbranched polymer stars with gaussian statistics revisited. 2013. submitted.

[55] D.P. Landau and K. Binder. *A Guide to Monte Carlo Simulations in Statistical Physics*. Cambridge University Press, Cambridge, 2000.

[56] J. P. Wittmer, A. Johner, P. Polińska, O. Benzerara, H. Meyer, and J. Baschnagel. Long-range spatio-temporal correlations of the displacement field of both incompressible and overdamped liquids: Phenomenological linear response theory and Monte Carlo simulation results. in preparation.

[57] P. Polińska, H. Meyer, and J. P. Wittmer. Non-monotonous density profile of starburst dendrimer melts. 2014. in preparation.

[58] M. Filali, M.J. Ouazzani, E. Michel, R. Aznar, G. Porte, and J. Appell. Robust phase behavior of model transient networks. *The Journal Of Physical Chemistry B*, **105**:10528, 2001.

[59] A. Zilman, J. Kieffer, F. Molino, G. Porte, and S. A. Safran. Entropic phase separation in polymer-microemulsion networks. *Physical Review Letters*, **91**:015901, 2003.

[60] L. Ramos and C. Ligoure. Structure of a new type of transient network: entangled wormlike micelles bridged by telechelic polymers. *Macromolecules*, **40**:1248, 2007.

[61] C. Tonhauser, D. Wilms, Y. Korth, H. Frey, and Ch. Friedrich. Entanglement transition in hyperbranched polyether-polyols. *Macromolecular Rapid Communications*, **31**:2127, 2010.

[62] F. Müller-Plathe. Reversing the perturbation in nonequilibrium molecular dynamics: An easy way to calculate the shear viscosity of fluids. *Physical Review E*, **59**(5), 1999.

[63] W. Kob and H.C. Andersen. Testing mode-coupling theory for a supercooled binary lennard-jones mixture. ii. intermediate scattering function and dynamic susceptibility. *Physical Review E*, **52**:4134, 1995.

[64] A. Tanguy, J. P. Wittmer, F. Leonforte, and J. L. Barrat. Continuum limit of amorphous elastic bodies: A finite-size study of low-frequency harmonic vibrations. *Physical Review B*, **66**:174205, 2002.

[65] M. Tsamados, A. Tanguy, C. Goldenberg, and J. L. Barrat. Local elasticity map and plasticity in a model lennard-jones glass. *Physical Review E*, **80**:026112, 2009.

[66] H. Meyer and J. P. Wittmer N. Schulmann andJ. E. Zabel. The structure factor of dense two-dimensional polymer solutions. *Computer Physics Communications*, **182**:1949, 2011.

[67] T. Witten and L. Sander. Diffusion-limited aggregation, a kinetic critical phenomenon. *Physical Review Letters*, **47**:1400, 1981.

[68] P. Meakin, A. Conigilio, H. E. Stanley, and T. Witten. Scaling properties for the surfaces of fractal and nonfractal objects: An infinite hierarchy of critical exponents. *Physical Review A*, **34**:3325, 1986.

[69] J.-F. Gouyet. *Physique et structures fractales*. Masson, 1993.

[70] T. Kramer S. Godoya and M. Moshinsky. Transient phenomena in quantum mechanics. *Revista Mexicana de Fisica S*, **52**:1, 2006.

[71] G.S. Grest and K. Kremer. Molecular dynamic simulation for polymers in the presence of a heat bath. *Physical Review A*, **33**(5), 1986.

[72] J. S. Kłos and J. U. Sommer. Properties of dendrimers with flexible spacer-chains: A Monte Carlo study. *Macromolecules*, **42**:4876, 2009.

[73] D. A. Lenz, B. M. Mladek, Ch. N. Likos, G. Kahl, and R. Blaak. Monomer-resolved simulations of cluster-forming dendrimers. *The Journal of Physical Chemistry B*, **115**:7218, 2011.

[74] M. Abramowitz and I.A. Stegun. *Handbook of Mathematical Functions*. Dover New York, 1964.

[75] H. Ehrenreich, F. Seitz, and D. Turnbull. *Solid State Physics: Advances in Research and Applications*. Academic Press, 1970.

[76] D. R. Squire, A. C. Holt, and W. G. Hoover. Isothermal elastic constants for argon. theory and Monte Carlo calculations. *Physica*, **42**:388, 1969.

[77] J.R. Ray and A. Rahman. Statistical ensembles and molecular dynamics studies of anisotropic solids. *The Journal of Chemical Physics*, **80**:4423, 1984.

[78] J.R. Ray. Elastic constants and statistical ensembles in molecular dynamics. *Computer Physics Reports*, **8**:109, 1988.

[79] J. F. Lutsko. Generalized expressions for the calculation of elastic constants by computer simulation. *Journal of Applied Physics*, **8**:1152, 1988.

[80] J. F. Lutsko. Generalized expressions for the calculation of elastic constants by computer simulation. *Journal of Applied Physics*, **65**:2991, 1989.

[81] C. Maloney and A. Lemaître. Universal breakdown of elasticity at the onset of material failure. *Physical Review Letters*, **93**:195501, 2004.

[82] K. Yoshimoto, T. Jain, K. van Workum, P. Nealey, and J. de Pablo. Mechanical heterogeneities in model polymer glasses at small length scales. *Physical Review Letters*, **93**:175501, 2004.

[83] K. Yoshimoto, B. Papakonstantopoulos, J. Lutsko, and J. de Pablo. Statistical calculation of elastic moduli for atomistic models. *Physical Review B*, **71**:184108, 2005.

[84] M. Ferrario, G. Ciccotti, and K. Binder. *Computer Simulations in Condensed Matter: From Materials to Chemical Biology. Volume 1*. Springer, 2006.

[85] S. Ulrich, X. Mao, P. Goldbart, and A. Zippelius. Elasticity of highly cross-linked random networks. *EPL (Europhysics Letters)*, **76**:677, 2006.

[86] F. Zamponi, G. Parisi. Mean-field theory of hard sphere glasses and jamming. *Reviews of Modern Physics*, **82**:789, 2010.

[87] H. Yoshino and M. Mézard. Emergence of rigidity at the structural glass transition: A first-principles computation. *Physical Review Letters*, **105**:015504, 2010.

[88] G. Szamel and E. Flenner. Emergence of long-range correlations and rigidity at the dynamic glass transition. *Physical Review Letters*, **107**:105505, 2011.

[89] H. Yoshino. Replica theory of the rigidity of structural glasses. *The Journal of Chemical Physics*, **136**:214108, 2012.

[90] E. del Gado and W. Kob. Network formation and relaxation dynamics in a new model for colloidal gelation. *Journal of Non-Newtonian Fluid Mechanics*, **149**:28, 2008.

[91] S. Toxvaerd and J. C. Dyre. Communication: Shifted forces in molecular dynamics. *The Journal of Chemical Physics*, **134**:081102, 2011.

[92] F. Birch. The effect of pressure upon the elastic parameters of isotropic solids, according to murnaghan's theory of finite strain. *Journal Of Applied Physics*, **9**:279, 1938.

[93] B. H. Zimm and W. H. Stockmayer. The dimensions of chain molecules containing branches and rings. *The Journal of Chemical Physics*, **17**(12):1301–1314, 1949.

[94] B. Hammouda. Structure factor for starburst dendrimers. *Journal of Polymer Science Part B: Polymer Physics*, **30**:1387, 1992.

[95] P. Biswas and B. Cherayil. *The Journal of Chemical Physysics*, **100**:3201, 2001.

[96] S. Obukhov, M. Rubinstein, and T. Duke. Dynamics of a ring polymer in a gel. *Physical Review Letters*, **73**:1263, 1994.

[97] A. Blumen, A. Jurjiu, T. Koslowski, and Ch. von Ferber. Dynamics of vicsek fractals, models for hyperbranched polymers. *Physical Review E*, **67**:061103, 2003.

[98] A. Blumen, Ch. von Ferber, A. Jurjiu, and T. Koslowski. Generalized vicsek fractals: regular hyperbranched polymers. *Macromolecules*, **37**:638, 2003.

[99] M. Dolgushev and A. Blumen. Dynamics of semiflexible chains, stars, and dendrimers. *Macromolecules*, **42**:5378, 2009.

[100] M. Dolgushev and A. Blumen. *Macromolecules*, **131**:044905, 2009.

[101] M. Dolgushev and A. Blumen. *Macromolecules*, **132**:124905, 2010.

[102] M. Dolgushev, A. Blumen, and G. Berezovska. Branched semiflexible polymers: Theoretical and simulation aspects. *Macromolecular Theory and Simulations*, **20**:621, 2011.

[103] F. Fürstenberg, M. Dolgushev, and A. Blumen. Analytical model for the dynamics of semiflexible dendritic polymers. *J. Chem. Phys.*, **136**:154904, 2012.

[104] A. Kumar and P. Biswas. Dynamics of semiflexible dendrimers in dilute solutions. *Macromolecules*, **43**:7378, 2010.

[105] A. Kumar and P. Biswas. *The Journal of Chemical Physics*, **134**:214901, 2011.

[106] A. Kumar and P. Biswas. *The Journal of Chemical Physics*, **137**:124903, 2012.

[107] B. Duplantier. Statistical mechanics of polymer networks of any topology. *Journal of Statistical Physics*, **54**:581, 1989.

[108] B. Duplantier. Tricritical polymer chains in or below three dimensions. *EPL (Europhysics Letters)*, **1**:491, 1986.

[109] K. Biswas and A. Blumen. *The Journal Chemical Physics*, **114**:2430, 2001.

[110] B. Wu, Y. Lin, Z. Zhang, and G. Chen. Trapping in dendrimers and regular hyperbranched polymers. *The Journal of Chemical Physics*, **137**:044903, 2012.

[111] F. Fürstenberg, M. Dolgushev, and A. Blumen. *The Journal of Chemical Physics*, **138**:034904, 2013.

[112] B. Mandelbrot. *The Fractal Geometry of Nature*. W.H. Freeman, 1982.

[113] W. Burchard. Static and dynamic light scattering from branched polymers and biopolymers. In *Light Scattering from Polymers*, volume 48 of *Advances in Polymer Science*, pages 1–124. Springer Berlin Heidelberg, 1983.

[114] K. Huber, S. Bantle, W. Burchard, and L. Fetters. Semidilute solutions of star branched polystyrene: a light and neutron scattering study. *Macromolecules*, **19**:1404, 1986.

[115] J. P. Wittmer, H. Meyer, A. Johner, S. P. Obukhov, and J. Baschnagel. *The Journal of Chemical Phycis.*, **139**:217101, 2013.

[116] E. Buhleier, W. Wehner, and F. Vögtle. "Cascade"- and "Nonskid-Chain-like" Syntheses of Molecular Cavity Topologies. *Synthesis-stuttgart*, **1978**:155–158, 1978.

[117] J. M. J. Fréchet, C. J. Hawker, and K. L. Wooley. The convergent route to globular dendritic macromolecules: A versatile approach to precisely functionauzed three-dimensional polymers and novel block copolymers. *Journal of Macromolecular Science, Part A*, **31**(11):1627–1645, 1994.

[118] Jean M. J. Fréchet and Donald A. Tomalia. *Dendrimers and Other Dendritic Polymers*. Wiley, 2001.

[119] M. Kenward, F. Tessier, Y. Tatek, Y. Gratton, S. Guillouzic, and G. W. Slatera. Molecular dynamics simulations of polymers in microenvironments. In *Proceedings of the 17th International Symposium on High Performance Computing Systems and Applications and OSCAR Symposium*. NRC Research Press, 2003.

[120] R. Kimmich. *Principles of Soft-Matter Dynamics: Basic Theories, Non-invasive Methods, Mesoscopic Aspects*. Springer, 2012.

[121] Christian Holm and Kurt Kremer. *Advanced Computer Simulation Approaches for Soft Matter Sciences I*. Springer, 2005.

[122] J. C. Phillips, R. Braun, W. Wang, J. Gumbart, E. Tajkhorshid, E. Villa, Ch. Chipot, R. D. Skeel, L. Kalé, and K. Schulten. Scalable molecular dynamics with namd. *Journal of Computational Chemistry*, **26**(16):1781–1802, 2005.

[123] William A. Goddard III, Donald Brenner, Sergey Edward Lyshevski, and Gerald J Iafrate. *Handbook of Nanoscience, Engineering, and Technology*. CRC Press, 2012.

[124] http://codeblue.umich.edu/hoomd-blue/.

[125] http://lammps.sandia.gov/.

[126] R. Petrenko and J. Meller. *Molecular Dynamics*. John Wiley Sons, Ltd, 2001.

[127] http://classes.yale.edu/fractals/FracTrees/welcome.html.

[128] G. Evmenenko, B. J. Bauer, R. Kleppinger, B. Forier, W. Dehaen, E. J. Amis, N. Mischenko, and H. Reynaers. The influence of molecular architecture and solvent type on the size and structure of poly(benzyl ether) dendrimers by sans. *Macromolecular Chemistry and Physics*, **202**(6):891–899, 2001.

[129] T. J. Prosa, B. J. Bauer, E. J. Amis, D. A. Tomalia, and R. Scherrenberg. A saxs study of the internal structure of dendritic polymer systems. *Journal of Polymer Science Part B: Polymer Physics*, **35**(17):2913–2924, 1997.

[130] R. Scherrenberg, B. Coussens, P. van Vliet, G. Edouard, J. Brackman, E. de Brabander, and K. Mortensen. The molecular characteristics of poly(propyleneimine) dendrimers as studied with small-angle neutron scattering, viscosimetry, and molecular dynamics. *Macromolecules*, **31**(2):456–461, 1998.

[131] L. Cavallo and F. Fraternali. A molecular dynamics study of the first five generations of poly(propylene imine) dendrimers modified with n-tboc-l-phenylalanine. *Chemistry A European Journal*, **4**(5), 1998.

[132] E. J. Wallace, D. M. A. Buzza, and D. J. Read. Monte Carlo simulation scheme for dendrimers satisfying detailed balance. *Macromolecules*, **34**(20):7140–7146, 2001.

[133] J.H. Conway and N.J.A. Sloane. *Spheres Packings, Lattices and Groups*. New York: Springer-Verlag, 1999.

[134] N. Sensei and K.J. Wilkinson. *Biophysical Chemistry of Fractal Structures and Processes in Environmental Systems*. John Wiley Sons, 2008.

[135] G. Giupponi and D. M. A. Buzza. A Monte Carlo simulation scheme for nonideal dendrimers satisfying detailed balance. *Macromolecules*, **35**(26):9799–9812, 2002.

[136] Jens Als-Nielsen and Des McMorrow. *Elements of Modern X-ray Physics*. John Wiley Sons, 2011.

[137] S. Rathgeber, M. Monkenbusch, M. Kreitschmann, V. Urban, and A. Brulet. Dynamics of star-burst dendrimers in solution in relation to their structural properties. *The Journal of Chemical Physics*, **117**(8):4047–4062, 2002.

[138] T. J. Prosa, B. J. Bauer, and E. J. Amis. From stars to spheres: A saxs analysis of dilute dendrimer solutions. *Macromolecules*, **34**(14):4897–4906, 2001.

[139] G. Nisato, R. Ivkov, and E. J. Amis. Size invariance of polyelectrolyte dendrimers. *Macromolecules*, **33**(11):4172–4176, 2000.

[140] T. Pakula. Static and dynamic properties of computer simulated melts of multiarm polymer stars. *Computational and Theoretical Polymer Science*, **8**(12):21 – 30, 1998.

[141] C.H. Wang. *Spectroscopy of Condensed Media*. Elsevier, 1985.

[142] Ulrich Rössler. *Solid State Theory: An Introduction*. Springer, 2009.

[143] T. P. Lodge and M. Muthukumar. Physical chemistry of polymers: entropy, interactions, and dynamics. *The Journal of Physical Chemistry*, **100**(31):13275–13292, 1996.

[144] E. G. Timoshenko, Y. A. Kuznetsov, and R. Connolly. Conformations of dendrimers in dilute solution. *The Journal of Chemical Physics*, **117**(19):9050, 2002.

[145] R. Scherrenberg, B. Coussens, P. van Vliet, , G. Edouard, J. Brackman, E. de Brabander, and K. Mortensen. The Molecular Characteristics of Poly(propyleneimine) Dendrimers As Studied with Small-Angle Neutron Scattering, Viscosimetry, and Molecular Dynamics. *Macromolecules*, **31**(2):456–461, 1998.

[146] A. V. Lyulin, G. R. Davies, and D. B. Adolf. Brownian dynamics simulations of dendrimers under shear flow. *Macromolecules*, **33**(9):3294–3304, 2000.

[147] Z. Y. Chen and S. M. Cui. Monte Carlo simulations of star-burst dendrimers. *Macromolecular Theory and Simulations*, **29**(24):7943–7952, 1996.

[148] James E. Mark. *Physical properties of polymers handbook*. Springer, 2006.

[149] U. Balucani. *Dynamics of the Liquid State*. Oxford University Press, 1995.

[150] P. J. Daivis and D. J. Evans. Comparison of constant pressure and constant volume nonequilibrium simulations of sheared model decane. *The Journal of Chemical Physics*, **100**(1):541–547, 1994.

[151] C. M. Tenney, M. Craig, and E. J. Maginn. Limitations and recommendations for the calculation of shear viscosity using reverse nonequilibrium molecular dynamics. *The Journal of Chemical Physics*, **132**(1), 2010.

[152] F. Müller-Plathe. Reversing the perturbation in nonequilibrium molecular dynamics: An easy way to calculate the shear viscosity of fluids. *Physical Review E*, **59**:4894–4898, May 1999.

[153] F. Vögtle, G. Richardt, and N. Werner. *Dendrimer Chemistry: Concepts, Syntheses, Properties, Applications*. Wiley-VCH, 2009.

[154] Thomas G. Mezger. *The Rheology Handbook: For Users of Rotational and Oscillatory Rheometers*. Vincentz Network GmbH & Co KG, 2006.

[155] D. Rubenstein, W. Yin, and M.D. Frame. *Biofluid MEchanics*. Elsevier, 2001.

[156] T. H. Mourey, S. R. Turner, M. Rubinstein, J. M. J. Fréchet, C. J. Hawker, and K. L. Wooley. Unique behavior of dendritic macromolecules: intrinsic viscosity of polyether dendrimers. *Macromolecules*, **25**(9):2401–2406, 1992.

[157] Ch. Dufès, I. F. Uchegbu, and A. G. Schätzlein. Dendrimers in gene delivery. *Advanced Drug Delivery Reviews*, **57**(15):2177 – 2202, 2005.

[158] C. Klix, F. Ebert, F. Weysser, M. Fuchs, G. Maret, and P. Keim. Glass elasticity from particle trajectories. *Physical Review Letters*, **109**:178301, 2012.

[159] J. Farago, A. N. Semenov, H. Meyer, J. P. Wittmer, A. Johner, and J. Baschnagel. Mode-coupling approach to polymer diffusion in an unentangled melt: I. the effect of density fluctuations. *Phys. Rev. E*, **85**:051806, 2012.